TRANSITION TO HIGH DIMENSIONAL DYNAMICS IN SYSTEMS OF COUPLED OSCILLATORS

A thesis submitted to the University of Manchester
for the degree of Doctor of Philosophy
in the Faculty of Engineering and Physical Sciences

2007

By

Nicholas J. M^{C}Cullen

School of Physics and Astronomy

Contents

List of Tables

List of Figures

Abstract

This thesis presents the results of investigations into high dimensional dynamics in systems of coupled oscillators. Modified van der Pol electronic oscillators are used for these investigations, proving ideal due to the large amounts of high quality data that can be obtained from them. Various coupling configurations are used, to study complex dynamics in simple nonlinear networks.

A newly developed method for determining the local attractor dimension is introduced which is very easy to implement, as well as being robust enough to yield useful information solely from experimental time-series data. Results are presented using this method for detecting unstable dimension variability (UDV), which is detrimental to numerical models of systems suffering from it, reducing the reliability of such models. The method is also used to identify invariant sets and extract them from the overall attractor. This allows the evaluation of shadowing times, which are a measure of the length of time for which numerical results can be relied. The distributions of these shadowing times are shown to have different scaling for short and long times, in agreement with theoretical predictions. The separated invariant sets are additionally used to make measurements of the local Lyapunov exponents, which is not usually possible from experimental data.

The results of an investigation into the development of high dimensional dynamics in the system are described. Hyperchaos is found to appear in the system after the combination of two distinct phase-multistable sets. Numerical studies reveal that each of these sets independently develops a second positive Lyapunov exponent as they lose stability to become nonattracting sets. The transition to two positive Lyapunov exponents and hyperchaos is found both experimentally and numerically to be smooth in both of the phase-multistable synchronisation states. To uncover the origin of this transition experimentally, generalised synchronisation is investigated over a range of parameter values. Additionally, the transition is studied in terms of the topological dimension, using the method developed for detecting UDV.

The progressive loss of generalised synchronisation, along with the smooth transition in the Lyapunov exponents and steady change in the measured local dimension all indicate that attractor bubbling due to a riddling bifurcation is the mechanism responsible for the transition to high dimensional dynamics in the system.

Declaration

No portion of the work referred to in this thesis has been submitted in support of an application for another degree or qualification of this or any other university or other institution of learning.

Copyright

To Anna:

It's all your fault!

☺

Acknowledgements

$\mathcal{A}$n un-payable debt of gratitude is owed to my supervisor Dr. Pablo Moresco for his endless guidance and support throughout the duration of my time here. Without his patient supervision and moderating influence I'm sure my more chaotic tendencies would have had me turning up more blind alleys, dead ends and other such traffic related clichés, before arriving late as usual at the deadline. I'm surprised he hasn't torn his hair out or gone bonkers by now, having to deal with my idiocy for three and a half years.

$\mathcal{N}$ext, to all other members, past and present, of the Manchester Centre for Nonlinear Dynamics, as well as the wider Department (or should that be *School*) of Physics and Astronomy and further afield with whom I have had many stimulating discussions, both academic and otherwise, I give my heartfelt thanks for creating an atmosphere of fascinating contemplation and welcome distractions. Special mentions go to Professor Martin Golubitsky and Professor Tom Mullin for providing me with the opportunity to work on the feed-forward network described in Chapter 4.

$\mathcal{N}$ow, as always, my parents and the rest of my family continue to give me nothing but total support for my *unusual* "career" choice, and I owe my very existence here to their understanding, encouragement and support, both morally and financially.

$\mathcal{A}$nd finally on paper but first in my heart, all of my friends. You know who you are. Thank you for preventing me from straying too far from or getting too close to sanity. Especially the latter.

Author's Publications

The following is a list of any work included in this thesis which has to date been, or is due to be published in peer-reviewed academic journals by the author.

1. The method described in Chapter 3, along with a selection of the results of its application presented in Chapter 5 appear in:

   N. J. M^{C}Cullen and P. Moresco.

   "Method for measuring unstable dimension variability from time series."

   Phys. Rev. E., 73:46203, 2006.

2. The results of the investigation presented in Section 4.5 have been accepted for publication in:

   N. J. M^{C}Cullen, T. Mullin and M. Golubitsky

   "Sensitive signal detection using a feed-forward network."

   Phys. Rev. Lett., in press.

The most incomprehensible thing about the universe is that it is at all comprehensible.

Albert Einstein

Chapter 1

An Introduction to Dynamical Systems and Chaos

1.1 Nonlinear Dynamics in Nature

1.1.1 Introduction

At first glance nature appears to be inherently complex and largely unpredictable but, on closer inspection, structure - albeit complicated - is found everywhere. To gain an understanding of the world, scientists try to find order and rules; often by making simplifying assumptions.

Until recently, this lead most to believe that even the most seemingly impenetrable of problems could be completely understood if only the basic equations were known. Systems were assumed to fall into two broad categories, deterministic and stochastic. Deterministic systems were previously assumed to be largely predictable, with the random processes accounted for using statistical averages. Thus it was believed that long term prediction of even complicated dynamics was possible.

However, deterministic systems only remain predictable when using linear approximations, or only weakly nonlinear models. Though it has long been known

that some nonlinear differential equations could have no unique solution and produce unpredictable results (for example Poincaré's work on the *three body problem* [PG92]), it was until recently thought that in most practical situations these effects could be neglected. Since the advent of modern computing, and Edward Lorenz' celebrated computer simulations [Lor63], it has become possible to numerically solve nonlinear models that are analytically insoluble. When taking into account the full nonlinearities, many systems, even simple natural ones, can exhibit aperiodic behaviour where almost identical states quickly diverge. In such cases the dynamics depends sensitively on the initial conditions and long term prediction becomes impossible; a phenomenon known as deterministic chaos. This type of behaviour is found in such important aspects of nature as the evolution of the global climate and local weather patterns and it has long been suspected that fluid turbulence is a form of high dimensional chaos [Mul93]. In recent times it has become clear that much of nature's complexity can be explained by using nonlinear models [Gol06].

Conversely, another outcome of these same nonlinear models is the appearance of temporal or spatial order and patterns, which often emerge spontaneously. Systems containing a large number of elements, where it would seem like the many interactions between the elements would create impossibly complex dynamics, can give rise to very simple states overall. An interesting overview of systems in which nonlinearities give rise to self-organisation and pattern formation can be found in the non-technical book by Philip Ball [Bal99]. From the patterns on animals skins to the beating of the human heart and the synchronisation of animals' circadian rhythms with the passing of day and night, nonlinear dynamical models have been put forward to explain a wealth of natural systems and these provide examples of some of the basic features of nonlinear dynamics.

1.1.2 Simple Chaos

Nonlinear dynamics can be applied to natural systems in a wide variety of contexts and chaos can be found throughout nature. One of the simplest examples of chaotic dynamics can be obtained from a biological motivation. Considering the situation of a species living in isolation, with a food supply that can support a limited population, the following model can be derived.

The population size in any given year is assumed to be entirely determined by that of the previous year. Thus it can be sampled annually, giving an iterative description of the dynamics (a *mapping*). The population in year $n+1$ is represented by x_{n+1} and is proportional to the population x_n in year n, multiplied by a constant parameter, α, related to the deficit between deaths and new offspring. If the maximum population size is taken to be 1, at which value the animals consume their entire food supply and die out, then x_{n+1} is also proportional to $1 - x_n$; giving the following expression:

$$x_{n+1} \quad = \quad \alpha x_n(1 - x_n). \tag{1.1}$$

This is known as the quadratic or logistic map and can be used to demonstrate many of the features found throughout nonlinear dynamics.

A calculation of the population dynamics is carried out by choosing a value for α and assigning an arbitrary initial value to x_n in the range $0 < x_n < 1$. The resulting value of the population in the following year x_{n+1} is then fed back into the equation as x_n and the process is repeated a sufficient number of times for transient behaviour to die-out and the population to reach its long term state. At values of $0 < \alpha < 1$ the iteration always tends to the solution $x^* = 0$, representing the population dying out due to there being on average fewer than one survivor per individual. For values of $\alpha > 1$ the solution $x^* = 0$ becomes unstable and a nonzero equilibrium value is now reached that is independent of the initial choice of x_n. In the above region of the parameter space – in

this example one dimensional (*co-dimension one*) and based on α – the steady-state solution is described as an *attracting fixed-point*, as iterations started in its vicinity will converge to it. More details about this and other types of *attractor* are given in Section 1.2.1. At $\alpha = 3$ a qualitative change in the dynamics (a *bifurcation*) occurs, this time with x^* not settling to a single value but instead alternating between two. This is an example of a *period doubling* bifurcation, with the population size now oscillating between two values in alternate years. Several types of bifurcation are described in Section 1.2.2. As the parameter is increased further, period doubling bifurcations occur at progressively shorter intervals, decreasing geometrically in the parameter α. At a critical value of $\alpha \approx 3.57$ the difference in α between successive period doubling bifurcations goes to zero and the sequence becomes *chaotic*, with the sequence of population sizes never repeating exactly. This infinite number of period doubling bifurcations leading to chaotic oscillation is the Feigenbaum route to chaos. The set of values of x^* is now a *chaotic attractor*, as sequences started from initial conditions outside it will, after some transient, end up inside and remain there for all future iterations. Sensitivity to initial conditions can be demonstrated by picking two similar values of x_1 at the same value of the parameter α and observing how their sequences diverge under repeated iteration. This is shown in Figure 1.1 for the initial conditions $x_1 = 0.1, 0.101$, at $\alpha = 3.72$.

The results of iterating the quadratic map at different values of the parameter α are shown in Figure 1.2 (a). For each value of α the long-term behaviour, x^*, of the calculation is plotted. The structure in the chaotic regime is complicated and regions within the structure are scaled up in (b) and (c) to show some of the complexity contained within Equation (1.1). It can be seen in Figure 1.2 (b) that periodic windows exist within the chaotic region. The periodic windows are said to be *dense* in this region, meaning there are an infinite number of periodic windows interspersed with an infinite number of chaotic bands.

These periodic windows appear suddenly in a *crisis* as the parameter is varied

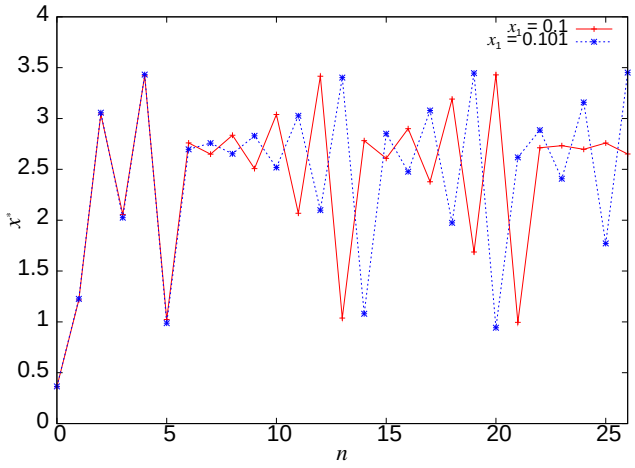

Figure 1.1: Sensitivity to initial conditions in the quadratic map. Solutions were iterated from initial conditions $x_1 = [0.1, 0.101]$ at a parameter value of $\alpha = 3.72$. The states initially follow each other closely before quickly diverging.

slowly past a particular value. The crisis seen here, leading to periodic windows in a chaotic region, is known as a *subduction crisis* but there are other types of crisis with different characteristics [GOY83]. The periodic states thus formed suffer more period doubling bifurcations and the central bifurcation diagram within the main periodic window is shown in Figure 1.2 (c). The structure of the chaotic attractor (the set of points at a particular α) is of fractal dimension, being between 0 and 1. A type of fractal structure can also be seen in the diagram as a whole, with similarity observed between the appearance of this sub-region and the structure of the whole *bifurcation diagram* in Figure 1.2 (a).

This and other types of structure or pattern produced by nonlinear models can be seen throughout the natural world. Therefore, it is clear that using the natural pattern forming tendencies of nonlinear systems could prove advantageous for explaining many features found in nature.

1.1.3 Dynamics versus DNA

One of the current questions in biology is how all the richness of animal appearance and behaviour can be derived from the information encoded in the genes.

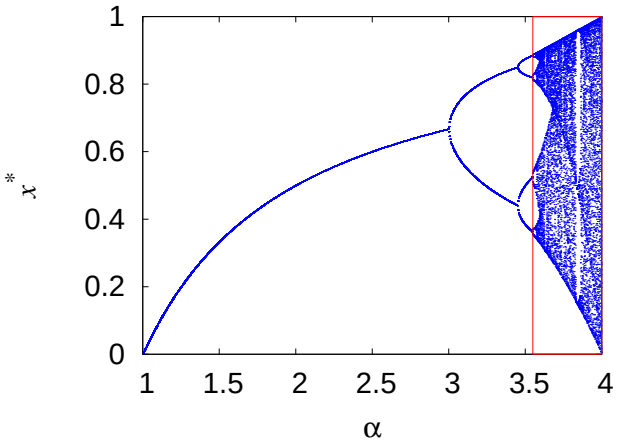

(a)

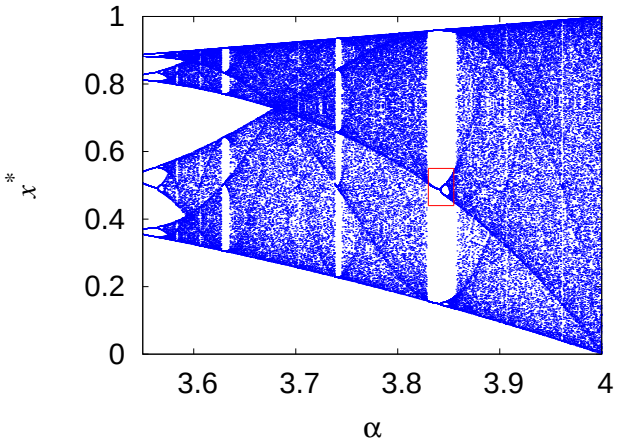

(b)

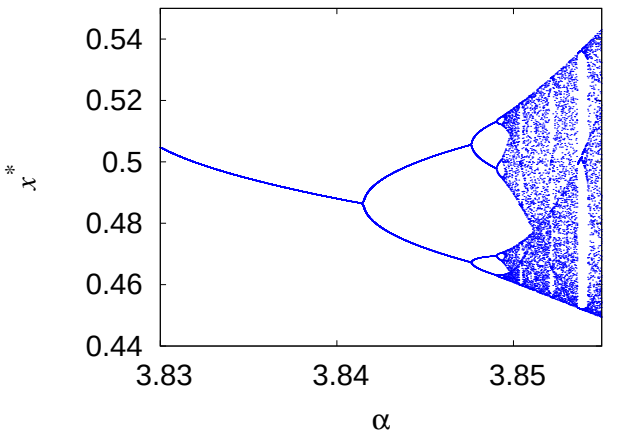

(c)

Figure 1.2: Bifurcation diagram of the quadratic map. Values of x^* are obtained by iterating the quadratic Equation (1.1) at various values of α. At lower α iterations lead to a single solution. As α is increased, oscillations develop and become more complicated at successive period doubling bifurcations, until chaos emerges. Magnified views of regions within (a) are shown in (b) and (c), showing self-similarity to infinitely small scales.

It is well known that the number of genes alone cannot account for the level of complexity found in life-forms and it is accepted that the interaction between genes also needs to be taken into account.

A popular idea in the nonlinear dynamics community is that not all of the observed patterns are mapped out explicitly by the instructions in our DNA. Instead it has been suggested that nature takes advantage of the complexity that can be derived from simple nonlinear systems. Very simple systems can be made to produce astoundingly complex spatial or temporal patterns. Alan Turing demonstrated that a model based on a process of two competing chemical species could spontaneously produce patterns reminiscent of those seen on animal skins [Tur52]. Also, patterns seen in heart muscle during regular function and fibrillation can be reproduced using the model of an excitable oscillating medium [Fit61]. Similarly, small networks of coupled nonlinear oscillators can output complex rhythms resembling those necessary for the functioning of animals, such as the role of groups of neurons known as *central pattern generators* (CPGs) in such things as patterns of locomotion in legged animals [GSBJ98]. That nature would exploit these principles is a seductive idea, as it would prove exceptionally economical in terms of the amount of genetic material required to fully encapsulate an organism's workings.

The last two examples, as well as many others, are related by the fact that they can be modelled as systems of coupled oscillators. It is possible to represent spatially extended systems as networks of discreet elements and such *finite element* models are useful for many scientific and engineering applications. When the individual elements are capable of complicated dynamics such as chaos, the overall behaviour can be highly complex. Examples of this are fluid turbulence and spatiotemporal chaos, both of which can be described by partial differential equations and have an infinite number of degrees of freedom. If scientists hope to have a chance of accurately modelling such problems, a firm understanding of the dynamics in intermediate cases is needed. The interaction of small numbers of

chaotic oscillations can produce high dimensional chaotic states. However, there also exist regimes where the dynamics are reduced through synchronisation of neighbouring elements and the behaviour can be understood using concepts from low-dimensional chaos. This thesis deals with the transition to high-dimensional dynamics in systems of coupled oscillators.

1.2 Concepts in Dynamical Systems Theory

The example of the quadratic map in Section 1.1.2 demonstrates how even simple nonlinear equations can produce chaotic dynamics, with sensitivity to initial conditions leading to divergence of originally indistinguishable solutions. This, along with noise and uncertainty in measurements of the variables associated with the system's degrees of freedom, renders long-term prediction impossible. Despite this lack of quantitative predictability much useful information can be obtained from measurements and simulations of a given system. This has relied on researchers devising new ways of representing and extracting dynamical information from nonlinear systems.

Dynamical systems theory has thus provided the framework for the understanding of systems demonstrating chaos and other nonlinear phenomena. This has often meant concentrating on qualitative similarities between systems and statistical averages, instead of detailed quantitative prediction. The following sections outline some of the concepts in dynamical systems theory and the types of information that can be gained from studying nonlinear systems.

1.2.1 Attractors

In unforced dissipative systems dynamical states will end up on stable solutions from a variety of initial conditions. In this case the stable solutions are called the *attractors* of the system. For the damped pendulum the downward hanging state is an attractor, as the system will asymptote to this state from all starting

points. The upward balance point is an unstable fixed-point in phase space and states started nearby will quickly diverge.

The stability of fixed points and periodic solutions to small perturbations can be determined by the application of linear stability analysis. Taking an η degree of freedom system of ordinary differential equations (ODEs), $\dot{x} = f(x)$, the local stability about some equilibrium solution x^* can be determined by obtaining the linearised equations of the system $\dot{y} = Df(x^*)y$, where D is the matrix of partial derivatives of the system (the Jacobian):

$$D = \begin{pmatrix} \frac{\partial \dot{x}_1}{\partial x_1}\big|_{(x^*)} & \frac{\partial \dot{x}_1}{\partial x_2}\big|_{(x^*)} & \cdots & \frac{\partial \dot{x}_1}{\partial x_\eta}\big|_{(x^*)} \\ \frac{\partial \dot{x}_2}{\partial x_1}\big|_{(x^*)} & \frac{\partial \dot{x}_2}{\partial x_2}\big|_{(x^*)} & \cdots & \vdots \\ \vdots & \vdots & \ddots & \vdots \\ \frac{\partial \dot{x}_\eta}{\partial x_1}\big|_{(x^*)} & \cdots & \cdots & \frac{\partial \dot{x}_\eta}{\partial x_\eta}\big|_{(x^*)} \end{pmatrix}. \tag{1.2}$$

The eigenvalues (λ) of this matrix give the stability along different directions, with negative/positive values indicating linear stability/instability along the respective eigenvectors. Directions along which states converge are described as contracting directions (or stable dimensions) in phase space and those along which they diverge as expanding directions (or unstable dimensions). If solutions $y(t) = y_0 e^{\lambda f(x^*)t}$ of $\dot{y} = Df(x^*)y$ have exponents which are negative overall, $e^{\lambda f(x^*)t}$ decreases with time and the solution is *linearly stable*. The region containing a set of initial conditions y_0 which are attracted to a stable solution x^* is known as the *basin of attraction* of the solution. The solution x^* is an attractor if it is stable and there exists a basin of attraction belonging to it. The distances (δ) from the set of nearby initial conditions y_0 to an attractor x^* will therefore contract and all $y(t)$ asymptote to x^*.

1.2.2 Common Bifurcations

A feature of nonlinear systems is that sudden changes in the qualitative solution structure can occur on variation of one or more of the system parameters. Examples of this type of change, or *bifurcation*, were demonstrated for the quadratic equation (1.1), with the dynamics becoming progressively more complicated as the parameter was increased. The bifurcation structure of a system can be illustrated in a *bifurcation diagram*, exemplified in Figure 1.2. Here, the solution structure was shown as a function of a single parameter in a *one-parameter bifurcation diagram*. For variation of two or more parameters the locus of bifurcations can be shown in the parameter space.

Bifurcations occurring around a fixed point are referred to as *local bifurcations* and can be detected by studying the eigenvalues of the linearised vector field around the solution, with a real eigenvalue going to zero at a bifurcation. This also applies to bifurcations of periodic orbits, as they are fixed points of maps. Local bifurcations are often characterised by the appearance of new solutions in phase space which can be either stable or unstable. The qualitative change in dynamics between regular and chaotic motion usually comes about via a sequence of bifurcations and it is important to understand the route to chaos in terms of the bifurcations undergone. The nature of a bifurcation depends on the form of the dominant nonlinear terms in the equations, with qualitatively different transitions occurring in each case. Some common bifurcations encountered in the current study are outlined below but a detailed introduction to bifurcation theory can be found in Wiggins [Wig90].

The Saddle Node Bifurcation

A simple example of a bifurcation is the saddle-node bifurcation, with two solutions appearing where there were previously none (Fig. 1.3).

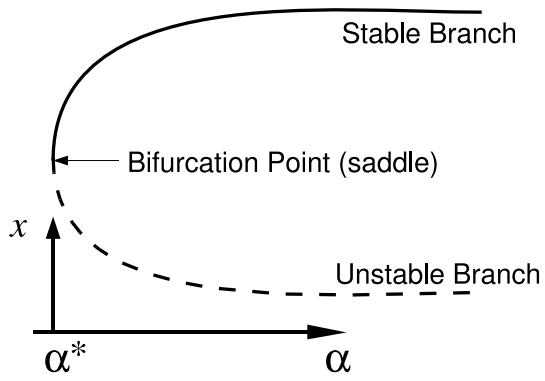

Figure 1.3: The Saddle-node bifurcation. On variation of a parameter, α, two solutions for the system variable x appear: one stable and the other unstable.

This can be derived by looking at equilibrium solutions ($\dot{x} = 0$) of the equation

$$\frac{\mathrm{d}x}{\mathrm{d}t} = \alpha - x^2 \tag{1.3}$$

at different values of the parameter α. There are no solutions at $\alpha < 0$ but for $\alpha > 0$ there are two solutions, $x = \pm\sqrt{\alpha}$.

In this case one of the new solutions is stable to perturbations and the other is unstable. Bifurcations often appear in pairs in this way and they are generally characterised by either a change in stability of preexisting solutions or the appearance of one stable and one unstable solution. This is given a more rigorous treatment in the next example.

Pitchfork Bifurcations

One of the most important bifurcations is the (supercritical) pitchfork bifurcation, which can be obtained from steady-state solutions of the cubic ODE:

$$\frac{\mathrm{d}x}{\mathrm{d}t} = \alpha x - x^3, \tag{1.4}$$

with α as the variable parameter. The solution $x^* = 0$ exists for all α and is the only solution for $\alpha < 0$. The solution structure bifurcates at $\alpha = 0$, above which

there are two more real solutions, $x^* = \pm\sqrt{\alpha}$, as shown in Figure 1.4.

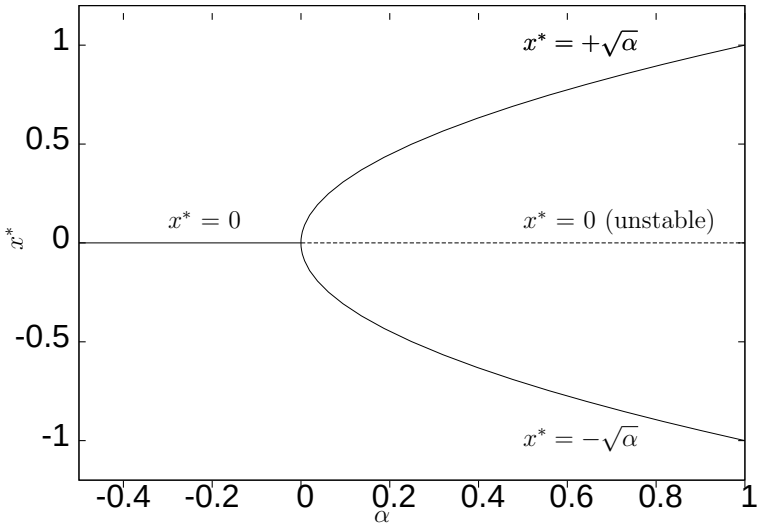

Figure 1.4: The pitchfork bifurcation. As the parameter α is increased past $\alpha = 0$ the single solution loses stability to two new solutions.

The linear stability of the various solutions can then be determined by calculating the local linear gradient at the solution. This is outlined in more detail in Section 1.2.1. From Equation (1.4) for this single degree of freedom (DOF) system the local gradient is simply $\frac{\partial \dot{x}}{\partial x}|_{(x^*)} = \alpha - 3(x^*)^2$, showing that the trivial ($x^* = 0$) solution is linearly unstable for $\alpha > 0$, represented by a broken line in Figure 1.4. Bifurcations are characterised by an eigenvalue of the system crossing the imaginary axis, with the corresponding change in stability of the solution. It can also be seen in this example that both nontrivial branches created at the bifurcation point are stable. Therefore, in this case there is a bifurcation in which a stable solution suffers an exchange of stability to become unstable at the bifurcation point, along with the appearance of two new stable solutions.

Although pitchfork bifurcations can be found in many systems, they are usually not as simple as in the above ideal situation. A system requires perfect symmetry for this type of ideal pitchfork bifurcation to exist. Inevitably, real systems contain some imperfection which has the effect of creating a bias, breaking the ($\mathbb{Z}_2$) symmetry required for this type of bifurcation. The simplest way to

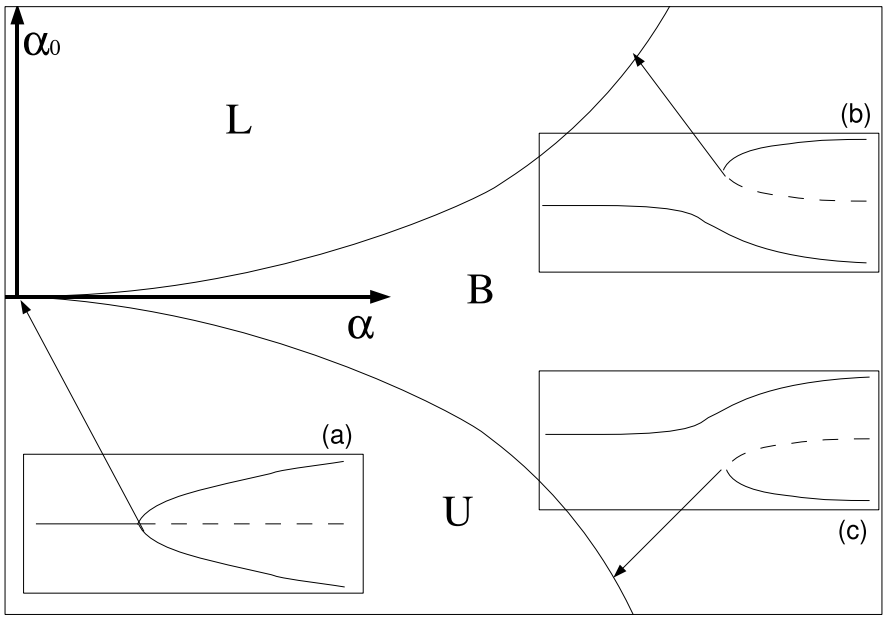

Figure 1.5: Imperfect pitchfork bifurcations. Varying the imperfection term α_0 disconnects the pitchfork, creating a continuous branch and a saddle-node. In region L only the lower branch exists. Similarly for U and the upper branch. In B both branches coexist, but solutions stay on the continuous branch on increasing the bifurcation parameter, α.

model this is with the addition of a linear offset term, α_0, to the equations:

$$\frac{\mathrm{d}x}{\mathrm{d}t} = \alpha x - x^3 + \alpha_0. \tag{1.5}$$

This has the effect of disconnecting the different branches of the pitchfork bifurcation, creating a continuous (preferred) branch and a disconnected saddle-node, as is shown in Figure 1.5. The curves show the loci of the saddle-node for different values of α_0 and α.

This effect is shown in Section 4.7.2 to be crucial for understanding the dynamical regimes found in coupled systems, where the effect of coupling is to induce a small perturbation in each subsystem proportional to the output of the other.

The Hopf Bifurcation

A transition from steady-state to time-dependent behaviour is seen when a complex conjugate pair of eigenvalues crosses the imaginary axis in a Hopf bifurcation. The Hopf bifurcation can be obtained from solutions of the equation:

$$\frac{\mathrm{d}x}{\mathrm{d}t} = x(\alpha + \beta|x|^2), \tag{1.6}$$

where x is complex, $\beta = a + ib$ and α is the parameter. When α is negative the system is in equilibrium but for $\alpha > 0$ the solutions are periodic. On the creation of a periodic limit cycle an unstable fixed-point remains where there was previously a stable attracting equilibrium, around which the oscillations "rotate".

Period Doubling Bifurcations

Periodic oscillations are fixed points of maps so the bifurcations of these are also considered local bifurcations.

A bifurcation is found when considering steady solutions $x_{n+1} = x_n$ of the quadratic map $x_{n+1} = \alpha x_n(1 - x_n)$ (Eqn. (1.1), introduced in Sec. 1.1), as the parameter is increased past $\alpha = 3$. For $1 < \alpha < 3$ the solution $x^* = 1 - \frac{1}{\alpha}$ is found to be stable; losing stability at $\alpha = 3$. Just beyond this value stable fixed points can be found on the second iterate; i.e. by considering steady-state solutions of the double-return map $x_{n+2} = \alpha^2 x_n(1-x_n)(1-\alpha x_n(1-x_n))$. This is an example of a *period doubling* bifurcation.

The quadratic map approaches chaos via a cascade of period doubling bifurcations. In this case the number of iterations required for solutions to return to a previous value is successively doubled at each bifurcation. The analogy of period doubling in continuous-time systems is where oscillations have amplitudes that alternate between two values on successive maxima. This behaviour is shown in Figure 1.6, where (a) is the oscillation after the first period doubling bifurcation and (b) after a second.

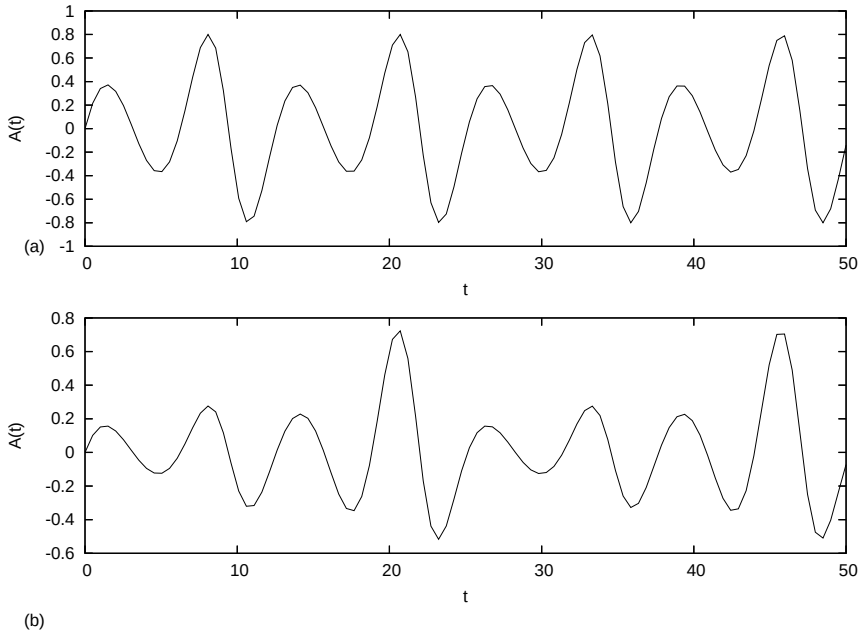

Figure 1.6: Period doubling for continuous-time systems. A period-2 oscillation is shown in (a) and a period-4 in (b).

Period doubling can lead to chaotic motion via a succession of bifurcations, each lengthening the return period by a factor of two, similar to period doubling on maps. On period doubling, an unstable solution remains, with nearby states diverging exponentially from it. In continuous-time systems, these remnants are known as unstable periodic orbits (UPOs). Chaotic attractors that have developed through the Feigenbaum scheme have suffered an infinite number of period doubling bifurcations and therefore contain an infinite number of UPOs. This feature is important for understanding the stability of chaotic attractors, as described in Section 1.2.6.

Global Bifurcations

In the above examples a bifurcation can be detected by studying the stability of a fixed point or periodic orbit at any locality on the solution. In other cases a sudden change in the qualitative dynamics occurs which can not be detected by studying the local eigenvalues of the solution. In these cases the transition comes

about due to an interaction of the attractor with another solution. If one part of a periodic orbit or chaotic attractor collides with another set, the dynamics is affected over the whole solution. This type of transition is known as a *global bifurcation*. An example of a global bifurcation is when a limit-cycle collides with an unstable saddle point (with both positive and negative eigenvalues to the Jacobian) in a *homoclinic bifurcation*. This type of bifurcation is discussed in context in Section 4.7.1.

In the case of chaotic attractors, a collision with another set is known as a *crisis* and can lead to a sudden change in the global characteristics of the dynamics of the system. For example if, on variation of a parameter, trajectories in a chaotic attractor stray into the basin of attraction of a fixed point or periodic orbit the chaotic attractor becomes an unstable (chaotic) saddle and all trajectories on it will be transient.

1.2.3 Phase Space Representation

The data obtained from measurements of a system's variables are usually in the form of a time-series of discrete isochronous values. However, for complicated dynamics and especially for chaotic cases, it is often more useful to use a representation of the data based on the degrees-of-freedom of the system. This *phase-space* (or *state-space*) can be constructed using any set of measures of the system as axes, so long as this set is unique for each state of the system. A simple example of this is the undamped un-driven simple pendulum performing sinusoidal oscillations. Each point in its motion can be uniquely associated with a vector based on its position and angular velocity, from which the phase space of the system can be constructed.

1.2.4 Phase Space Trajectories

A stationary fixed-point state of a system is represented by a static point, whereas dynamical states are curves in phase space, as shown in Figure 1.7. Arrows are

used to show the evolution of states (*direction of flow*), since time is not explicitly represented by an axis in phase space. Where a fixed-point is an attractor initial conditions started within the basin of attraction of the solution will follow a curve towards it in phase-space, as sketched in Figure 1.7 (a). In the case of stable periodic solutions, these *phase-space trajectories* form closed loops, referred to as *limit-cycles*. The pure sinusoidal oscillations produced by the simple pendulum form ellipses in the amplitude – angular velocity phase space.

Harmonic oscillations such as these require only two-dimensions in phase-space but nonlinearities in the equations can give rise to more non-planar geometries. Complicated dynamics can exist, such as oscillations which have a different amplitude on alternative maxima, causing trajectories to perform multiple loops in phase space. In a two-dimensional space trajectories would therefore cross, giving the system a choice for a particular initial condition, which violates the deterministic nature of these systems. Thus for complicated oscillations, such as chaos, there must be at least three degrees of freedom to a continuous-time system, to prevent the system having such non-deterministic points. [1]

Trajectories on chaotic attractors appear to cover a surface in phase-space, with a structure which has fractal dimension. Despite the complicated nature of individual trajectories, the surface on which they exist is a fixed geometrical object in phase-space and does not vary in time, known as an *invariant manifold*. The expansion from having an unstable dimension, which gives rise to sensitivity to initial conditions, is able to exist in a globally stable attractor because of folding of the manifold due to nonlinearities in the equations. Diverging trajectories are thus folded back into the attracting region along the contracting direction, re-entering it at re-injection points, as shown in the sketch of Figure 1.7 (c) and (d). The invariant manifold is flat locally (on small scales) and the directions along which nearby trajectories contract or expand (the stable and unstable dimensions)

[1] In the discreet-time case of non-invertible maps, where the mapping $x \mapsto f(x)$ has no inverse, such as the logistic map (1.1) in Section 1.1.2, chaos can exist with one degree-of-freedom.

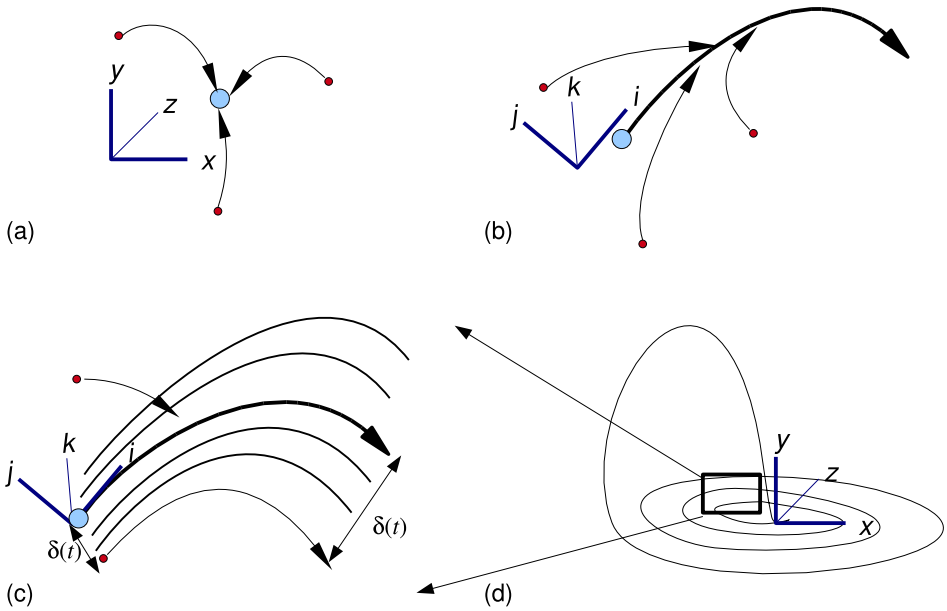

Figure 1.7: Local stability around solutions in phase space. The stable fixed point shown in (a) is an attractor, with solutions from all initial conditions following trajectories towards it in phase-space (shown by arrows). A portion of a stable dynamical solution is shown in (b) by the bold curve. Here the coordinate basis has been reoriented so that i is aligned with the direction of flow, which is neither attracting nor contracting (the neutral direction). Directions j and k are stable dimensions to the flow, along which nearby trajectories contract. In (c) the attractor is chaotic and has both stable and unstable directions locally, with j aligned along the contracting and k the expanding direction. The expansion is represented by an increase in time of the length of the distance $\delta(t)$ between the solution and a nearby trajectory. The chaotic attractor is stable overall, with diverging trajectories being folded and re-injected along the stable direction, as shown in (d).

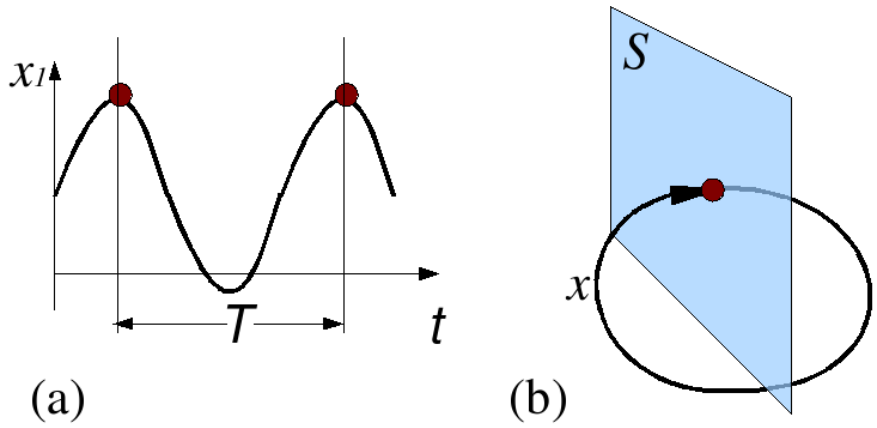

Figure 1.8: Converting a flow to a map. Using (a): periodic sampling of period $t = T$ and (b): the cutting of a section S in phase-space.

can be defined and the rates of expansion or contraction quantified, as explained in more detail in Section 1.2.6.

1.2.5 Maps and Sections

The representation of the dynamics of a system can be simplified without losing any dynamical information by converting the flow to a map, reducing the dimension of the phase-space by one. If a suitable time-scale can be chosen, this can be done by periodically sampling the variable at the ideal intervals (Fig. 1.8(a)). The map of one point to the next can then be obtained and methods from discrete-time systems can be applied. Simple limit cycles appear as fixed points on the map, with period doubled states appearing as two points and so on up to higher periodic orbits. Chaos appears as a set of points with fractional dimension (a fractal).

Another way of converting a flow to a map is to construct a *Poincaré surface of section* of the flow (Fig. 1.8(b)). This is done by plotting only the points at which the flow crosses some suitably defined section in a particular direction.

An example of obtaining a Poincaré section from a flow is shown in Figure 1.9. The chaotic attractor used was obtained by numerical integration of the equations of motion for the system described in Chapter 4. It is shown in all

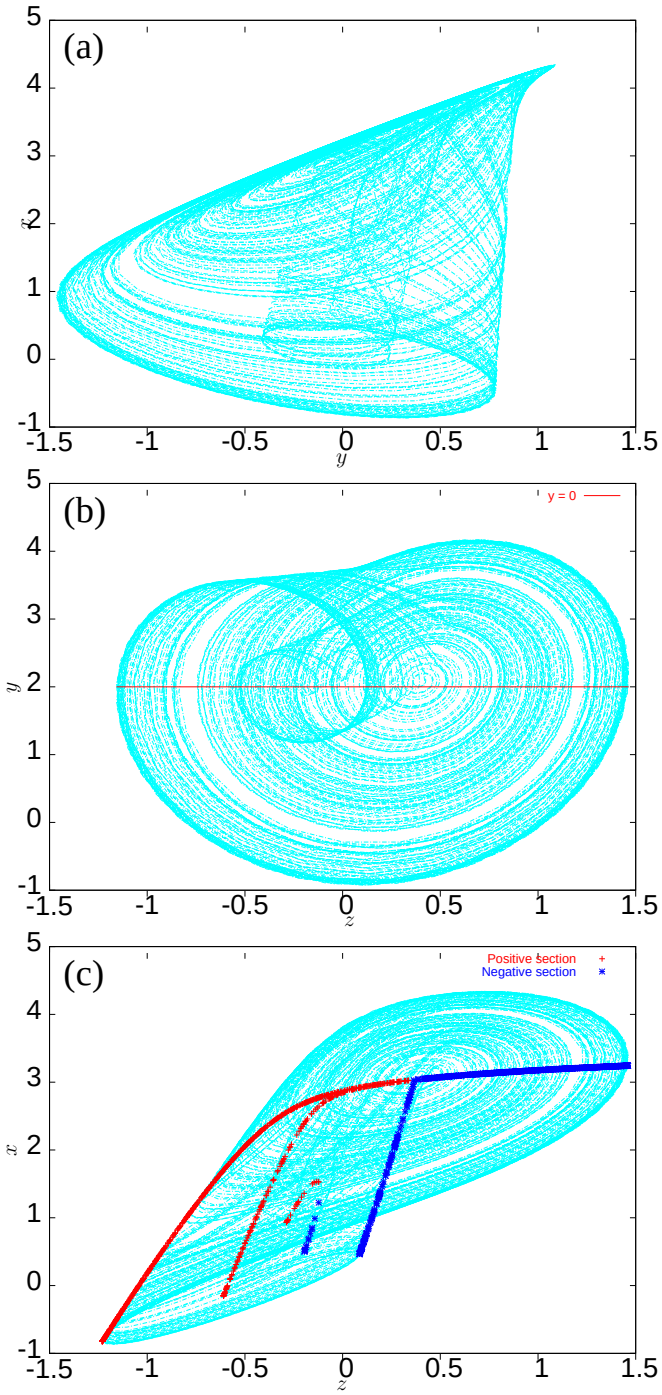

Figure 1.9: Reduction of a chaotic flow to a Poincaré surface of section on the $y = 0$ plane. The flow is shown in turquoise in three projections: (a), (b) and (c); with points defined by the Poincaré section (red line) shown by red or blue points depending on the choice of the flow cutting in the positive or negative direction respectively.

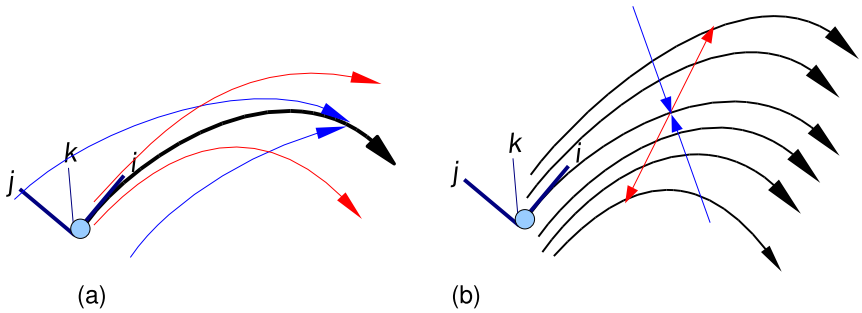

Figure 1.10: Unstable periodic orbits (UPOs) in a chaotic attractor. The directions of contraction and expansion of a single UPO are shown in (a) by blue and red arrows, respectively. An ensemble of UPOs combine to form the manifold of a chaotic attractor, arranged in such a way to give it both locally expanding and contracting directions (b).

three projections of the three dimensional phase space, with the $y = 0$ plane being cut to make the Poincaré section.

1.2.6 Local and Global Stability of an Attractor

In dissipative systems, stable fixed points and periodic solutions have a locally contracting flow from all directions[2]. This means that nearby initial conditions will be drawn onto the stable solution from all directions. However, the situation is qualitatively different for chaos, where the local flow is on average a saddle, having both stable and unstable directions. The locally unstable dimension comes from the infinite number of unstable periodic orbits (UPOs) contained within the attractor, as represented in Figure 1.10. Chaotic attractors have this property of local instability yet have global stability due to the ensemble of the UPOs being organised in such a way that forms a stable set having non-zero volume in phase space.

Nearby trajectories contract and expand along the stable and unstable directions respectively. This was shown in Figure 1.7 by the contraction or divergence of a set of initial conditions along different orientations. In the $[i, j, k]$ basis,

[2]With the exception of points separated along the local direction of flow i, which neither expand nor contract on average.

which is locally reoriented to be aligned with the principal orthogonal vectors of the flow, i is the direction of the flow, j is locally contracting (stable) and k is locally expanding (unstable). A short segment of such a flow is illustrated in Figure 1.11. The flow can be decomposed with respect to its expanding and contracting directions into a set of stable and unstable manifolds, shown here as blue and red surfaces, respectively.

1.2.7 Lyapunov Exponents

Through a complicated process of folding and re-injection, a chaotic attractor remains globally stable, with initial conditions contracting onto and becoming bounded by the size of the attractor. However, nearby trajectories are separated along the unstable directions and have local exponential divergence when averaged over long times. This was represented in Figure 1.7 (c) by the growth of $\delta(t)$, the linear separation of two trajectories along the locally expanding direction, k. Quantification of this exponential divergence of trajectories gives a measure of the stability of solutions to small perturbations. The flow can be decomposed into its component directions locally in phase space and the linear rates of expansion along the different directions determined. The time-averages of these rates can then be used to calculate the average exponents of the exponential expansion, known as the *Lyapunov characteristic exponents* of the system.

When considering some small displacement vector at a point $x(t = t_0)$ on a

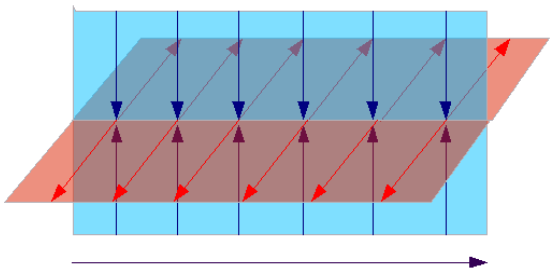

Figure 1.11: Local expanding and contracting directions to the flow on a chaotic attractor. The flow has both locally expanding (unstable) and contracting (stable) directions, shown in red and blue, respectively.

trajectory, $\underline{V}_n(0)$, aligned with an eigenvector of the linearised flow, its evolution $\underline{V}_n(t)$ is exponential with time:

$$\|\underline{V}_n(t)\| = \|\underline{V}_n(0)\|.e^{\lambda_n t}. \tag{1.7}$$

The Lyapunov exponents are defined as the average exponential rate of expansion or contraction along these orthogonal directions to the flow:

$$\lambda_n = \lim_{t\to\infty} \frac{1}{t} \ln\left(\frac{\underline{V}_n(t)}{\underline{V}_n(0)}\right). \tag{1.8}$$

As was mentioned previously, for systems of coupled ODEs, the linear stability of a fixed point is determined by finding the eigenvalues of the Jacobian matrix of partial derivatives evaluated on the solution. If the real parts of all eigenvalues are negative then the linearised flow in the region of the fixed point is contracting and the solution is stable. Unstable solutions will have one or more eigenvalues with positive real part. Lyapunov exponents can be considered a generalisation of this to chaotic states and flows in general.

A three degrees-of-freedom (DOF) chaotic attractor of a system will have three Lyapunov exponents. One is the expanding direction that characterises the sensitivity to initial conditions. There is also typically one zero (or neutral) exponent corresponding to the direction of the flow, along which there is neither expansion nor contraction on average, one point in the trajectory being the time evolution of the other along this direction. To be globally stable the system must be attracting on average so the third exponent is negative, the sum overall having to be less than zero for dissipative systems.

Global and Local Dimension

The dimension of the phase-space is determined by the number of degrees of freedom of the system, being equal to the minimum number of measurements required to uniquely characterise any state of the system.

Stationary states are points in phase-space, whereas limit cycles form a locally one dimensional line curved in higher dimensions. Chaotic attractors are fractal in dimension and exist on some invariant manifold which has a local topological dimension lower than that of the total phase-space. In the case of three DOF chaos, neighbouring trajectories are pushed apart in the expanding direction but close together in the contracting direction. Points are also spread out in the direction of flow, making the spread of trajectories approximately two dimensional locally.

In dissipative systems with more than three degrees of freedom there can be more than one locally expanding direction; a phenomenon dubbed *hyperchaos* [R$\ddot{\text{o}}$79]. Where there are two expanding directions (*unstable dimensions*) the trajectories are spread into a third dimension locally. Thus the local topological dimension is equal to the number of non-negative Lyapunov exponents.

1.2.8 Hyperbolicity of Attractors

Another important concept when considering chaos and hyperchaos in systems of ODEs is that of attractor *hyperbolicity*.

The dynamics on an attractor is said to be hyperbolic if the following three conditions are satisfied [GH83, page 238]:

1. At each point in the set the tangent-space can be split into expanding and contracting subspaces, along which the distances between two nearby trajectories will respectively grow or shrink exponentially in time.

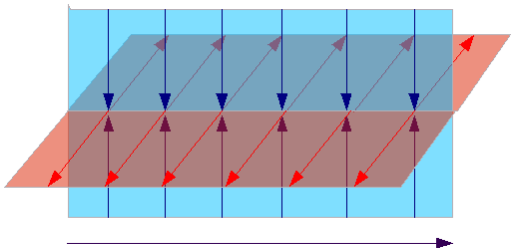

2. The angle between the stable and unstable subspaces is bounded away from

zero, i.e. there are no tangencies between expanding and contracting directions.

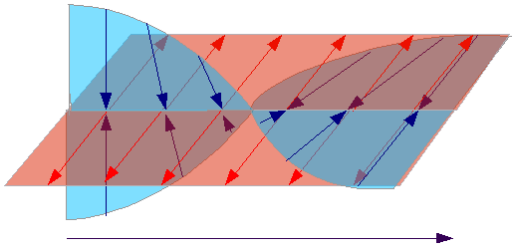

→ Non-hyperbolicity due to a tangency.

3. Along a typical trajectory the expanding subspaces evolve continuously into expanding subspaces only and contracting subspaces into contracting ones.

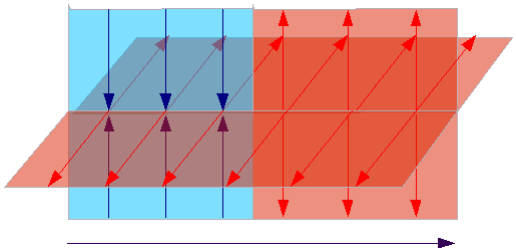

→ Non-hyperbolicity due to contracting direction losing stability.

The attractors of only a few dynamical systems can be proven to be hyperbolic for certain parameter values and it is believed that attractors in physically relevant systems usually lose hyperbolicity due to the existence of points violating conditions 2 or 3 [LGYK93]. Only recently has a physical system been found for which the attractors can be proved to be hyperbolic [Kuz05].

The second condition is violated if a tangency exists between the stable and unstable manifolds at some point on the attractor, where an expanding and contracting direction coincide. The third condition cannot be satisfied if there are variations in the dimension of the expanding and contracting subspaces in different parts of the set. This form of non-hyperbolicity is called unstable dimension variability (UDV) and can occur where the number of local directions of expansion varies at different points in the attractor, corresponding to differences in the local unstable dimension. Therefore, UDV arises when a typical trajectory in

the attractor visits regions containing UPOs with different numbers of expanding directions.

It is believed that the presence of tangencies is a common feature in low dimensional systems but in systems with more than three degrees of freedom, where attractors can be hyper-chaotic and contain periodic orbits with more than one expanding direction, UDV is believed to be commonplace [LLWG99].

1.2.9 Shadowing and Unstable Dimension Variability

Sensitivity to initial conditions naturally leads to the question of whether the *pseudo-trajectories* computed from models of physical systems, which suffer from round-off errors and inaccuracies in the model, actually correspond to some true solution of the system.

It would at first seem that, given these modelling inaccuracies and finite knowledge of the initial conditions, information gained from numerical models could be completely unreliable in chaotic regimes. However, recent research has shown that true trajectories can exist that stay close to, or *shadow*, pseudo-trajectories for long times; thus giving validity to statistical values obtained from computed trajectories [HYG87].

The length of time for which these conditions are valid, known as the *shadowing time*, has been shown to be strongly related to the hyperbolicity of the attractor. The shadowing time t_s is defined as the time for which a numerically calculated trajectory (or *pseudo-trajectory*) can be said to stay within some small distance δ to a trajectory of the real system (Fig. 1.12).

It has been shown that for hyperbolic systems the shadowing time is infinite [Ans67; Bow75], while for systems with tangencies the shadowing time will in general be finite and dependent on the error in each step of the computation of the trajectory [HYG88; GHYS90; SY91; CP91; CVV94]. Nevertheless, in many cases, using high accuracy calculations allows for the computation of trajectories

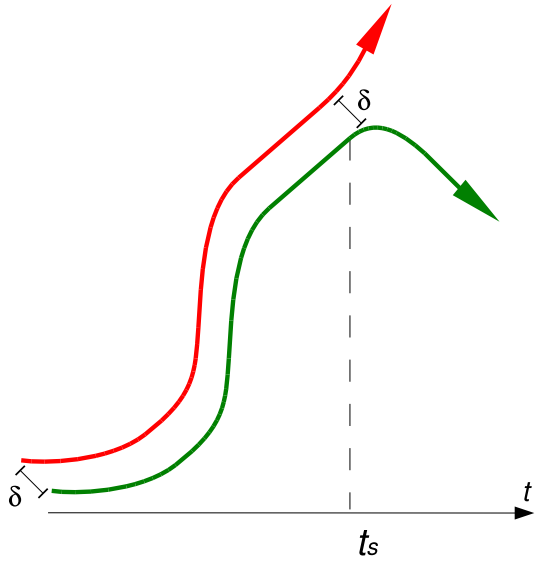

Figure 1.12: Shadowing time t_s is the time for which a numerical *pseudo-trajectory* stays within some small distance δ to a true system trajectory.

long enough to estimate reliable statistical averages. On the other hand, the obstruction to shadowing due to UDV has been found to be especially severe, leading not only to very short shadowing times, but also to a significant amplification of computational errors, suggesting that the modelling and computed averages are highly unreliable in such cases [DGSY94; SGY97; KKG+97; LG99; BS00; Sau02].

1.2.10 Short-Time Lyapunov Exponents

The Lyapunov exponents are usually defined for an infinite trajectory covering the whole attractor but they can also be defined for finite times, giving information on the local rather than global expansion and contraction rates. These are the short-time Lyapunov exponents (STLEs) and UDV can be discussed in terms of them. If one of the locally expanding directions at some point along a trajectory evolves into a contracting direction, then one of the positive STLEs becomes negative (and vice versa if the number of expanding directions increases). Therefore, for a long trajectory, UDV will manifest itself as a fluctuation about zero of one or more STLE.

The existence of UDV means that there are trajectories which pass through regions with locally different numbers of positive STLEs. The change in sign of one or more of the STLEs is usually used in numerical experiments to detect the presence of UDV and the associated obstruction to shadowing [DGSY94] but, as is discussed in Section 2.2.2, this is problematic when using experimental data.

1.2.11 Synchronisation

Synchronisation is the tendency for interacting systems to unify their motion in some way and can be observed everywhere in nature. For example, people strolling side by side will tend to walk in-step and fireflies coordinate their flashing to maximise the distance from which they can be seen. Christiaan Huygens was the first to report synchronisation in a physical context, for two clocks supported from a common beam [Huy01]. The two clocks were observed to keep time perfectly with each other and their pendula had exactly opposite motion at any one time. This occurred despite the clocks not having identical natural periods of oscillation; going out of time when separated across the room. Synchronisation of interacting oscillating systems has since been found in many natural systems and is an important phenomenon in the nonlinear sciences [PRK01].

Recently synchronisation has been shown to play a key role in interacting or spatially extended chaotic systems [BKO$^+$02]. Spatially extended systems can be reduced to a grid of coupled oscillators, with synchronisation between the motions of the discreet elements giving rise to spatial waves and patterns [Ble88]. For coupled and high dimensional systems, the transition from low to high dimensional dynamics is often associated with the loss of synchronisation of some of the variables of the system.

Two interacting periodic oscillators i, j, with natural (uncoupled) frequencies of oscillation ω_{0i} and ω_{0j}, are said to be synchronised if their frequencies when coupled change and become entrained such that $\omega_i = \omega_j$. When $\omega_{0i} = \omega_{0j}$, synchronisation causes the systems to become phase-locked completely in phase

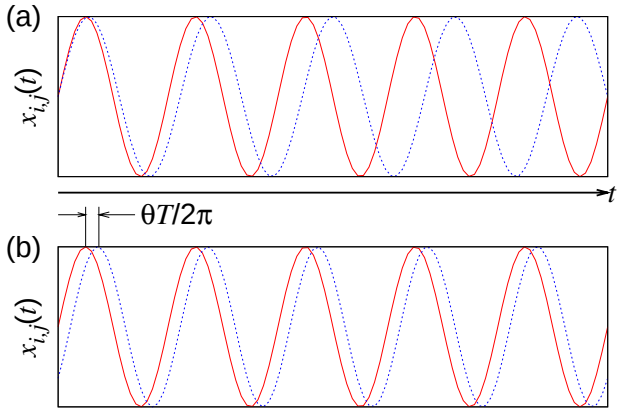

Figure 1.13: Synchronisation of periodic oscillations with different natural frequencies. The phase drift can be seen in (a) for the uncoupled case. When coupled, (b), a phase lag $\phi_j - \phi_i = \theta$ can exist between the synchronised oscillations.

(or totally out of phase) where the difference between their phases $\phi_j - \phi_i = 0$ (or $\phi_j - \phi_i = \pi$). A difference in the natural frequencies $\omega_{0i} > \omega_{0j}$ can result in a phase lag, $\phi_2 - \phi_1 = \theta$ between their oscillations, with the system of higher natural frequency leading slightly (Fig. 1.13).

The synchronised state exists within a range of frequency mismatch (or *detuning*) between ω_{0i} and ω_{0j}. If the detuning is larger than the stability threshold for a particular coupling strength, synchronisation is lost and the motion is on a torus in phase space. As the strength of the coupling is varied, the range of detuning for which the synchronised state is stable changes, becoming narrower for weaker coupling. For coupled higher dimensional or chaotic oscillators with subsystems having dimensions N and M, the combined phase space in the unsynchronised state has a dimension of $N \times M$. When the systems become synchronised some of the variables lose their independence and the number of degrees-of-freedom of the dynamics is reduced, with trajectories in phase-space being contained within a lower dimensional manifold called the *synchronisation manifold* (Fig. 1.14).

A system of two coupled oscillators can be considered as one unified system or as two interacting systems. In the latter representation the dynamics can

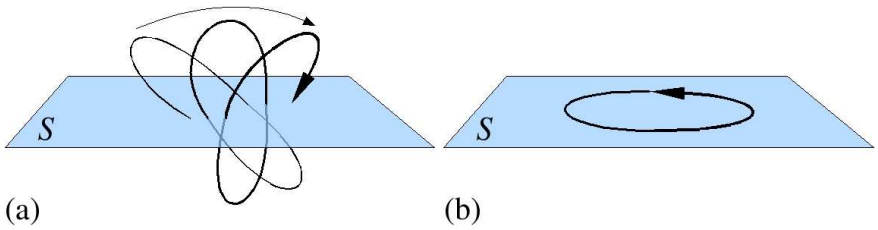

Figure 1.14: The synchronisation manifold S exists in a lower dimensional subspace within the $N \times M$ total phase space of the system. Orbits in the uncoupled case, (a), explore the full $N \times M$ space, whereas when synchronised, (b), orbits are restricted to S.

synchronise so that the two systems behave in a unified manner. This raises the question of whether or not a coupled system can be considered as a single system for all values of the coupling strength or whether there is some threshold value. This is also an important point when considering spatially extended systems. If some threshold value exists, below which the subsystems are not unified, the implication is that spatially separated parts of the system that have a weak connection below this value are not deterministically connected. Therefore taking measurements in one part of the system may give little or no information about the system as a whole. On the other hand, when the different parts of a system experience synchronisation it is hoped that ideas from low-dimensional chaos could be applied to such phenomena as spatiotemporal chaos or fluid turbulence.

In the case of simple oscillations synchronisation refers to an entrainment of the frequencies of the sub-systems either to each other or to some external drive. However, for chaotic oscillations the situation is somewhat more complicated. Various types of synchronisation have been identified and the broad categories are outlined here, from stronger to weaker respectively.

Complete Synchronisation

Perfect synchronisation of chaotic signals was first noted by Pecora and Caroll [PC90]. In this work they observed the complete synchronisation of two interacting systems, where both the frequency and amplitude of the two systems were

perfectly matched. This is variously termed *complete synchronisation*, *identical synchronisation* and *perfect synchronisation*.

Complete synchronisation (CS) can be considered a stronger definition of synchronisation than that of periodic oscillations, for which there is no requirement regarding the relative amplitudes. For CS, the observables of the subsystems follow each other exactly and the dynamics of the combined system resemble that in an individual system, the number of degrees of freedom being reduced accordingly. In the combined phase-space of the system CS manifests itself by trajectories becoming contained in the synchronisation manifold $S \in \mathbb{R}^N$, where $N = M$ is the dimension of the individual uncoupled subsystems.

Synchronisation in this case comes about when the unstable periodic orbits (UPOs) contained within the attractors of the interacting systems become locked with their counterparts, in a similar manner to phase locking in stable limit cycles. A difference in the natural frequencies of the subsystems can lead to a phase difference appearing, as in the synchronisation of simple oscillations. In this case, where the amplitudes of the subsystems are matched but follow with a phase lag, the phenomenon is known as *lag synchronisation*.

Generalised Synchronisation

The next strongest type of synchronisation between interacting chaotic systems is where there is not an exact match between the amplitudes of subsystems but there still exists some (often complicated) functional relationship which maps states from one subsystem onto the next:

$$x_2 = g(x_1). \tag{1.9}$$

This *generalised synchronisation* (GS) implies a one-to-one equivalence between states in the subsystems [RST95].

The existence of GS implies that the two subsystems can still be considered as a single unified system, as it is possible through some smooth functional transform

to project one subsystem onto the other. Therefore if (1.9) is satisfied there still exists a synchronisation manifold, $S \in \mathbb{R}^L$, in the $N \times M$ combined phase space, on which the dynamics are restricted. Also, in spatiotemporal systems this form of synchronisation is important for spatial structures such as waves and patterns to exist. When these systems are decomposed into a discreet grid, the variables of neighbouring elements need to be related to each other by some smooth mapping.

The degree of GS is related to the number of positive Lyapunov exponents in the system, with its onset characterised by a positive Lyapunov exponent crossing zero [OHZ$^+$03]. Two uncoupled, three degrees-of-freedom chaotic oscillators will each have one positive Lyapunov exponent, corresponding to the direction locally in phase-space in which the amplitude varies. The existence of only one positive Lyapunov exponent in the coupled system implies that the amplitudes of oscillation of the two subsystems have become dependent. Synchronisation in this case is therefore strongest where there is only one expanding direction to the flow and the dynamics are restricted to a synchronisation manifold S. Here, the amplitudes are strongly correlated and GS is easily detectable, despite S having a more complicated structure than for complete synchronisation. Where there is more than one positive Lyapunov exponent and a corresponding number of directions of instability to the flow, the dimension of the synchronisation manifold is increased. This can occur when the UPOs contained within the attractors bifurcate and become unstable transverse to the synchronisation manifold [KMP00]. In these cases correlations between amplitudes are much weaker (if they exist at all) and GS can not be measured using current methods. The degree of GS is therefore related to the number of expanding directions and the local dimension of the attractor in phase space. However, it has also been shown in [SBK$^+$02] that, if $g(x)$ is not a smooth function and contains wrinkles or is otherwise non-differentiable the detection of GS is unlikely, even in cases where there is unification of the two systems.

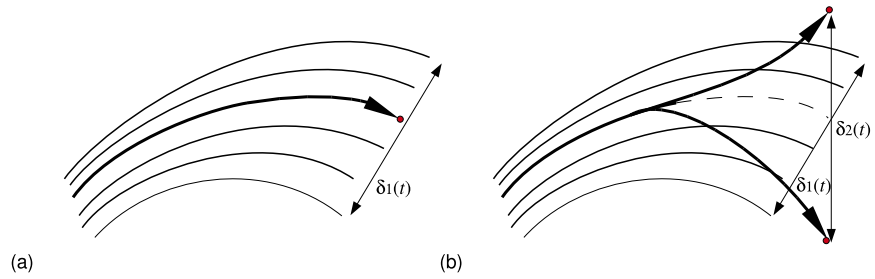

Figure 1.15: Bifurcation of a UPO in the stable manifold, leading to the emergence of a second positive Lyapunov exponent in the system. In (a) there is only one unstable direction to the flow locally. As UPOs begin to bifurcate, as in (b), a second expanding direction begins to develop and trajectories can explore a higher dimensional phase-space.

Loss of Generalised Synchronisation

Strong generalised synchronisation is lost when a second Lyapunov exponent emerges in the system and the synchronisation manifold loses a transverse direction of stability. This can happen when unstable periodic orbits (UPOs) that compose the stable manifold bifurcate and become expanding along one of their previously contracting directions, [KMP00]. This is shown schematically in Figure 1.15.

The first occurrence of a bifurcation of a UPO is known as a *riddling bifurcation*, after which point trajectories intermittently deviate from the low-dimensional synchronisation manifold along the bifurcated orbits. As the parameter is further increased and more UPOs bifurcate, the local topology of the manifold expands into a higher dimension. The system becomes hyperchaotic, with a second positive Lyapunov exponent emerging, when trajectories spend equal amounts of time near 1D and 2D unstable orbits. This point is known as the *blowout bifurcation* and is a result of a balance between bifurcated and un-bifurcated UPOs. Between the bifurcation of the first UPO and the point where the last one becomes transversely unstable there exists a mixture of UPOs with different numbers of expanding directions: a case of unstable dimension variability.

Phase Synchronisation

Synchronisation in its most general sense is the observed locking of the phases of interacting systems. Two subsystems can still have a degree of synchronisation, even when the conditions for the detection of GS break down, if the frequencies of the oscillations remain entrained and phase locking can be measured. This weaker definition of synchronisation is known as *phase synchronisation* (PS) [RPK96]. In its weakest form, phase synchronisation exhibits no correlation of amplitudes and so called generalised synchronisation is not present. The phase synchronised state has been identified in various biological systems from disease cycles in populations to the communication between neurons in different areas of the brain [RPK$^+$01; He03].

For two coupled chaotic oscillators, the transition between chaos and hyperchaos (with one and two positive Lyapunov exponents, respectively) is associated with the transition between generalised and phase synchronisation [PRZ$^+$99]. The existence of a single Lyapunov exponent at zero indicates that the flow (equivalent to the phase) is unique and the individual phases are locked together. The directions in which the amplitudes vary are the locally expanding (unstable) dimensions, characterised by the positive Lyapunov exponents. Therefore the transition to two positive Lyapunov exponents is the point at which the two subsystems develop independent amplitude variations and generalised synchronisation is lost.

The appearance of phase synchronisation is also important when considering whether the individual subsystems can be thought of as one combined system. In cases where the phase angle of oscillations $\phi(t)$ can be defined, the zero Lyapunov exponent, which characterises the direction of the flow, follows the angle of rotation of the oscillations in phase-space. Therefore, if the individual phases $\phi_i(t)$ and $\phi_j(t)$ of two subsystems i and j are locked and rotate together, the coupled system has only one zero Lyapunov exponent and the oscillations are acting together [PRK99].

Loss of Synchronisation

In certain regimes below the threshold for PS the oscillations can suffer intermittent slips in the phase. In this *imperfect phase synchronisation* (IPS) the phases are neither locked nor cycling continuously. The relative phases lock for intermittent periods of time before there is a 2π phase slip where the oscillators separate in phase until once again locking.

Away from the synchronisation regime the system can develop a second zero Lyapunov exponent and trajectories explore the complete $N \times M$ phase space of the system. Below the threshold of IPS each subsystem must be considered separately from its companion. Although each is perturbed by the other's motion, one cannot be used to ascertain anything about the current state of the other.

Summarising, the scheme for the degree of synchronisation of two interacting chaotic oscillators is as follows. Uncoupled (or below the synchronisation threshold), phases are independent and there are two Lyapunov exponents at zero, corresponding to two independent directions of flow. At the onset of phase synchronisation a zero Lyapunov exponent becomes negative and the phases rotate together but there are still two positive Lyapunov exponents (hyperchaos), with amplitudes uncorrelated between the subsystems. The system moves from hyperchaos to chaos as a positive Lyapunov exponent becomes negative the amplitudes become dependent and generalised synchronisation exists. The strongest form of synchronisation is where there is complete one-to-one equivalence of the amplitudes, giving rise to identical synchronisation.

1.3 Summary

In this chapter, the importance of nonlinear dynamics and complex systems to phenomena in the natural world has been discussed. Various aspects of the dynamics of nonlinear systems have also been introduced. It was seen that high dimensional systems can be represented as systems of coupled lower dimensional

subsystems. When these ensemble systems are composed of oscillators, the interaction between them to create the global dynamics can be understood in terms of the degree of synchronisation between the subsystems. The increase in complexity that can develop when the dimension of the problem is increased has been outlined, along with ways in which the dynamics can behave like a lower dimensional system through synchronisation of the variables. The relationship between synchronisation states and the transition to hyperchaos has also been introduced. When highly synchronised, the dynamics exist on a lower dimensional manifold but as synchronisation is lost the system experiences higher dimensional dynamics, with hyperchaos developing in the system. Phenomena can then occur in higher dimensional attractors which create problems for modelling, such as UDV, and it will be useful to be able to identify when such behaviour is present.

In the following chapters these concepts will be further developed, especially with regard to their use in analysing the behaviour of real physical systems. In Chapter 2 the numerical and experimental techniques used in the investigation of these phenomena are explained. A more detailed description is given for a new technique for determining the local dimension in Chapter 3, which is used for detecting UDV and also identifying invariant sets and helping to determine local Lyapunov exponents and shadowing times.

Systems of nonlinear oscillators are described in Chapter 4, along with an experimental configuration used for investigating these phenomena and testing the methods introduced in Chapters 2 & 3. In Chapter 5 the results of a study of the high-dimensional dynamics found in the system, particularly UDV, are presented and in Chapter 6 the origins of hyperchaos in the system are investigated.

Chapter 2

Numerical and Experimental Methods

The main difficulties in dealing with nonlinear systems, especially in chaotic regimes, are the analytical insolubility of the equations and the large amounts of data needed to get an accurate representation of the complexity in chaotic flows. Fortunately, as well as automating the process, computers reduce by many orders of magnitude the time needed to numerically calculate solutions to the equations and analyse the data from experiments. Some of the main techniques employed are outlined in this chapter, with emphasis on those used to produce the results presented in the subsequent chapters.

2.1 Numerical Methods

2.1.1 Solving Nonlinear Equations

Systems of ODEs can be solved numerically by integrating on a computer. The basic principle behind this is to take the gradient of the equations of motion about a point in its trajectory and extrapolate the motion for some small time, such that the linear approximation holds. Continuous iteration of this process

can yield an approximation to the true solutions of the equations. The Runge-Kutta method, a fourth order integration technique, is often used to follow the trajectories of systems [PTVF92]. This technique evaluates the trajectory at several intermediate points in a small time-step h, giving an integration of the motion which is usually reliable if h is small enough. It also has the advantage of ease of implementation and is used extensively for solving dynamical systems.

This method of following a dynamical solution of the equations of motion can be used as part of techniques to evaluate measures of the attractor and the data thus generated can be compared to that from experimental time-series.

2.1.2 Calculating Lyapunov Exponents

When the equations of motion are known it is possible to evaluate the Jacobian matrix of partial derivatives to give the linearised flow about each point. From this the Lyapunov exponents can be determined by calculating the average rates of expansion and contraction of small vectors for long trajectories in phase space.

The method of Benettin *et al.* [BGGS80] does this by iterating a set of orthogonal vectors forward for some small time, h, and determining the orientation of the principal directions of expansion and contraction from the stretching of these vectors, as shown in Figure 2.1. It is necessary to periodically re-orthogonalise the set of vectors, as they will tend to align with the most expanding direction, and would otherwise become degenerate. The lengths of the vectors also require periodic renormalisation to keep them within the linear approximation. Therefore, the magnitude of stretching is recorded before the vectors are re-orthogonalised and their lengths normalised. The process is then repeated for many iterations over a long trajectory.

2.1.3 Separating Invariant Sets

In higher dimensional systems attractors can be composed of various sub-sets (or *invariant sets*) with different internal dynamics, such as in a system experiencing

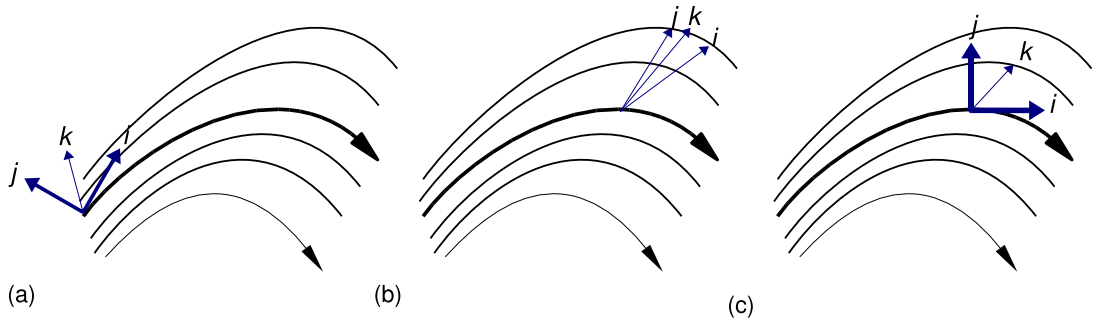

Figure 2.1: Numerical method of Benettin for determining Lyapunov exponents. (a): A set of orthogonal unit vectors $(\underline{i}, \underline{j}, \underline{k}, \dots)$ is defined on the linearised flow. (b): The flow is evolved for a time long enough for the vectors to grow and begin to align with the direction of maximum expansion but short enough for the lengths to remain independent. (c): The magnitudes of the vectors $(|i|, |j|, |k|, \dots)$ are recorded before the set is orthogonalised with respect to the direction of maximum expansion and their lengths re-normalised.

UDV. It is therefore useful to be able to identify such sets and even separate them so as to measure their properties independently.

A numerical algorithm for identifying and separating invariant sets is the PIM-simplex method of Moresco *et al.* [MD99], which can also be used for following unstable chaotic saddles which would otherwise be transient. In this technique a simplex of points is initiated near to a set of interest and the times calculated for trajectories originating from these points to escape a bounding region. These boundaries are defined such that they isolate any sets which are not part of the one under investigation. By means of a maximisation procedure the simplex is continuously redefined until its points straddle a local maximum of the escape time. The points in the simplex can be used as approximation of points in the real invariant set, as these have infinite escape time. Continuing the process from this point a trajectory is integrated until the next mapping, at which point the sequence is repeated, giving an approximation to the true invariant set.

2.2 Time Series Analysis Techniques

One of the principal advances in the field of nonlinear time-series analysis has been the realisation that information on attractors in the system can be obtained from time-series measurement, and techniques have been developed to extract as much dynamical information as possible from available data [BK86].

2.2.1 Attractor Reconstruction

The understanding of chaotic systems relies heavily on being able to represent the attractors of the system in phase-space. However, it is rarely possible to measure all the degrees of freedom of a real physical system. In the most limiting case it is only possible to record one of the dynamical variables, which may or may not be a variable in the equations of motion. However, all is not lost, as it is possible to reconstruct the attractors from a time-series of measurements of just one observable.

In the case of the simple pendulum, undergoing simple harmonic motion, the dynamical variables are the angle ϕ and angular velocity $\dot{\phi}$, both of which are needed to completely define a state of the system. However, if it were only possible to measure the angle $\phi = \sin(t)$, differentiation would give the velocity $\dot{\phi} = \cos(t)$. An alternative for transforming $\sin(x)$ to $\cos(x)$ is through a phase shift, $\cos(x) = \sin(x + \frac{\pi}{2})$. Thus using the *delay coordinates* $\phi_1 = \sin(t)$ and $\phi_2 = \sin(t + \frac{T}{4}) = \cos(t)$, where T is the period of oscillation, gives an equivalent reconstruction of the dynamics in phase space (Fig. 2.2).

Fortunately, this principle is useful not only for simple harmonic motion, but can be extended to complicated or chaotic oscillations in higher dimensions. The embedding theorem of Takens [Tak81] gives proof that reconstructions of attractors based on successive differentiation or, more commonly, a series of delay coordinates are topologically equivalent to the original attractor. This means that invariant quantities defined on the attractor such as the fractal dimension

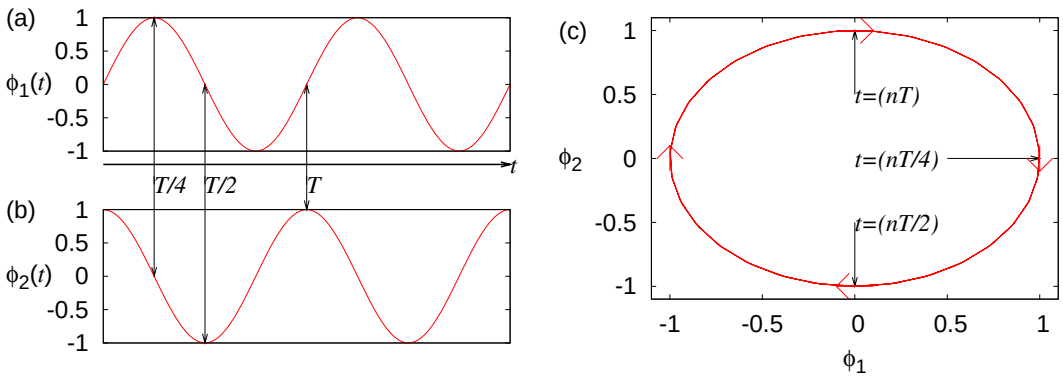

Figure 2.2: Delay coordinates. In the case of a pendulum undergoing simple harmonic motion, a single variable $\phi_1(t)$, (a), can be used to reconstruct the true two-dimensional phase-space, (c). The second variable, (b), is constructed using a time-delay of the first such that $\phi_2 = \phi_1(t + \frac{T}{4})$, where T is the period of oscillation.

and Lyapunov exponents are preserved under the transformation from the full system to one constructed from delay coordinates.

Therefore, given a time-series of measurements $[w(0), w(\delta t), \ldots, w(N\delta t)]$ of some smooth function of the state of the system taken at a constant, appropriately chosen sampling rate δt, the orthogonal vector coordinates of points $x_{i,j,k,\ldots}(t)$ in the reconstructed attractor are defined thus:

$$\begin{aligned} x(t) &= [w(t),\ w(t+\delta t),\ w(t+2\delta t),\ \ldots,\ w(t+(\nu-1)\delta t)], \\ &\equiv [x_i(t),\ x_j(t),\ x_k(t), \ldots], \end{aligned}$$

where ν is the embedding dimension of the attractor. The embedding dimension is technically defined as up to $2\eta + 1$, where η is the dimension of the state space manifold. However, practically the system can often be embedded in a lower dimension, which can be determined by various methods (see Sec. 2.2.3). Using this technique as a basis, many of the mathematical results that can be derived from models of dynamical systems can be applied to real physical data.

2.2.2 Measuring Lyapunov Exponents

By taking a set of nearby initial points and calculating their evolution around the attractor it is possible to evaluate the average rates of attraction and divergence and hence the Lyapunov exponents of the system. Lyapunov exponents quantify the rate of exponential expansion or contraction of volumes over the whole of a given attractor, and can be calculated by averaging over a very long trajectory the local expansion and contraction of segments linking nearby points on the embedded attractor.

The method of Wolf *et al.* is similar to the numerical technique of Benettin, except that real data points are followed, rather than vectors in the linearised flow [WSSV85]. Wolf's method works by defining some small region, $B_\epsilon(\mathsf{x})$, of radius ϵ around a trajectory point, x. All embedded points falling within $B_\epsilon(\mathsf{x})$ are identified and those best aligned with the orthogonal directions selected. The divergence and contraction of these points is then followed along sections of a trajectory, so long as these sections are short enough that the flow is approximately linear (Fig. 2.3). These points have to be replaced periodically and with sufficient frequency to ensure that the vectors generated by them stay orthogonal and their size small enough for the linear approximation to remain valid, whilst also allowing for the expansion and contraction rates to be numerically computable.

Short-Time Lyapunov Exponents

In numerical studies the detection of UDV is carried out by estimating the short-time Lyapunov exponents. For experimental data, this would require using Wolf's method but over short trajectories to evaluate the local rates of expansion and contraction.

Although the amount of data that can be obtained from electronic oscillator systems would appear to be sufficient for this, the random fluctuations in the number of points in a given region means that frequently a suitable replacement point cannot be found when orthogonalisation is required, making the short time

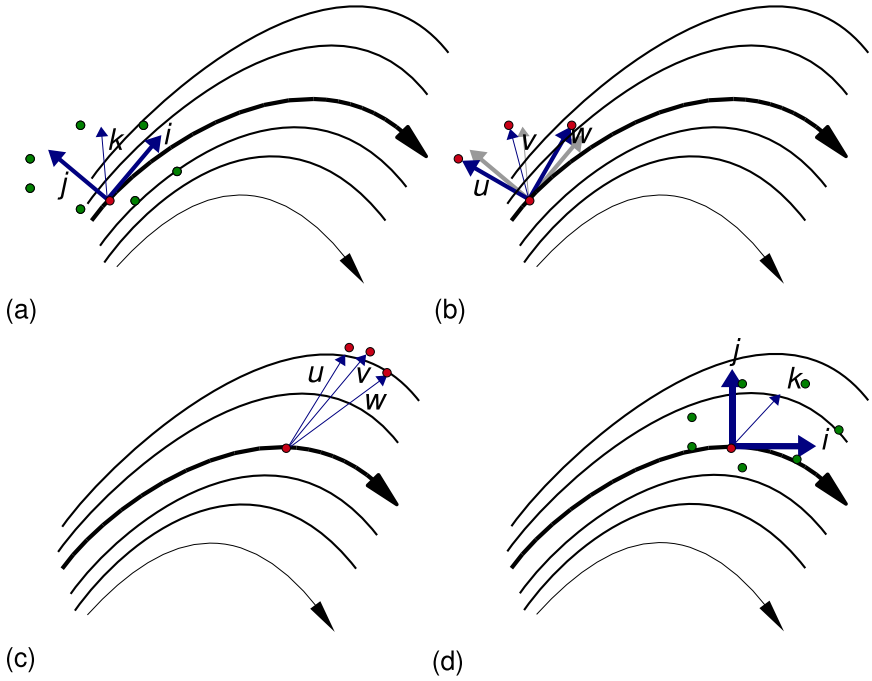

Figure 2.3: Wolf's method of determining Lyapunov exponents from time-series data. (a): A set of orthogonal vectors $(\underline{i}, \underline{j}, \underline{k}, \dots)$ is defined around a trajectory point in the reconstructed attractor. (b): The neighbouring embedded points within a small radius are found and the points $(\underline{u}, \underline{v}, \underline{w}, \dots)$ which are most aligned with the orthogonal set identified. (c): The points are followed for a time long enough for them to begin to move towards the direction of maximum expansion but short enough so that their distances remain approximately small enough for the linear assumption to be approximately valid. (d): The growths of the distances $(|u|, |v|, |w|, \dots)$ are recorded before a new orthogonal set of $(\underline{i}, \underline{j}, \underline{k}, \dots)$ are defined, aligned with respect to the direction of maximum expansion, and a new set of neighbouring points found.

averages less reliable. This is a particular problem when the radius ϵ is reduced to a size necessary for $B_\epsilon(\mathsf{x})$ to be a good approximation to the linear tangent space of the local manifold. This is especially pronounced where the data are more sparse due to being spread into higher numbers of dimensions locally, such as in hyperchaotic regions.

It is also a requirement that one of the vectors be aligned along the direction of the largest STLE. However this direction is not known *a priori*, so the vectors need to be allowed to evolve for some time before the expansion and contraction rates can be calculated reliably. This alignment will in general be lost when the trajectory reaches a non-hyperbolic point, thus reducing the actual number of points available to estimate the STLEs. All of these requirements make this technique very sensitive to adjustments to the parameters of the calculation, as well as being very unreliable due to a low density of points in the contracting directions. An alternative method for identifying the existence of UDV and estimating the STLEs is described in Chapter 3, which is based on measures of the local attractor dimension.

2.2.3 Measuring the Local Attractor Dimension

The local topological dimension of the attractor is directly related to the number of expanding directions, giving an alternative way to determine variations in the number of unstable dimensions.

Measures of attractor dimension can also be used to determine the best dimension in which to embed a time-series for attractor reconstruction. A common way of determining the embedding dimension is using the *false neighbours* method [KBA92]. Here, the separation of nearby points is evaluated and tracked as the dimension of the embedding is steadily increased. If the dimension is too small, points that are not neighbours in the real system but appear nearby on projection into a lower dimensional space will separate as the dimension is increased. Once the average separation of neighbours reaches a definite value the ideal embedding

dimension has been found. There are also techniques to calculate the actual fractal dimension of the attractor, but they are of little practical use in the context of detecting UDV.

Several methods have been proposed to determine the local topological dimension of the manifold containing the attractor [FCF+81; BJK87; HPF90]. The method of Froehling *et al.* [FCF+81] attempts to fit the data to the local tangent space by means of linear regression. This is repeated for increasing dimension of fit, until the correct dimension is determined from the χ^2 values obtained. Therefore the method relies upon the linear approximation being valid in the region from which the data are taken. This means that the radius of the local region containing the points must be small enough to ensure minimal curvature. This is in competition with the need for the level of noise in the contracting directions to be small compared to the radius of the set of points under investigation and with having a region big enough that it contains sufficient points for the analysis to be reliable.

Alternatively, the method of Broomhead *et al.* [BJK87] studies the singular values of the matrix whose rows consist of the vectors connecting the points in the local region $B_\epsilon(\mathsf{x})$ to its centre. The number of significant singular values is expected to be equal to the dimension of the local tangent space, assuming it is well approximated by $B_\epsilon(\mathsf{x})$. However, the presence of noise will give the attractor some thickness in all the contracting directions in phase space. If the radius of the local region, ϵ, is increased beyond the noise threshold, the singular values corresponding to non-contracting directions will increase linearly with ϵ while the singular values of the contracting directions will remain constant until the curvature of the set becomes relevant, thus making it possible to distinguish expanding directions from noisy contracting ones.

Similar difficulties to Froehling's method arise in these techniques and also that of Hediger [HPF90], which also makes use of singular value decomposition. For this reason, a technique based on the statistical averages of distances in

the embedded attractor was developed as an alternative, which is described in Chapter 3.

2.2.4 Measuring Chaotic Synchronisation

The ease of detection of synchronisation in chaotic systems depends on the type of synchronisation encountered. Identical synchronisation can be seen easily by plotting the dynamical variables $x_1(t)$ and $x_2(t)$ of the coupled subsystems O1 and O2 against each other. As in the case of synchronisation of periodic oscillations, if $x_1(t) = mx_2(t)$, where m is a constant, a straight line of slope m will be seen. However, more sophisticated techniques are required when trying to identify weaker forms of synchronisation.

Generalised Synchronisation

The condition for generalised synchronisation is that there exists some smooth functional relationship $x_2 = g(x_1)$ between dynamical variables $x_1(t)$ and $x_2(t)$ of the coupled subsystems. This implies that the amplitudes of the oscillations are correlated in some way and nearby trajectories in one subsystem will also be neighbours in the other. This property can be used to detect generalised synchronisation (GS) between them. A common method of achieving this is to perform an ε–δ test on the time-series of the subsystems [BJM$^+$03]. In the case of two coupled subsystems, the attractors of each are first reconstructed using the techniques described above. A point $x_1(t_{k0})$ on a trajectory in the first subsystem is chosen and a hypersphere of small radius δ defined (Figure 2.4). A set of embedded points $(x_1(t_{k1}), x_1(t_{k2}), \dots)$ which lie within δ are then found. The points in the second subsystem $(x_2(t_{k1}), x_2(t_{k2}), \dots)$ at corresponding times are identified and their distances ε from the point $x_2(t_{k0})$ calculated. In many cases, total lack of synchronisation can be seen immediately by choosing a small radius δ to give a compact set of points S(δ) in the first subsystem and looking at the set of corresponding points in the second, S(ε). If points in S(ε) are spread

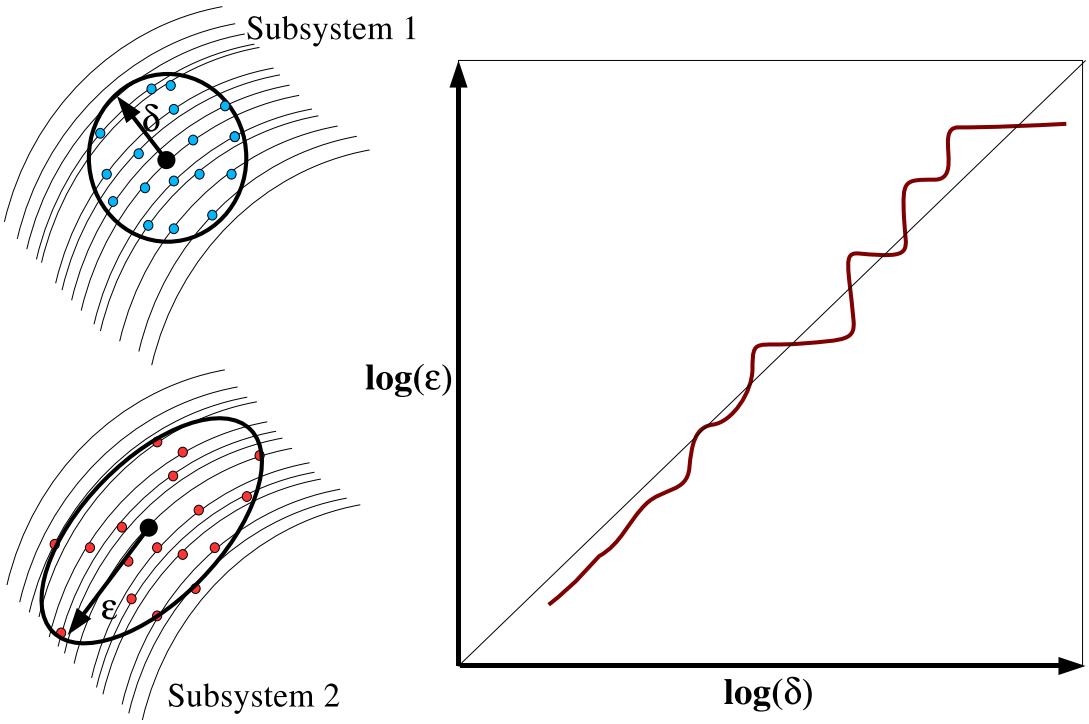

Figure 2.4: Measuring generalised synchronisation by looking at correlation of embedded points. Data-points on a trajectory of one subsystem are found within a radius δ along with the corresponding points in the second subsystem. The distances to points in the second subsystem ε are identified, and the maximal distance is plotted against δ for a range of δ.

across the whole of the attractor, it can be reasonably assumed that there is little or no synchronisation of the trajectories. A concentration of points in S(ε) would indicate that some form of generalised or phase synchronisation exists, but further analysis is needed to positively identify the true synchronisation dynamics.

In ε–δ tests, distances of points in each subsystem from their respective origin are compared. The usual technique is to find the maximal distance ε_{max} for Subsystem 2 as a function of decreasing δ in Subsystem 1. If $g(x)$ is differentiable, $\varepsilon_{max} \to 0$ linearly as $\delta \to 0$ [SBK$^+$02]. This results in the gradient $\log \varepsilon / \log \delta$ approximating unity in the region close to x where $g(x)$ is approximately linear. The technicalities here are necessary only as far as rigorous mathematical proof is concerned and often GS can be implied by using weaker forms of this method.

It is possible to say that GS exists simply by observing a positive correlation between points in δ and ε.

Generalised synchronisation can disappear as the unstable periodic orbits (UPOs) within the attractor bifurcate and lose an extra dimension of stability [KMP00]. The locking of these UPOs is the basis of chaos synchronisation and as they bifurcate the synchronisation manifold extends into a higher dimension than previously. As bifurcations of UPOs occur, the attractor becomes riddled with holes and trajectories intermittently deviate from the low-dimensional surface, causing the local topology of the manifold to expand into a higher dimension. This increase in the local topological dimension is one other possible way to detect a reduction in synchronisation.

Phase Synchronisation

Phase synchronisation is defined when there is no detectable correlation between the magnitudes of oscillations of the subsystems but their phases are still locked. This can occur in a system of two coupled three degrees-of-freedom chaotic attractors when there are two positive Lyapunov exponents. The existence of two directions of expansion to the flow implies that each subsystem has its own expanding direction, which is related to the local direction in which the amplitudes vary [PRZ+99].

It is often possible to see phase synchronisation by performing steps of the above method for generalised synchronisation and looking at the spread of points in S(ε) for some small δ (Fig. 2.5). Phase synchronisation will usually appear as points in S(ε) being restricted to some phase angle, but spread across all amplitudes. However, to positively identify if phase synchronisation exists it is necessary to be able to define the phase of the oscillations of each subsystem. While this is easy for periodic and certain complicated oscillations with a definite focus, it is often a nontrivial task, especially in highly complicated flows with no obvious centre of rotation.

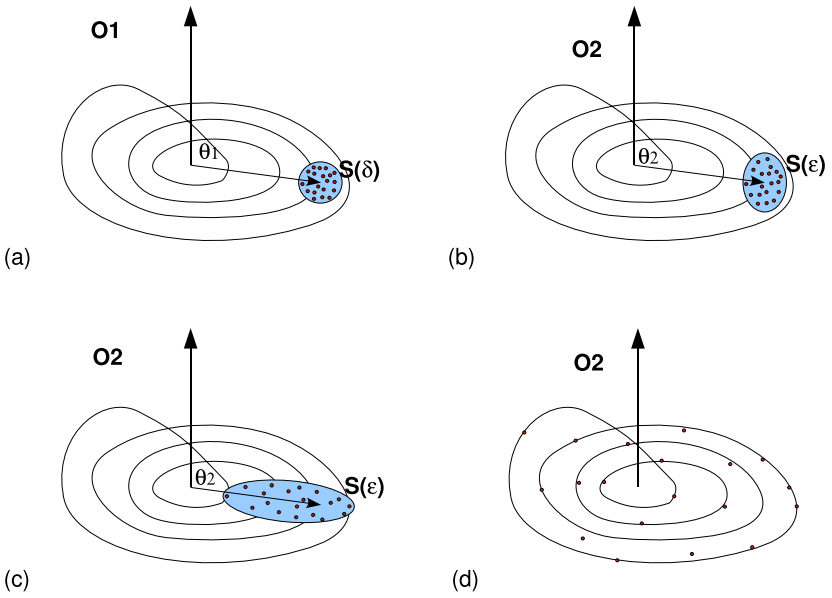

Figure 2.5: Synchronisation and embedded points. (a): A compact set of points S(δ) is chosen in one subsystem, **O1**. The corresponding set S(ε) in the other subsystem is then observed. (b): For generalised (or stronger) synchronisation, both the phase-angle θ_2 and the amplitudes of S(ε) are bounded. (c): When the subsystems are only phase-synchronised, θ_2 is bounded, but S(ε) is spread over all amplitudes. (d): In the unsynchronised case, points cover the whole of the attractor of the second subsystem, **O2**.

One way to unambiguously obtain the phase of an oscillation is through performing the Hilbert transform $x_H(t)$ on $x(t)$. The Hilbert transform is defined as:

$$x_H(t) = \pi^{-1} \int_{-\infty}^{\infty} \frac{x(t)}{t-\tau} d\tau, \tag{2.1}$$

where the integral is taken at the Cauchy principal value. This can be computed from real data using the fast Fourier transform (FFT), via the following steps [PRK01]:

1. $y(\omega) = \mathrm{FFT}[x(t)]$,
2. $\Re[y(\omega)] \Leftrightarrow \Im[y(\omega)]$,
3. $x_H(t) = \mathrm{FFT}^{-1}[y(\omega)]$.

Swapping the real and imaginary parts of $y(\omega)$ in step 2 effectively phase-shifts the frequency components of $y(\omega)$ by $-\pi/2$. The phase and amplitude at any point in time can then be obtained from the *analytic signal*:

$$\zeta(t) = x(t) + ix_H(t) = A(t)e^{i\phi(t)}, \tag{2.2}$$

where the *instantaneous phase* is $\phi(t)$ and $A(t)$ is the *instantaneous amplitude*.

Plotting ϕ as a function of time can then reveal the transition to imperfect phase synchronisation by the appearance of intermittent 2π phase slips.

2.3 Summary

In this chapter an outline has been given of some methods for extracting useful information from nonlinear dynamical systems in chaotic regimes. At such parameter values analytical techniques usually fail and standard signal processing techniques give little useful information.

It has been demonstrated how numerical algorithms can be used to solve the equations of motion of nonlinear dynamical systems by integration. Extensions to these techniques were shown to be useful for calculating the Lyapunov exponents and separating invariant sets.

It has also been shown how the attractors of a system can be reconstructed from measurements of only one of its variables. Using this as a basis, quantitative measures such as the Lyapunov exponents and topological dimension can be calculated. Techniques have also been demonstrated which can identify synchronisation between different elements of the system.

Application of these methods to models of and time-series data from physical systems can yield a great deal of information about their dynamics where analytical and standard signal processing techniques fail.

In the next chapter a new method is described which can prove useful for identifying the existence of UDV in a system, as well as extracting invariant sets and making measurements on shadowing times and short-time Lyapunov exponents, all from time-series data alone.

Chapter 3

Method for Measuring Unstable Dimension Variability

3.1 Introduction

The loss of synchronisation and associated behaviour described in Chapter 1 are important phenomena and it is believed that an understanding of these will be vital in comprehending the higher dimensional dynamics to be found in systems with high numbers of degrees of freedom. Often such systems spend their time fluctuating between different invariant sets within the attractors of the system. If these subsets of the complete attractor have unstable manifolds of different dimension then unstable dimension variability (UDV) is present and serious limitations exist to the applicability of the shadowing theorem.

Unstable dimension variability has been shown in recent years to be a crucial factor in determining shadowing times in systems with more than three degrees of freedom. When faced with a real physical system, information on the presence of UDV will be necessary for determining the parameter ranges in which models and numerical simulations can be expected to give results that correspond to real states of the system. A method that can detect UDV from real system data would therefore be a useful tool in the study of systems with a moderate to high

number of degrees of freedom, such as those arising from reductions of systems of PDEs to a set of ODEs. Such a method would also be valuable for identifying non-attracting sets and determining their role in phenomena such as turbulence and spatiotemporal chaos.

The usual method for detecting UDV in numerical studies is to determine the short-time Lyapunov exponents (STLEs) of the system and look for fluctuations in the number of positive ones. Experimentally, however, the presence of noise and constraints in the amount of data available impose serious limitations on techniques available for measuring the Lyapunov exponents [ABST93], such as those described in Section 2.2.2. These methods rely on taking long time averages to obtain reliable values, which is not possible when trying to determine short-time information.

In this chapter a new method is discussed for detecting local unstable dimension in experimental data that does not require the calculation of STLEs.

3.2 Local Unstable Manifold and Topological Dimension

An alternative approach to detecting UDV is to measure the local topological dimension of points on the attractor and relate this to the dimension of the local unstable manifold. For a point x in an attractor $\mathcal{A}$, the region of the smooth manifold $\mathcal{M}$ around x, $\mathcal{M}_{\mathsf{x}}$, can be described by means of local stable and unstable manifolds and the corresponding linear tangent spaces [HP68]. Trajectories passing through $\mathcal{M}_{\mathsf{x}}$ will be displaced apart along the unstable directions and driven together along the stable directions, as described in Section 1.2.6. Therefore the trajectories inside $\mathcal{M}_{\mathsf{x}}$ will be organised in a way that is related to the local structure of the stable and unstable manifolds. The aim of this approach is therefore to determine the dimension of the linear subspace associated with the

(a) Expanding and neutral directions (b) Contracting and neutral directions

Figure 3.1: The distribution of points around a chosen trajectory point. Expanding directions, $\leftarrow \rightarrow$, and the neutral direction of flow (shaded arrow) show a spread of points, whereas contracting directions, $\rightarrow \leftarrow$, appear almost flat. Thus the dimension of the containing region is strongly related to the number of unstable dimensions.

expanding directions from the distribution of points belonging to these trajectories. Locally, the distribution of experimental data approximates the subspace spanned by the unstable and neutral (in the direction of the flow) directions, with a certain "thickness" in the stable directions due to noise (Fig. 3.1). So, for example, in the case where there is locally one expanding direction, the set of points will approximate a two-dimensional surface, while for two expanding directions the set of points will be distributed in an approximately three-dimensional volume.

When determining the dimension of sets of local data at various points for a long enough trajectory on the attractor, variations in the number of expanding directions would be revealed by variations in the local topological dimension. Therefore the approach here is to look at the local distribution in phase space of points belonging to numerous trajectories and calculate the local topological dimension on which those points sit and from this the number of locally expanding directions.

Like the calculation of STLEs, this approach also suffers to a degree from the presence of noise and a limited amount of data. However, the fact that this

method tries to estimate an integer value rather than to determine the sign of a quantity that can be close to zero makes it more robust in that respect.

As described in Section 2.2.3, several methods already exist to determine the local topological dimension of the manifold containing the attractor [FCF+81; BJK87; HPF90]. These methods can suffer due to the temporal fluctuations of the singular values induced by the presence of dynamical noise [TNS05], as well as from high curvature in the set at certain parameter values. It is for these reasons that the method described in the next section was developed, which is not only very easy to implement and can run its course unaided, but is also very robust to the levels of noise and curvature seen in the systems on which it was tested.

3.3 A Statistical Method for Determining the Local Dimension

Since it is the geometry of a set of points within a certain radius that needs to be determined, it is natural to consider whether there exists a simple geometrical measure that can be used to achieve this goal. An obvious differentiating feature of circles or spheres of different dimension is the ratio of their bounding surface to the area/volume contained within. Considering a number of points evenly distributed in volumes of different dimension, it can be seen that the average distance between points increases on increasing dimension. For example, the average distance between pairs of points is larger for a two dimensional disc of points than for a one dimensional line. This property holds for arbitrarily large dimension, with the mean distance between all pairs of points depending on the dimension of their distribution.

Hammersley [Ham50] looked at the distribution of distances between points uniformly distributed in hyper-spheres of different dimension. It was shown that, for an infinite number of points, the mean distance between them converges to a

Dimension, ν	Mean, $\mu_\nu(d)$	Variance, $\mathrm{var}_\nu(d)$
1	0.3333	0.05555
2	0.4531	0.04469
3	0.5143	0.03551
4	0.5521	0.02857
⋮	⋮	⋮
∞	0.7071	0.00000

Table 3.1: The mean distance between points uniformly distributed in unit diameter hyper-spheres of various dimension. Values obtained by Bennet [Ben69] from a result by Hammersley [Ham50].

characteristic value that depends on the dimension, ν, of the hyper-sphere. This result was found to be useful for determining the dimension of the space containing a given set of points, even if their number is finite and their distribution non-uniform. Although the presence of curvature and noise has a detrimental effect on the values obtained, this way of determining the local dimension of the set appears to be more robust than the other techniques mentioned earlier.

For points uniformly distributed in a hyper-sphere of dimension ν, the values of the mean inter-point distances $\mu_\nu(d)$ (normalised by the diameter of the hyper-sphere) and the corresponding variances $\mathrm{var}_\nu(d)$ for several values of ν, were calculated by Bennet [Ben69] and are included in Table 3.1.

The method described here for the detection of UDV works best on attractors reconstructed from time-series data using delay embedding or related methods, due to the inherent normalisation of the dimensions. Also it is important to not oversample the data, as this would lead to a small scale structure resembling a set of one dimensional lines in the direction of the flow. The procedure works by first defining a small hyper-spherical region around each point in a long trajectory on the embedded attractor and identifying all points contained therein. The distances between all the pairs of points in this neighbourhood are measured and their average ($\mu(d)$) calculated and normalised by the largest recorded distance.

To evaluate the robustness of this approach, the mean distances for numerically generated sets of points, randomly distributed and contained in spaces of different dimension were calculated. For example, a two-dimensional unit diameter disk of 800 randomly distributed points with a thickness in the third direction of 10% of the diameter of the disk gave a value of $\mu_\nu(d) = 0.4535$, which is very close to the value 0.4531 that corresponds to a two dimensional set. This approach is therefore expected to be successful in cases where data-sets are large enough that at each point of the embedded attractor it is possible to define a local region of phase space containing a few hundred points.

The method continues by repeating this procedure for a few successive points along the same trajectory and an average ($\bar{\mu}$) is obtained to smooth out local statistical variations. Once this has been carried out for a long trajectory, visiting most parts of the attractor, a histogram is produced to show the statistics of $\bar{\mu}$ for the whole attracting region. The histograms thus obtained will have peaks around the characteristic values shown in Table 3.1. Unstable dimension variability then shows up as multiple peaks in the histogram, each denoting a region with a given number of expanding directions. An example histogram produced using a numerically generated time-series from a model system is shown in Section 3.4.

3.3.1 Extended Applications of the Method

Separating Invariant Sets

In certain cases, the information gained from the application of the method can also be used to separate the embedded attractor into its regions of different unstable dimension. To achieve this it is necessary to define a threshold value of the local mean distances, μ^*, which corresponds approximately to the minimum between the peaks in the histogram. Points in the trajectory for which $\bar{\mu}$ is at either side of μ^* then have to be separated, given that these trajectory points exist in regions of different local topological dimension.

Measuring Shadowing Times

The presence of UDV generally implies a serious obstruction to shadowing, resulting in very short shadowing times. For the type of system used in later chapters, a typical trajectory can be decomposed into sections in which the behaviour is approximately hyperbolic and parts which correspond to the transitions between sets with different numbers of expanding directions. These *glitches* or changes of one direction in phase space from contracting to expanding (or vice versa) will generally lead to the exponential divergence between a true trajectory and a numerically generated pseudo-trajectory. The shadowing time is then directly related to the time between glitches and depends on the initial conditions of a given trajectory.

From the method of decomposing the reconstructed attractor into invariant subsets outlined above, it is possible to determine an approximation to the distribution of shadowing times by looking at the time a typical trajectory spends in the proximity of each invariant set, i.e. the times without variations in unstable dimension. To do this a suitable threshold value of the local mean distances needs to be defined, corresponding to the minimum between the peaks representing different topological dimension and then the number of time-steps between the points in the trajectory for which $\bar{\mu}$ crosses μ^* needs to be counted.

Measuring Local Lyapunov exponents

Once the attractor has been separated into its invariant sets it is possible to use the extracted subsets to calculate approximations to the local Lyapunov exponents, which are equivalent to short-time exponents for each set. To do this a technique such as Wolf's method needs to be applied separately to each of the sets and from this histograms of averages produced.

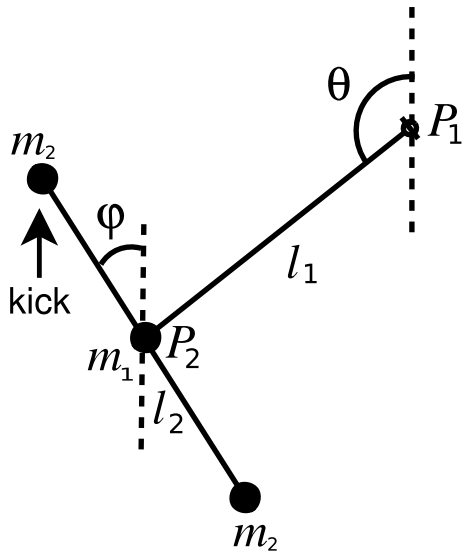

Figure 3.2: The kicked double rotor. Three masses (m_1, m_2, m_2) are attached to two massless rods, l_1 and l_2, which pivot at points P_1 and P_2. One of the masses is forced impulsively at periodic intervals.

3.4 Numerical Results

In order to test this method for the detection of UDV, it was applied to numerically generated time-series data from the kicked double-rotor system [GKOY87], which has previously been shown to contain UDV [MD97]. Figure 3.2 shows a diagram of the kicked double rotor system, which consists of three masses (m_1, m_2, m_2) attached to two massless rods, l_1 and l_2, which pivot at points P_1 and P_2. One of the masses is forced impulsively at periodic intervals, and the system is allowed to evolve continuously in between these "kicks". The motion is assumed to be restricted to a plane and the four dimensional system can be described by two angles, θ and φ, and the corresponding angular velocities.

A time-series was generated by integrating the equations of motion [GKOY87] between periodic "kicks", and $\sin(\theta)$ was embedded to reconstruct the attractor[1].

[1]Due to the large variations in the density of points between the different regions of the attractor, it was found to be necessary both to generate a large time-series (to "fill-out" the sparser, high-dimensional regions) and to take a random sampling of points in neighbourhoods

This was chosen for the embedding because the angular velocity variables are discontinuous at the kicks.

The method was applied to the embedded data for parameter values when the attractor is known to contain unstable periodic orbits with one and two expanding directions (see Figs. 9(d) and 10(d) in [MD97]). In Figure 3.3 it can be seen that the corresponding histogram shows definite peaks close to the values $\bar{\mu} = 0.4531$ and $\bar{\mu} = 0.5143$, as expected in the case of a trajectory visiting regions with one and two unstable dimensions. The spread of the peak for the higher dimensional region is found to be large due to the sparsity of points in this region resulting in statistical broadening. In Chapter 5 it will be shown that the method is also suitable for detecting the presence of UDV in time-series obtained from experimental measurements.

3.5 Summary

A method has been introduced to calculate the local topological dimension of an attractor and extract useful information on its structure and dynamics. This method only requires the calculation of distances between pairs of points, and as a consequence it is very easy to implement.

When investigating systems of increasing dimension, the size of the time-series needed to obtain enough embedded points for the method to succeed will also increase, along with the computer time required to calculate the values for the local dimension. This point is true of all time-series analysis techniques. The required size of the local data set, N, is expected to scale in a similar manner to that needed for calculations of the correlation dimension, which has been shown to scale as $N \sim 10^{\nu/2}$, where ν is the dimension of the set [ER92]. This is because the current method is based on the statistics of distances between pairs of points. The amount of data required for the calculation of Lyapunov exponents has been

where the density was very high (to quicken calculation in the high-density, low-dimensional regions).

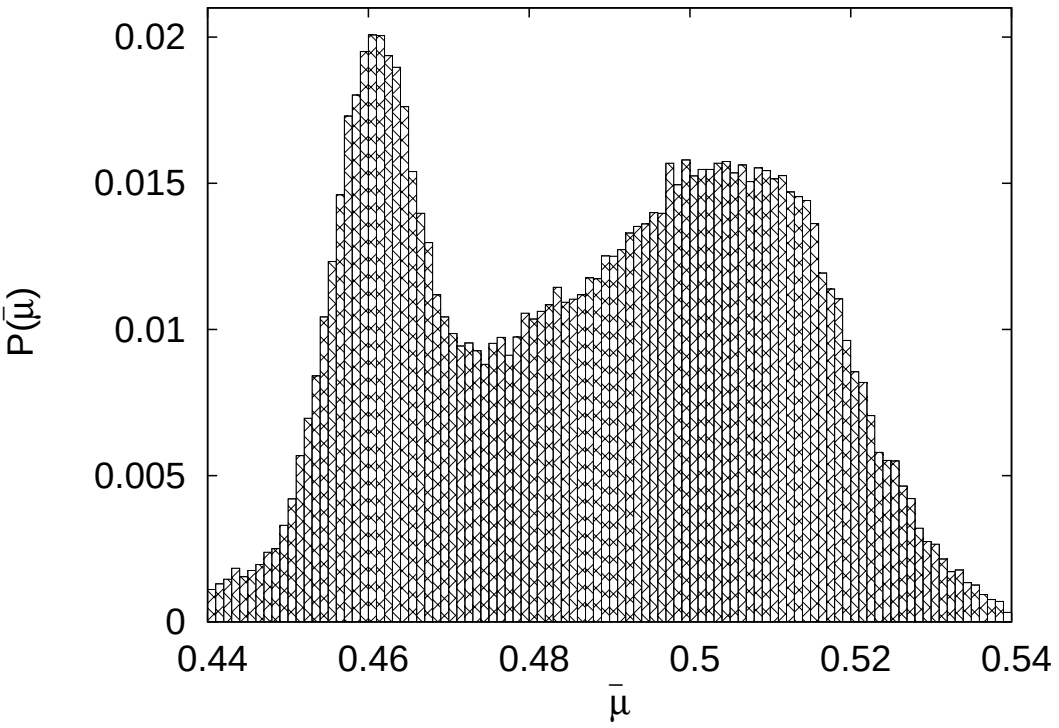

Figure 3.3: Distributions of local mean distances, $\bar{\mu}$, between points in the embedded attractor for the kicked double-rotor system. The distribution shows two peaks around the values corresponding to two and three dimensional distributions of points, in agreement with other results on this system confirming the existence of UDV.

shown to be approximately the square of that for the correlation dimension, demonstrating that the method introduced in this chapter compares well with other time-series analysis techniques.

As with other techniques, the presence of noise can have a detrimental effect but in the cases studied this method appears to be robust enough to yield useful information. In particular, small amounts of noise will induce a shift of the peaks in the histogram of $\bar{\mu}$ to higher values, giving the possibility of using the method as a tool for measuring the dynamical noise in a system as compared to the model situation.

Another limiting factor could be when the shadowing times become exceptionally short. In cases where the time a trajectory spends in regions with constant unstable dimension is shorter than the number of steps over which a useful average can be obtained for $\bar{\mu}$ (which can be taken as less than the length of a few typical orbital periods) the method will fail. However, in such cases trajectories will have little or no time to spread or converge into the new expanding or contracting subspaces and the attractor in such cases will exhibit no clear dimension.

However, in all cases studied the method was found to be more robust than other techniques attempted, and will prove useful in the study of experimental time-series data.

Chapter 4

Systems of Coupled Oscillators

4.1 Introduction

Systems capable of undriven self-oscillation can be found throughout nature. Neurons in the brain are well represented by individual integrate-and-fire oscillators, similar to the classical van der Pol electronic oscillator. Self-sustained oscillations are possible in systems where some force or charge is built to a certain threshold before being released, creating an oscillating output from a constant input.

A scheme for autonomous oscillation is shown in the cartoon system in Figure 4.1. Here a funnel cone of mass m is attached to the end of an elastic tube of length L. In some parameter regimes the tube bends by an angle θ dependent on the increasing product mL (Subfig. (a)). The qualitative nature of the equilibrium state of such a system with fixed m and increasing L depends on the ratio m/L. For certain values of m/L the bifurcation to the bent state is *supercritical*, with a unique value of θ for every mL (Subfig. (b)). In other regions of the m–L parameter space the behaviour is *subcritical* and there is hysteresis, with some retraction of the length necessary for the tube to "spring" back to its upright state (Subfig. (c)).

If a constant flow of water is fed into the tube in the hysteretic regime so that the mass in the cone can vary across the hysteresis range of mL oscillation

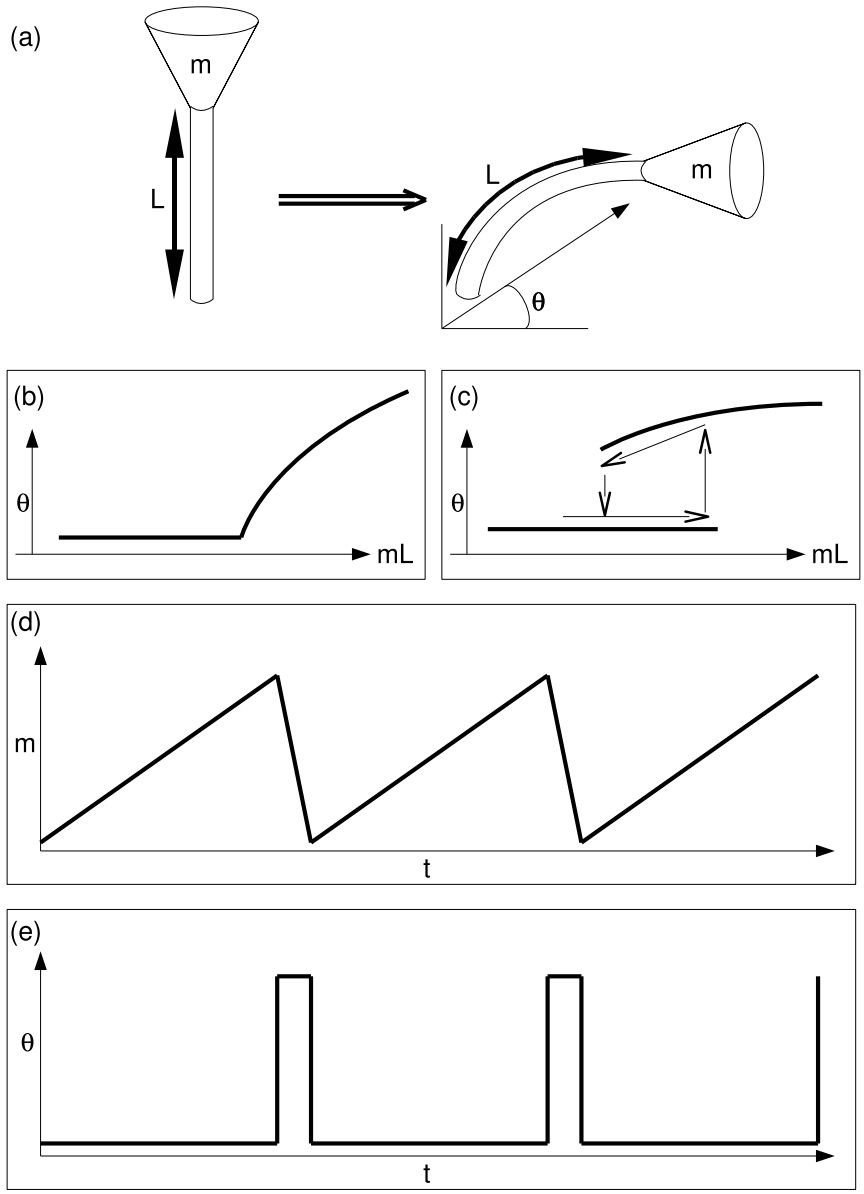

Figure 4.1: Relaxation oscillations. (a): A flexible tube of length L, with bending stiffness, is fitted with a funnel whose mass m can be varied by feeding water through the tube. At a critical mass the tube falls over and the funnel empties. (b): For certain ratios of fixed m to L the bending angle has a unique value. (c): At other ratios of $m : L$ the tube can be found in two stable states for a particular mL, with the response of the system showing hysteresis. (d) & (e): With a constant flow of water into the tube at these hysteretic values oscillations can be observed.

occurs. The mass builds until the critical value is reached, at which point the tube collapses, quickly releasing the water so that the tube returns to its upright state (Subfig. (d) & (e)). Here a bifurcation to periodic motion is observed, depending on the parameter related to the flow rate of water into the tube.

The models describing systems outlined subsequently usually treat each oscillator as being identical but in real systems this is not the case, with cells having some mismatch in their construction. This, as well as other sources of imperfection such as noise, is extremely difficult to model mathematically, and the results can often prove to be highly sensitive to the form that the imperfections take.

To show that such ideas are feasible in the real world, it can prove invaluable to use physical oscillators. Electronic oscillators are ideal for this task due to the high degree of control over the parameters of the system and the large amounts of high quality data that can be obtained. Electronic oscillators have been used to study nonlinear phenomena in real physical systems and such a system is described here.

In the physical systems used here, the imperfections are real, unlike the assumptions made in the theory, and the results can be relied upon much more to verify the mathematical results. As well as being able to attain a high degree of control over the parameters of the system, it is possible to measure the response to a very high accuracy. Also, any external interference which could affect the observed dynamics can be kept to a minimum and random noise is typically lower than in other physical systems. In addition, large amounts of data can be obtained from such systems in a relatively short space of time, making them perfect for testing time-series analysis techniques and investigating many of the concepts and theoretical predictions regarding chaotic systems.

4.2 Experimental System

For the experimental studies carried out in this research, a system of coupled nonlinear electronic oscillators was used. The individual oscillator units, shown schematically in Figure 4.2, are based on a modification of the van der Pol oscillator circuit [vdP27]. The essence of the circuit is an LCR loop in parallel to a nonlinear element, P, and various components which can be used as control parameters. The nonlinear element, consisting of radio valves in the original van der Pol system, has been replaced by a loop of twelve semiconductor diodes, based on the scheme of Shinriki *et al.* [SYM81] and modified by Robin Jones [HBC$^+$91]. Details of the experimental set-up can be found in the Ph.D. thesis of Healey [Hea91], along with a detailed study into the dynamics of the single oscillator system. The modified van der Pol electronic oscillator was used in the above study to demonstrate the Shil'nikov route to chaos in an experimental system [HBC$^+$91]. This set-up has also been used in several other experiments, notably work on the effect of noise on pitchfork and Hopf bifurcations by Juel *et al.* [JDM97] and on imperfect homoclinic bifurcations by Glendinning *et al.* [GAM01]. A further alteration to the original circuit has been the replacement of the LCR loop with a solid state equivalent to remove the effects of heating and external noise acting on the inductance coil. The present circuit was used to study pitchfork and Hopf bifurcations in systems of coupled oscillators in a Ph.D. thesis by Kerr-Delworth [KD99].

All components are kept fixed except for the resistance $R1$, which is connected across the nonlinear element and is used as a control parameter in the experiment. The nonlinearity of the operational amplifier is negligible in the regimes studied, being an order of magnitude smaller than for the other elements, so is taken to be zero throughout. Data for the system's dynamics were obtained by measuring the potential difference between the points V and g in the circuit, which varied approximately between -4.5V and 4.5V. Measurements were recorded by feeding the signals to a 16-bit *National Instruments* data acquisition card and recorded

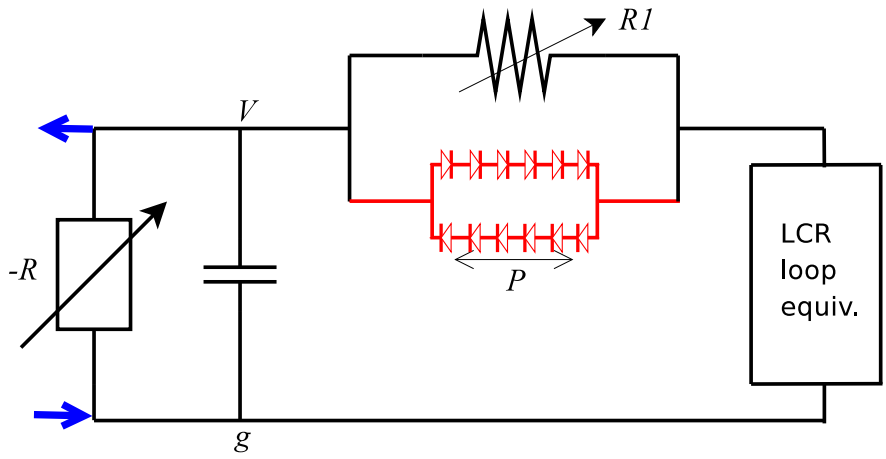

Figure 4.2: Circuit based on the van der Pol oscillator. Units are coupled via two unidirectional links from point V of one oscillator to g of the other and vice versa.

using real-time software at a high sampling rate.

Each oscillator has three degrees of freedom and is capable of exhibiting chaotic behaviour, as demonstrated in previous studies and described in the following sections. When n oscillators are coupled together the resulting $3n$ degrees of freedom systems can exhibit higher dimensional dynamics, such as various degrees of synchronisation and hyperchaos. The method of coupling used here follows the scheme of Kerr-Delworth [KD99], with the coupling links unidirectionally connecting the point V of one oscillator to g of another. The coupling links are constructed of operational amplifiers, whose high impedance allows the signal to be fed from one point in the coupled circuit to another without any feedback. The coupling strength can also be adjusted by a variable resistor, giving further control parameters in the coupled systems. For Chapters 5 and 6 a system composed of two oscillators unidirectionally coupled in a loop is used.

4.3 Theoretical Description

4.3.1 The Single Oscillator

The model for a single oscillator is given in Equation (4.1), which can be derived using Kirchhoff's laws:

$$\begin{aligned} \dot{x} &= \gamma\ [\ (y-x)/\beta + f(y-x) - \alpha_0 + \alpha x\ ], \\ \dot{y} &= -z - (y-x)/\beta - f(y-x), \\ \dot{z} &= y - \rho z. \end{aligned} \tag{4.1}$$

where x, y and z are dimensionless voltages and currents at various points in the circuit, β is a non-dimensionalisation of the variable parameter $R1$ and α of the negative resistance $-R$. The function $f(V)$ is the voltage response of the nonlinear element, P, which in its full form is the exponential: $f(V) = I_p(\mathrm{e}^{kV} - \mathrm{e}^{-kV})$, but can be well represented by a series expansion up to cubic order in V [Hea91]. The over-dot represents differentiation with respect to non-dimensional time, τ. All other symbols are dimensionless scaling constants, obtained by measurement of elements in the circuit, where $\gamma = 3.9$, $I_p = 1.87 \times 10^{-6}$ and $k = -3.9$.

In Equation (4.1), α_0 is used to model the small but inevitable imperfections in the system. This is assumed here to be a constant offset in the operational amplifier and represented by a simple linear term, $\alpha_0 = 7.2 \times 10^{-3}$. Although the imperfection here is tiny even a small bias can affect the global dynamics of nonlinear systems [GAM01]. In reality the imperfections will be more complex, but the approach taken here is sufficient to explain most of the features of the qualitative dynamics of the system.

The primary effect of this offset is to disconnect the two branches of the pitchfork bifurcation (as described in Section 1.2.2). This breaks the $\mathbb{Z}_2$ reflection symmetry of the subsequent oscillatory and chaotic dynamics of the system, offsetting

the various bifurcations of dynamical states so that they occur at different parameter values for each branch. This is an important effect when considering the coupling between two or more oscillators, as described in the following sections.

4.3.2 Coupling of Oscillators

The results in this thesis are from systems of coupled oscillators such as the one described at the end of Section 4.2. An oscillator, Oi, which experiences a coupled signal from a second oscillator, Oj, can be represented using the following set of equations:

$$\begin{aligned} \dot{x}_i &= \gamma\ [\ (y_i - x_i)/\beta_i + f(y_i - x_i) - \alpha_0 + \alpha_i(x_i - \sigma x_j)\ ], \\ \dot{y}_i &= -z_i - (y_i - x_i)/\beta_i - f(y_i - x_i), \\ \dot{z}_i &= y_i - \rho z_i. \end{aligned} \tag{4.2}$$

Oscillators Oi and Oj are denoted by the indices i and j, and this model is generic for any unit in a linear chain of any number of oscillators coupled unidirectionally. This model gives a good representation of the system for the range of parameters considered in Chapters 5 & 6, within the error in determining the scaling constants [KD99].

4.4 Coupled Cell Networks

A coupled cell network is a system of identical subsystems (or *cells*) connected together with identical coupling, where the direction of coupling is defined [GNS04]. One of the simplest coupled systems that can be modelled by Equation (4.2) above is a system of two oscillators coupled unidirectionally in a loop. This can be represented as the simple 2-cell network shown in Figure 4.3, where the arrows show the direction of coupling between cells. In this case the system can be represented by two sets of Equation (4.2), with the indices $[i, j]$ replaced by $[1, 2]$ and $[2, 1]$,

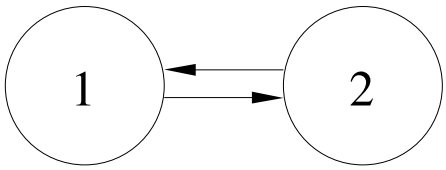

Figure 4.3: The 2-cell network representation of the system.

respectively.

The following sections of this thesis will deal primarily with high-dimensional dynamics in this simple configuration but in natural systems the cells can be coupled in many complex configurations. For example, different networks of neurons are coupled together in a myriad of ways to perform the different functions of the brain. Therefore it is important to understand the different phenomena that arise from coupling together autonomous oscillators of similar characteristics.

Small numbers of coupled oscillators can, depending on some parameter of the individual units and the strength of coupling, produce temporal rhythms and effects essential to many biological functions. The CPG for animal locomotion mentioned in Section 1.1.3 was able to reproduce all the known gaits of multi-legged animals from a network of $2n$ coupled oscillators, where n is the number of legs [GSBJ98]. Coupled oscillator systems can be used to model many other aspects of physiology, and the next section gives an example which uses a simple network to detect and amplify periodic signals at a specific frequency, using mechanisms believed to be present in animal auditory systems. This provides an ideal suitability test for the electronic systems used throughout this thesis.

4.5 Signal Detection Using Networks

Systems that can detect and amplify signals at specific frequencies are commonplace in the natural world; notably in the visual and auditory systems of animals. Scientists and engineers frequently look to biology for inspiration, and signal detection is one area where nature has excelled in producing systems with superior

characteristics over man-made devices [Wat94]. Animal auditory systems have excellent filtering characteristics, such as a wide range of amplitudes over which they can detect (their *dynamic range*) [Kin82]. Nonlinear compression of the input signals (the *dynamic compression*) is believed to be responsible for the large dynamic range in these systems. Several models exist which employ active elements in the auditory apparatus to achieve this [GP48; EOC+00; HER05], where cells are tuned close to a Hopf bifurcation. Cells with properties similar to van der Pol oscillators are believed to be responsible for amplification in some of these cases [SKG+06]. Physiological evidence exists for this *active audition* due to Hopf bifurcations for a range of animals and insect auditory systems [MH99; JÖ1; OEM01; GR03]. Models have also been proposed which make use of coupling between limit cycles to produce significant amplification in insect hearing [KS03; SVK04].

A system of coupled oscillators using this property to detect small periodic signals is presented here. The experimental system utilises the electronic oscillators introduced in Section 4.2 as the "cells" of the network, demonstrating their utility for testing such theoretical ideas.

4.5.1 The 3-Cell Feed-Forward Network

The network under investigation follows the configuration shown in Figure 4.4, with sinusoidal forcing of amplitude ε and frequency ω_F into a network of three cells coupled in a feed-forward manner. Preliminary numerical results by Professors Martin Golubitsky[1] and Don Aronson have indicated that, with each cell set close to the Hopf bifurcation, significant amplification occurs in cell 3 when the system is forced at $\omega_F = \omega_H$, the natural frequency at Hopf bifurcation.

[1]By private communication.

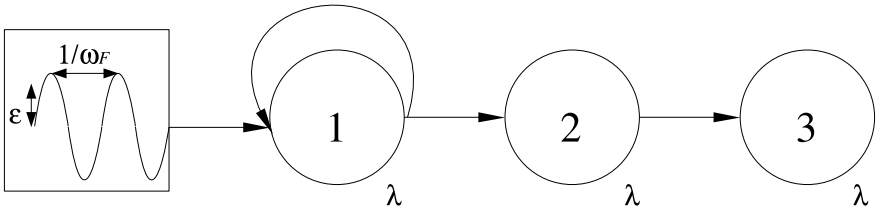

Figure 4.4: A schematic of the 3-cell feed-forward network with periodic forcing. Three identical oscillators are coupled unidirectionally. The bifurcation parameter λ is varied identically in each cell to tune the system on the Hopf bifurcation. A small forcing signal with amplitude ε and frequency ω_F is put into cell-1, triggering oscillation in the system when $\omega_F \approx \omega_H$, the natural frequency of the system at Hopf bifurcation.

This system can be represented by:

$$\begin{aligned} \dot{x}_1 &= f(x_1, x_1 + \varepsilon \cos(\omega_F t), \lambda), \\ \dot{x}_2 &= f(x_2, x_1, \lambda), \\ \dot{x}_3 &= f(x_3, x_2, \lambda); \end{aligned} \tag{4.3}$$

where λ is a bifurcation parameter, held identical in each cell and equal to zero at the Hopf bifurcation point. This is based on a similar system without the forcing term, studied analytically and numerically by Golubitsky *et al.* [GNS04]. A Hopf bifurcation was found to produce stable periodic solutions in cells 2 and 3, while cell 1 remained in equilibrium. In a surprising result, the amplitude growth in cell 3 was found to be $\lambda^{\frac{1}{6}}$ rather than the $\lambda^{\frac{1}{2}}$ expected for the growth after a Hopf bifurcation; suggesting resonant forcing of the third cell was important rather than simply a Hopf bifurcation phenomenon.

The idea here is to use such a network to selectively amplify an input signal at a specific frequency: the Hopf frequency of the system ω_H. The current investigation focuses on the configuration shown in Figure 4.4, with λ set close to the λ_c, the Hopf bifurcation point. The system is forced by a small harmonic input of amplitude ε and frequency ω_F.

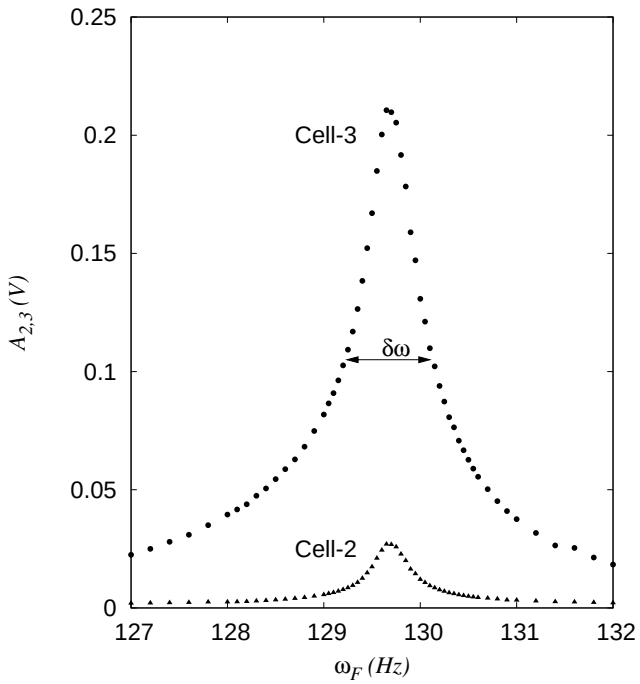

Figure 4.5: Response of the 3-cell feed-forward network, on variation of the drive frequency ω. The responses of both cells 2 and 3 are shown. A sharp peak can be seen in Cell 3 when the forcing frequency ω_F is around $\omega_F = \omega_H$, the natural frequency of the system at the Hopf bifurcation.

4.5.2 Experimental Results

The oscillators were set up in a configuration equivalent to Equation (4.3), with the fed-forward signal having a coupling attenuation of $\sigma = 0.0909$, and carefully balanced to ensure as close agreement to theory as possible. A water cooled copper heat-sink and a thermally insulating enclosure was used to stabilise the circuit at the Hopf bifurcation point. This is needed as systems are very sensitive to noise close to bifurcation points and thermal fluctuations affect the nonlinear elements, causing the Hopf bifurcation to "drift" in λ [JDM97].

A sharp response was found in cell 3 when forcing near ω_H, the natural frequency of the system at the Hopf bifurcation. States of the system settled to a stable non-oscillating equilibrium when forced at other nearby frequencies.

The amplitude response, A_3, of the third cell is shown in Figure 4.5 for a forcing amplitude of $\varepsilon \sim 5 \times 10^{-4} V$. A sharp response can be seen around $\omega_F = \omega_H$,

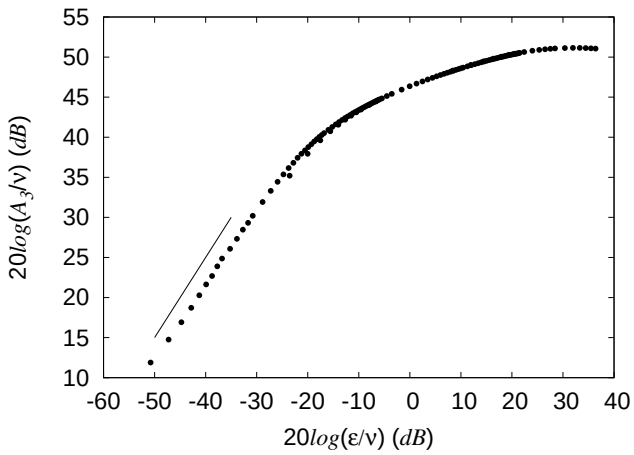

Figure 4.6: Amplitude response of the network. The amplitude found in cell-3 relative to the noise floor is shown on a log scale, plotted as a function of the input signal-noise ratio. The results demonstrate the compression of input amplitudes and the wide dynamic range of the system.

decaying quickly as $|\omega_F - \omega_H|$ increases. The bandwidth of the frequency–amplitude curve, measured as the full width at half maximum (FWHM) frequency spread, is seen to be $\delta\omega \approx 1\%$ of the central frequency. This corresponds to a *quality factor* $Q \approx 100$, demonstrating that the system has a narrow passband.

The system is found to exhibit much greater amplification for lower forcing amplitudes; demonstrating a strongly nonlinear amplitude response. An amplitude response curve over a range of ε at fixed $\omega_F \approx \omega_H$ is shown in Figure 4.6. Values of the amplitude of the third cell A_3 for a range of forcing amplitudes ε are given in dB, relative to the noise level ν. The system can be seen to have a wide dynamic range, measured to be $> 80dB$, as well as a large dynamic compression due to the nonlinear response of the system – thus comparing well to biological systems.

Finally, the amplitude growth through cells 2 and 3 was investigated to compare experiment to theory and confirm the suitability of this prototype system. Specifically the $\lambda^{\frac{1}{6}}$ growth of the third cell was sought, which was such a striking feature of the original unforced system. The ratio of the amplitude responses of cells 2 and 3 is found by plotting the amplification of A_2 and A_3 (Γ_2 and Γ_3, in

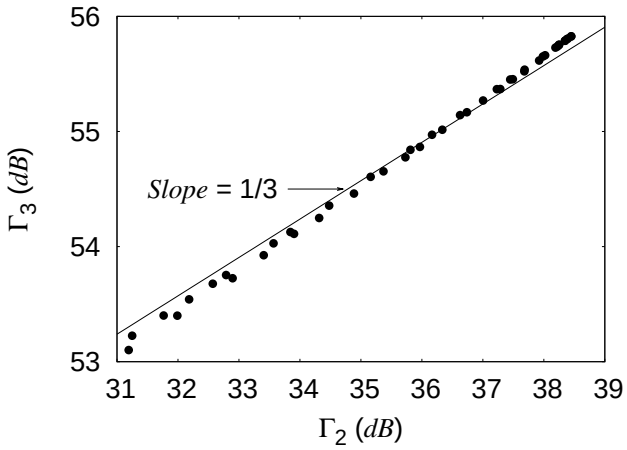

Figure 4.7: Relationship between amplitudes in cells 2 and 3. The amplification found in cells 2 and 3 (Γ_1 and Γ_3, respectively) are shown, in dB. The line indicates the predicted gradient of 1/3.

dB) for data across a range of ω_F close to the peak, and compared to the theoretical ratio of the exponents. This method involving the ratios of amplitudes was used because the bifurcation parameter λ is held constant at the Hopf bifurcation point λ_c. The resulting plot of the amplification in cells 2 and 3 (Γ_2 and Γ_3, in dB) for data across a range of ω_F close to the peak response is shown in Figure 4.7. A line with the predicted gradient of $m = 1/3$ dB/dB is also plotted for comparison. A linear relationship can be seen, with a least squares fit gradient of 0.369 ± 0.002, which is close to the expected value of 1/3 predicted by the theory for the unforced system [GNS04].

These results demonstrate effectively the usefulness of this type of electronic oscillator for experimentally investigating theoretical ideas about nonlinear coupled networks.

4.6 Spatial Networks

Larger arrays of coupled cells can resemble a continuous medium, and synchronisation effects can give rise to the formation of spatial patterns or some unified motion of the whole system, depending on the type and level of synchronisation (see Section 1.2.11). Conversely, the partial differential equations describing continuous systems with spatial as well as temporal extent have an infinite number of degrees of freedom and are often unwieldy and hard to compute numerically. It is often convenient to decompose these systems into a series of low dimensional units coupled together to create a spatial network. For example, models of an oscillating medium can be reduced to a system of coupled oscillating cells, with the coupling strength dependent on the distance between neighbours [Kur84]. Therefore, results from studies on simple networks of oscillators could prove very useful in helping to understand phenomena found in large complex and spatially continuous systems.

4.7 Bifurcation Structure in the Oscillators

4.7.1 Bifurcations of the Single Oscillator

The following is a qualitative outline of the various bifurcations and dynamics found in a single isolated oscillator, as described by Equation (4.1). A numerically generated one-parameter bifurcation diagram is presented in Figure 4.8, with $\alpha = 0.325$ and $3.0 < \beta < 4.4$.

On steadily increasing β, the system exhibits a progressively more complicated

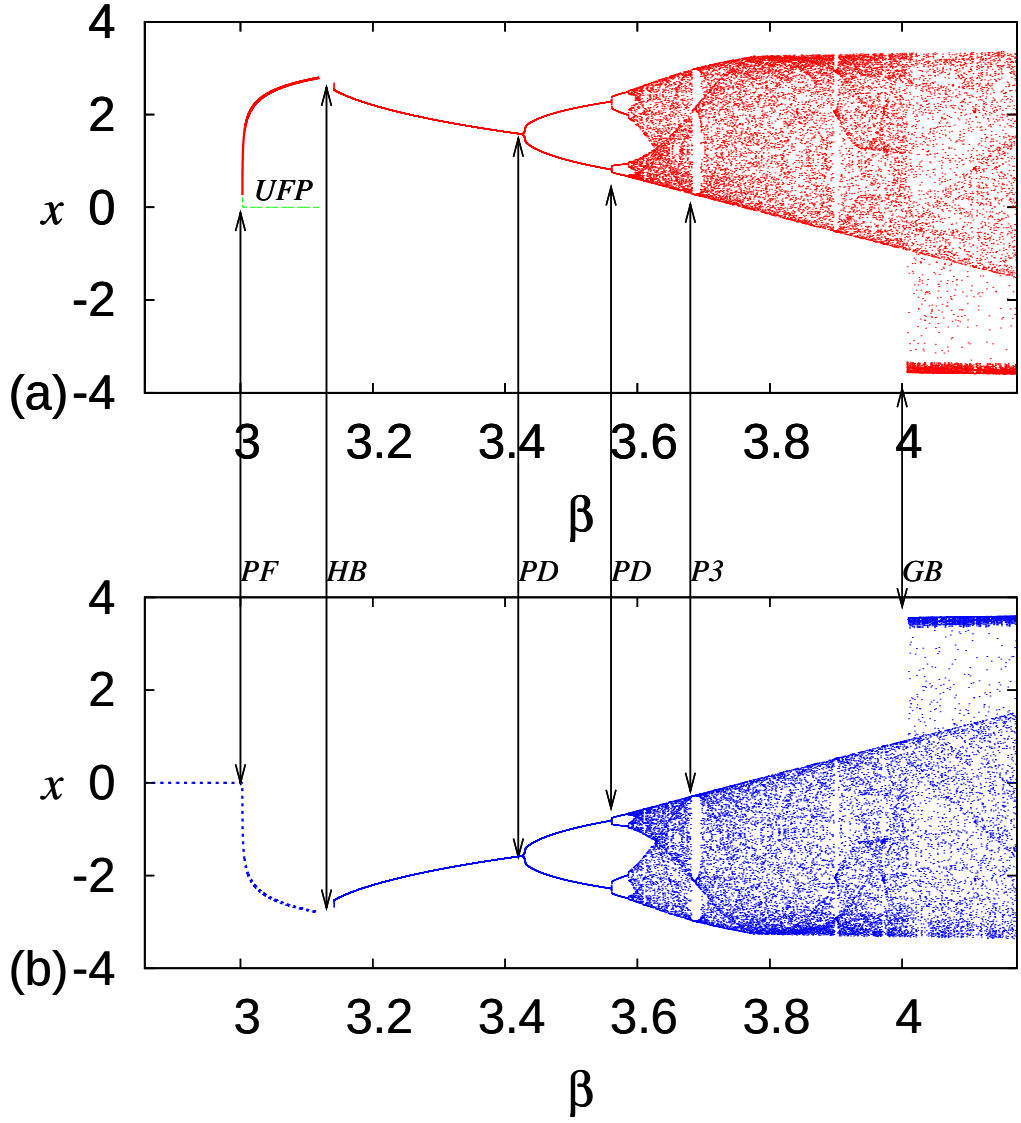

Figure 4.8: Numerical bifurcation diagrams for the single oscillator. In (b) PF marks the primary pitchfork bifurcation, HB the Hopf bifurcation and PD the first two period doubling bifurcations. P3 is a period-3 window and at GB the gluing bifurcation occurs.

response, beginning with a pitchfork bifurcation at $\beta \approx 3$ from a stable equilibrium at the phase space origin to two attracting fixed points. Both branches have growth laws close to $x \sim \pm\sqrt{\beta^*}$, where $\beta^* = \beta - \beta_{PF}$, the distance from the pitchfork bifurcation. These are both shown in Figure 4.8, with the disconnected branch in (a) and the continuous in (b). The disconnection is caused by the small imperfections in the system, modelled by the term α_0 in Equation (4.1). The attracting and unstable fixed points shown were generated from the equations of motion (4.1) using the package AUTO; a freely available set of tools for continuation of the solutions of dynamical systems and their bifurcations [Doe81].

Both branches of the system's response then undergo Hopf bifurcation at similar values of β (HB in Fig. 4.8), leading to stable periodic motion. The solutions were from here on produced by integrating the equations of motion using the Runge-Kutta routines mentioned in Section 2.1.1 and taking a one-dimensional projection of a Poincaré section of the flow in phase space at each value of β.

These periodic solutions then experience period doubling bifurcations, which occur at geometrically decreasing values of $\delta(\beta)$, the distance between successive bifurcations. This period doubling cascade leads to chaos in the system. The route to chaos in the single modified van der Pol oscillator was studied by Healey *et al.* [HBC$^+$91], with an almost identical set-up. There it was found that the Shil'nikov mechanism was responsible for the period doubling cascade to chaos in the system. From this it is known that the chaotic attractors of such a system are composed of an ensemble of infinitely many unstable periodic orbits (UPOs).

At higher values of β there is a point where the two states originating on different branches of the pitchfork bifurcation combine to form one large attractor in a *gluing bifurcation*. An analysis of the gluing bifurcation in the non-chaotic, planar case was carried out by Glendinning *et al.*, based on a study of this system [GAM01]. A gluing bifurcation occurs when two orbits become connected to form a single "glued" orbit. The orbits involved in the gluing bifurcation are shown in

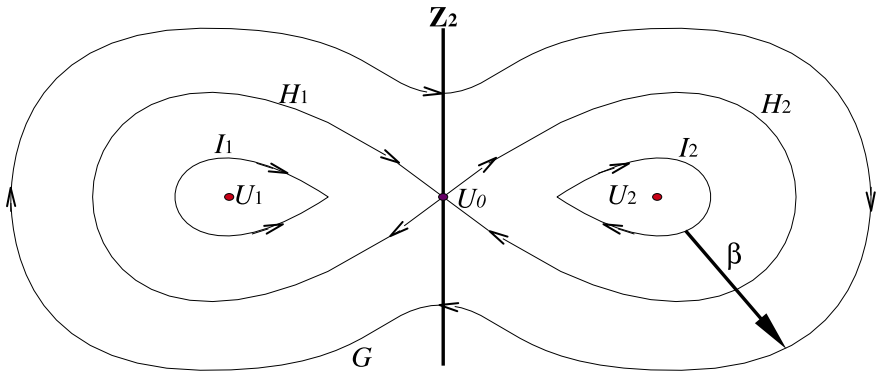

Figure 4.9: Homoclinic *gluing bifurcation*. Two orbits, I_1 and I_2, rotating about unstable fixed points, U_1 and U_2, grow on variation of a parameter β, until they reach the homoclinic orbits, H_1 and H_2. After this point one glued orbit, G, exists.

Figure 4.9. The *homoclinic orbits* H_1 and H_2 demark the separatrix between the glued orbit G and two orbits I_1 and I_2, which rotate about their respective foci U_1 and U_2, the unstable fixed point (UFP) remnants of Hopf bifurcations. This idealised situation requires $\mathbb{Z}_2$ symmetry (represented by the line labelled $\mathbf{Z}_2$ in Fig. 4.9). The UFPs U_1 and U_2 both originate from the hyperbolic fixed-point U_0 at a pitchfork bifurcation and suffer similarly from imperfections in the real system, disconnecting the homoclinic orbits.

In the chaotic case the situation is similar but the gluing manifests itself as a boundary crisis. The attractor steadily increases in size until its basin of attraction collides with that of its counterpart on the other side of the line of broken symmetry, resulting in the gluing bifurcation. After this point trajectories switch intermittently between the two "lobes" of the attractor.

4.7.2 A Coupled Pair of Oscillators

The unidirectional coupling from one oscillator (O1) to another (O2) has an effect equivalent to adding a static or dynamic perturbation to the α_0 term in the equations of motion (4.1), proportional to the state of O1. The bifurcations of O2 are therefore shifted depending on the magnitude of x_1 in O1. The effect of

feeding a constant voltage input from O1 to O2 is shown for experimental data in Figure 4.10 (a).

This behaviour for the two oscillators coupled in a loop is shown schematically in Figure 4.10 (b). In this case the effect is mutual and the resulting state of the combined system is more complicated. At higher parameter values, where $x_{1,2}$ have large magnitudes, the disconnected branch of the pitchfork bifurcation is shifted to values of $\beta_{1,2}$ where the continuous branch has already bifurcated to chaos. The dynamical states of the system can have two distinct configurations; one in which x_1 and x_2 are of opposite sign and the other where they take similar values on average. This can be explained by considering the mutual effect that each oscillator has on the other. When states of Oscillator 2 (O2) are on the continuous branch ("**C**" in Fig. 4.10), in the negative voltage regime, the coupling feeds a small negative voltage offset into Oscillator 1 (O1). This negative offset has the effect of making the negative branch of the pitchfork in O1 discontinuous and shifted to higher values of β_1. States on O1 are therefore forced onto the continuous branch, where they take the opposite sign to those in O2.

In the other case, when the states of O2 exist on the discontinuous branch ("**D**") in the $x_2 < 0$ regime, states on O1 are likewise forced onto the discontinuous branch at $x_1 < 0$. This can be understood intuitively by considering the effect of switching one of the oscillators to the opposing solution. If O2 were to be forced onto the continuous $x_2 > 0$ branch, the σx_2 attenuated offset imposed on O1 would cause the bifurcations to shift; reconnecting the $x_1 < 0$ branch and reverting the situation to the previous scenario. Therefore these are the only two stable configurations of the states in this parameter region. Henceforth, states with both oscillators on the continuous branch in opposing voltage regimes will be known as **C** and those together on the offset, disconnected branch as **D** states.

The effect of this on the observable states of the system follows the scheme shown in Figure 4.10 (c). On increasing the parameter ($\beta_1 = \beta_2 \equiv \beta$), the system bifurcates to chaos following a Hopf bifurcation from a nonzero fixed-point on

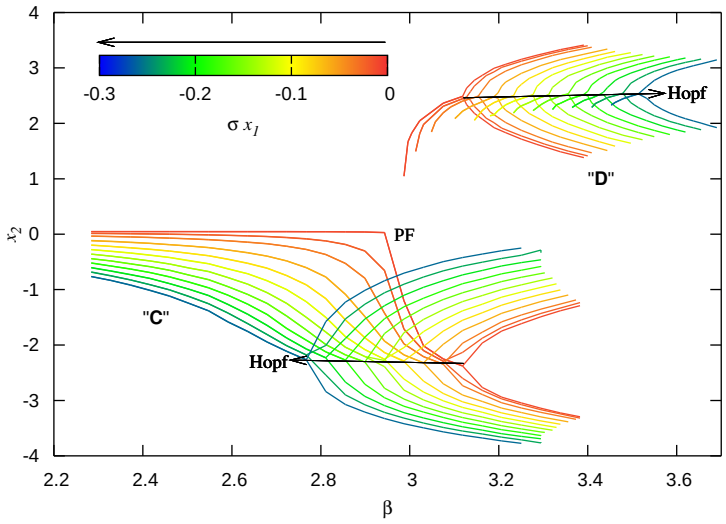

(a)

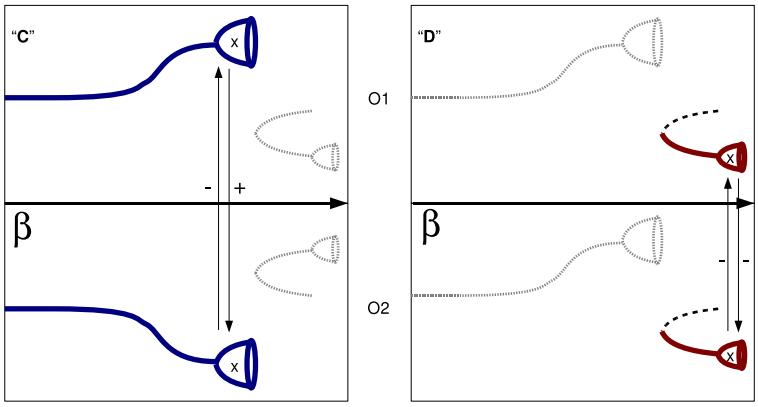

(b)

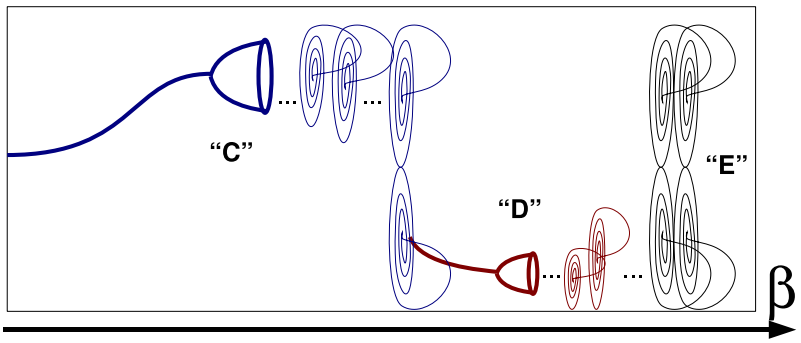

(c)

Figure 4.10: Dislocation of bifurcations due to coupling. An experimental study is presented in (a) of the dislocation of the continuous "**C**" and discontinuous "**D**" branches of the pitchfork bifurcation and consequent offsetting of the Hopf bifurcations of the response of one oscillator x_2 as a result of different levels of constant input from a second oscillator, σx_1. A schematic representation of the dislocation of the pitchfork and Hopf bifurcations of each oscillator by the other at an instant is given in (b). A representation of the resulting bifurcations in the coupled system on variation of β is shown in (c), wherein "**E**" represents the *glued* state.

the continuous branch (**C**) of the primary bifurcation. At higher values of β the degenerate attractors in the negative and positive voltage regimes combine to form one large "glued" state. On further increasing β the disconnected branch appears and states of the system come into contact with it. The glued **C** state is now a nonattracting set and trajectories fall onto **D** states of the disconnected branch, where solutions are once again in equilibrium. These then proceed to bifurcate to oscillating and chaotic states. The chaotic attractors of **D** steadily increase in size on increasing β until their boundaries collide with that of the nonattracting set **C** and the two merge.

4.8 Summary

In this chapter, systems of nonlinear oscillators coupled in various configurations were described. The usefulness of electronic oscillators for experimental investigations of these networks was also demonstrated. A modified van der Pol electronic oscillator has been described which develops chaotic dynamics through a sequence of bifurcations. A system of two of these circuits (or "cells") coupled unidirectionally in a loop has been introduced, along with the bifurcations which are found to appear herein.

The system is found to develop hyperchaos in certain of these parameter regimes, as well as exhibit high dimensional effects such as unstable dimension variability (UDV). To gain an understanding of the phenomena found in this system, the methods described in Chapters 2 and 3 have been applied, including analysis on real time-series data and numerical calculations. A detailed study of the dynamics found in these various regimes is described in the following chapters. In Chapter 5 the case of UDV is studied and the origin of hyperchaos in the system is investigated in Chapter 6.

Chapter 5

High Dimensional Dynamics and Unstable Dimension Variability

In this chapter a study of the phenomena found in the system of two oscillators coupled in the loop configuration is described. This investigation was carried out at parameter values where complex dynamics were encountered. Particularly, a case of unstable dimension variability (UDV) found in the system is investigated. This type of high-dimensional dynamics is important both when trying to determine the reliability of models of the system, as well as for gaining a greater understanding of intermittent behaviour found in higher dimensional systems.

As explained in Section 1.2.2 the two branches of the pitchfork bifurcation are dislocated by the introduction of a small imperfection or offset (Fig. 1.5), such as that generated by the attenuated output from another oscillator. In Section 4.7.2 it was shown how the feedback effect between the two coupled oscillators leads to two distinctly different states coexisting at the same values of β. These are labelled "**C**" for states originating on the continuous branch and "**D**" for those on the discontinuous branch, as introduced in Section 4.7.2 and shown in Figure 4.10 (c). As noted previously, the **C** sets on one cell generally do not coexist with the **D** sets on the other, with both cells always exhibiting similar dynamics to each other. The dynamics of the system therefore behave in unison, with attractors

of the combined system existing on either **C** or **D**. Dynamical states of **C** are encountered at lower values of β than those of **D**, these being offset to higher values.

For the purposes of this study all of the system parameters were kept constant except for β_1. The presented results were obtained by recording values of x_1 over a range of β_1. However, the results are found to be qualitatively similar even if a different parameter is changed or a different variable used for the measurements. The attractors of the system were reconstructed using the time-delay embedding technique of Takens outlined in Section 2.2.1, with the embedding dimension determined using the false neighbours method [KBA92].

5.1 Experimental Lyapunov Exponents

The bifurcation diagram of Figure 5.1 (a) shows the evolution of attractors of the system as a function of the parameter β_1. At first, up to $\beta_1 \approx 3.48$, states exist on the large ("glued") attractor on the continuous branch, **C**. At higher parameter values the discontinuous **D** branch exists and states are measured on its attractors, the **C** branch now being unstable (a saddle).

The associated evolution of the three largest Lyapunov exponents $(\lambda_1, \lambda_2, \lambda_3)$ over the same range of β_1 was determined using the method of Wolf *et al.* [WSSV85] with trajectories containing 2×10^5 points. These Lyapunov exponents are shown in Figure 5.1 (b). The errors shown are estimates of the robustness of the method, obtained by varying various parameters of the calculation and observing the resulting shift in the computed values.

In the studied parameter regime, where the attractors on **C** are in the "glued" state and flip intermittently between the two lobes, the attractor is found to have two positive Lyapunov exponents (i.e. it is 2D unstable). The structure of this large hyperchaotic attractor and the origin of the second Lyapunov exponent are studied in detail in Chapter 6, this being central to understanding the dynamics of

the system. After $\beta_1 \approx 3.48$ the hyperchaotic attractor loses stability to become a saddle, and states fall onto the smaller non-chaotic set on **D** with no positive Lyapunov exponents at these parameter values. In similar domains of β_1 an almost symmetrical disconnected set can also be found at negative values of x_1. For parameter values above $\beta_1 \approx 3.56$, a limit cycle attractor bifurcates to chaos, with one positive Lyapunov exponent (i.e. it is 1D unstable). The attractor then steadily grows in size until $\beta_1 \approx 3.72$, at which point the 1D unstable **D** attractor experiences an interior crisis with the 2D unstable (hyperchaotic) **C** saddle and the two merge [1]. The Lyapunov exponents above $\beta_1 \approx 3.72$ reveal that this combined attractor is hyperchaotic, with two of them being positive over long time averages.

At values of β_1 just above this transition, trajectories move intermittently between the large set from **C** and the two small sets from **D**. In Figure 5.2 a time-series in which trajectories spend appreciable time in each set is shown. This time-series is typical of the type of behaviour seen when trajectories are split evenly between the different subsets of the attractor. However, for increasing β_1 trajectories become progressively smooth, with attractors being dominated by the large sub-set, and have no clear intermittent structure.

Attractors at the merger of **C** and **D** are therefore a combination of the two, with fluctuations of trajectories between them resulting in the local dynamics inheriting characteristics of both. As the **D** sets contain periodic orbits with 1D unstable manifolds and the **C** set periodic orbits with 2D unstable manifolds, a trajectory in the post-crisis attractor will visit the vicinity of periodic orbits with a different number of expanding directions. Therefore the attractor shortly after the crisis should experience UDV.

[1] Due to the imperfect symmetry of the system the two small attractors experience the crisis at slightly different values of β_1.

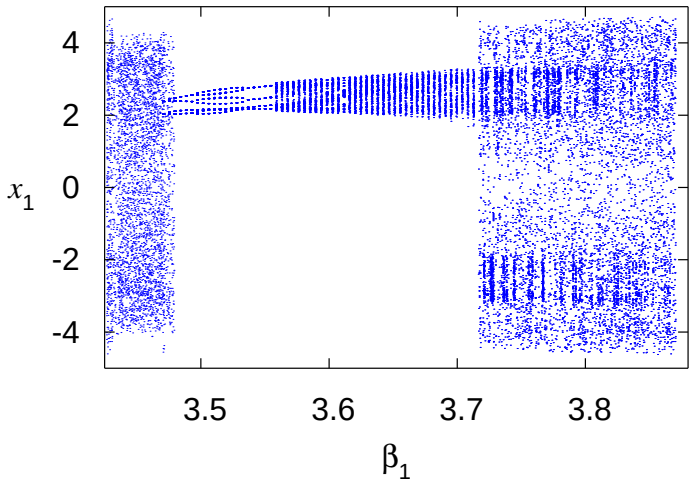

(a)

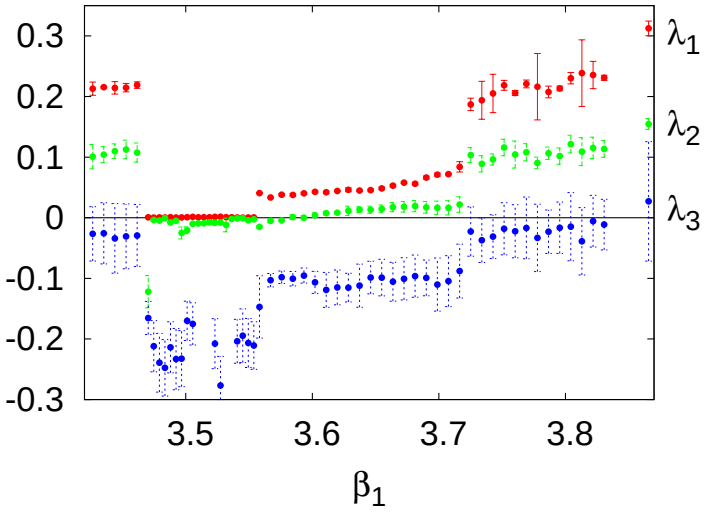

(b)

Figure 5.1: Experimental bifurcation diagram (a) for the system as a function of the dimensionless parameter β_1. For $\beta_1 < 3.72$ there is an almost-symmetric attractor which is not shown. The value x_1 is the first non-dimensional embedded coordinate, which is exactly equal in magnitude to the measured voltage response of the system. Associated evolution of the three largest Lyapunov exponents (b) of the system of coupled oscillators for varying β_1.

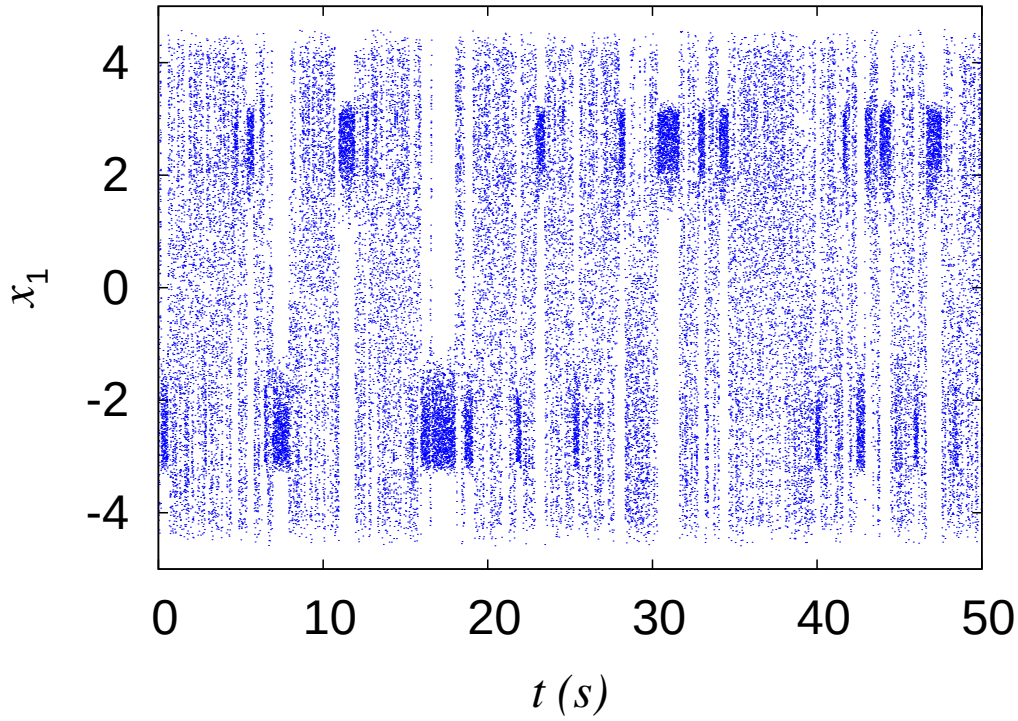

Figure 5.2: Time-series in a region of parameter space showing clear intermittency between the three sets.

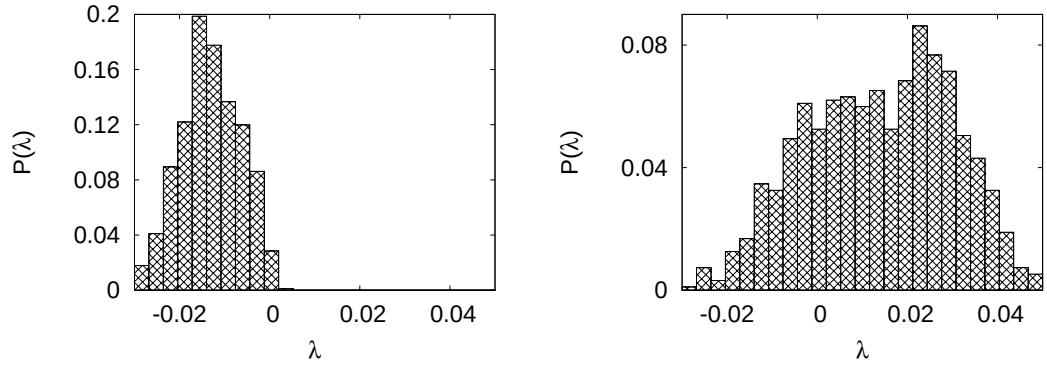

(a) Pre-crisis attractor (b) Post-crisis attractor

Figure 5.3: Histograms of numerically generated short-time Lyapunov exponents. The second and third exponents have been summed to give the peaks shown. The spread of values seen in (b) across positive and negative values is an indication of UDV.

5.2 Numerical Confirmation of UDV

5.2.1 Short Time Lyapunov exponents

The equations of motion of the system were integrated using a Runge-Kutta algorithm in order to numerically compute the Lyapunov exponents. These were obtained using the method of Benettin *et al.* [BGGS80] and their evolution is very similar to that obtained from the experimental data, confirming that the model and the real system have similar characteristics. Figure 5.3 shows the histogram of the sum of the second and third STLEs before and after the crisis where **C** and **D** merge, using a time of a twenty periods of oscillation for the calculations.

This sum will take either negative or positive values depending on whether locally there are one or two expanding directions respectively, as one of these exponents will correspond to the neutral direction of the flow and have a value close to zero. Before the crisis the distribution of this STLE is restricted to negative values (Fig. 5.3(a)), while shortly after the crisis it includes both positive and negative values (Fig. 5.3(b)). As described earlier this indicates that trajectories are visiting regions in the attractor where the number of expanding directions is different.

5.2.2 Separating Invariant Sets

The characteristics of the attractor shortly after the above crisis were studied in more detail by using this model and the PIM-simplex method [MD99]. The latter allowed for the decomposition of the attractor into unstable invariant sets and to gain further insight into the origins of UDV in the system. The three invariant sets obtained in this way for parameter values shortly after the crisis are shown in Figure 5.4. The points marked with blue "$*$" marks correspond roughly to the pre-crisis attractors, while the larger set indicated with red "$+$" marks is incorporated into the attractor at the point of the crisis. Long trajectories were obtained into each of these non-attracting sets and the corresponding Lyapunov exponents were calculated using the method of Benettin *et al.* [BGGS80]. The small sets were found to only contain one positive Lyapunov exponent and the large set to have two. As all sets are part of the attractor after the crisis, this implies variations in the number of locally expanding directions for points belonging to a typical trajectory.

5.3 Measuring UDV

5.3.1 Experimental Results

The method described in Chapter 3 was used to determine the number of expanding directions locally throughout the attractor. The method was applied to time-series data from the system at various values of β_1. The reconstructed attractors consisted of 2×10^5 points embedded in four dimensions. Around each trajectory point x the hyper-spherical region $B_\epsilon(\mathsf{x})$ was defined, of radius ϵ, to be as small as possible to reduce the effects of curvature, while ensuring that the number of contained points was large enough to obtain good statistics. The optimal size was found to be $\sim 2\%$ of the radius of the attractor. Each hyper-spherical region was found to contain from ~ 100 to ~ 2500 points, which were

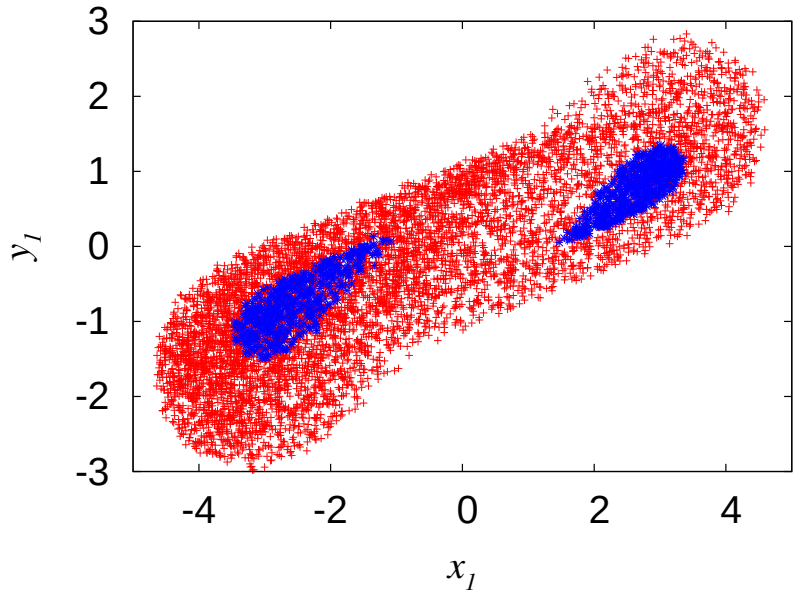

Figure 5.4: Two-dimensional projection of periodically sampled orbits of the numerically separated invariant regions. Results were obtained at a parameter value where trajectories spend approximately equal times on average in each subset. The small sets were found to have one positive Lyapunov exponent and the large set to have two.

used to determine $\mu(d)$ as described in Chapter 3. Averaging was performed over the values of $\mu(d)$ for 20 consecutive points on a trajectory to obtain $\bar{\mu}$ and to reduce statistical broadening of the peaks. Histograms at various values of β_1, showing the distributions of $\bar{\mu}$ over the attractor, both before and after the crisis are presented in Figure 5.5. It can be seen clearly that, just before the crisis, the histogram shows only one peak (Fig. 5.5(a)), with its maximum just above the characteristic value for two dimensions given in Table 3.1 on page 71. This shows that the reconstructed attractor consists of points which locally lie on an approximately two-dimensional surface everywhere, indicating only one expanding direction to the flow. The small shift of the peak to a value higher than that predicted is believed to be due to the presence of noise and the fractal structure of the attractor along the stable directions, as well as to curvature effects. Noise will cause the contracting directions to be broadened slightly (Fig. 3.1(b), page 69), separating otherwise nearby points by a small distance and increasing the

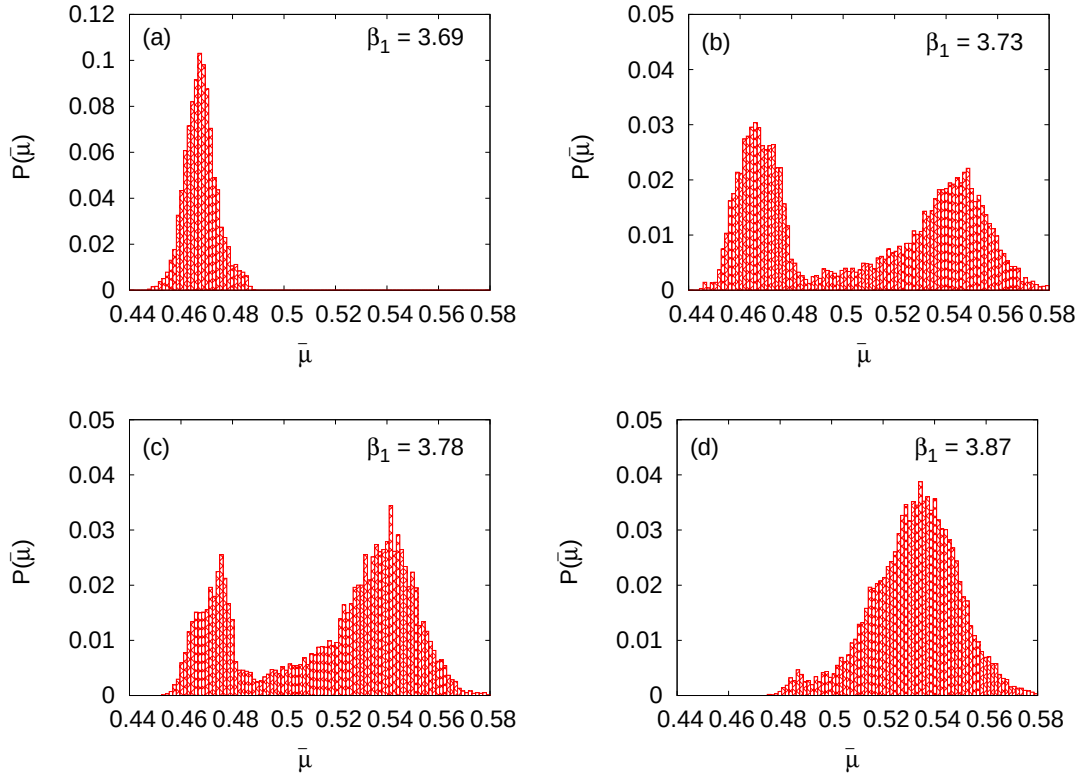

Figure 5.5: Distributions of local mean distances, $\bar{\mu}$, between points in the embedded attractor. Before the crisis the values of $\bar{\mu}$ are located around one peak close to the value corresponding to a two dimensional distribution of points, (a). After the crisis, and for nearby values of β_1, the distribution shows two peaks around the values corresponding to two and three dimensional distributions of points, (b) and (c). For larger values of β_1 the distribution of points is mainly three dimensional, (d).

value of $\bar{\mu}$. This hypothesis was confirmed by performing the method on numerically generated time-series of the same system, based on the model described in Section 4.3.2, both with and without the addition of a small amount of Gaussian noise. It was found that the addition of noise shifted the peak to the right, by an amount related to the magnitude of the noise. However, in the absence of additive noise, the peaks were observed to be slightly lower than the theoretical values. This is probably due to the effects of trajectories passing close to the edge of the attractor, as the neighbourhoods of points in this region will be partially empty, resulting in a lower value of the mean distance.

After the crisis, and for parameter values where trajectories were seen to visit the three different sets of the combined attractor, the histograms obtained show two distinct peaks (Figures 5.5(b) and 5.5(c)). The first recorded peak is at similar values to those recorded before the transition but the second peak has its maximum at a value close to that expected for a three dimensional distribution of points, indicative of two expanding directions. Thus the trajectory under investigation here is observed to visit regions of phase space where there are both one and two local unstable directions.

The area below each peak gives an idea of the proportion of time the trajectories spend around the one-dimensional and two-dimensional unstable regions. The obstruction to shadowing due to UDV is strongest when each region is visited for a substantial proportion of time as this results in one STLE having large variance and a mean value close to zero [SGY97]. According to Figure 5.5 this occurs for β_1 between 3.73 and 3.78. For larger values of β_1 trajectories mainly visit regions with two expanding directions and we can expect fewer changes in the local unstable dimension and longer periods of time where the dynamics can be considered to be nearly hyperbolic.

5.3.2 Separating Invariant Sets

The information gained from the application of the method can also be used to separate the embedded attractor into its regions of different unstable dimension, as shown in Figure 5.6 for $\beta_1 = 3.78$. Points denoted by blue "$*$" marks correspond to trajectory points where locally there is one expanding direction and those marked with red "+" marks to points with a two dimensional unstable tangent space. Qualitative similarities can be seen between Figure 5.6 and the sets obtained by means of the PIM-simplex method in Figure 5.4, even though Figure 5.6 is for a four dimensional embedding in a different projection to the six dimensional simulation of Figure 5.4. While the results in Section 5.2.2 relied on numerical computations and the availability of a model of the physical system,

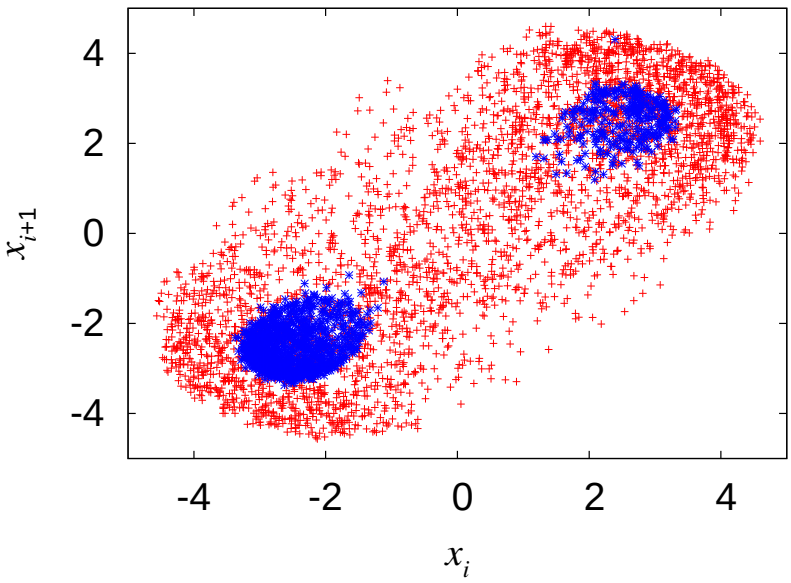

Figure 5.6: Projection of the invariant regions within the attractor, reconstructed from experimental data and separated using information from the application of the method of Chapter 3. Results were obtained at $\beta_1 = 3.78$.

here the same information was obtained solely from the experimental data.

5.3.3 Measuring Local Lyapunov Exponents

The sets separated from the attractor were then used to determine approximations to the short-time Lyapunov exponents. These should more correctly be termed *local Lyapunov exponents* since they are obtained from a subset of the total attractor.

The method of Wolf was used and histograms produced from averages of 75 consecutive time-steps. These are shown for the largest three Lyapunov exponents in Figure 5.7. The three values found for **D** (Subfigures (a), (b) and (c)) indicate one positive exponent in this invariant set, with another around zero and the third taking negative values. For **C** (Subfigures (d), (e) and (f)) there appears to be two positive local Lyapunov exponents.

This technique is extremely useful, as it is not usually possible to obtain information on the short-time Lyapunov exponents from experimental data. The

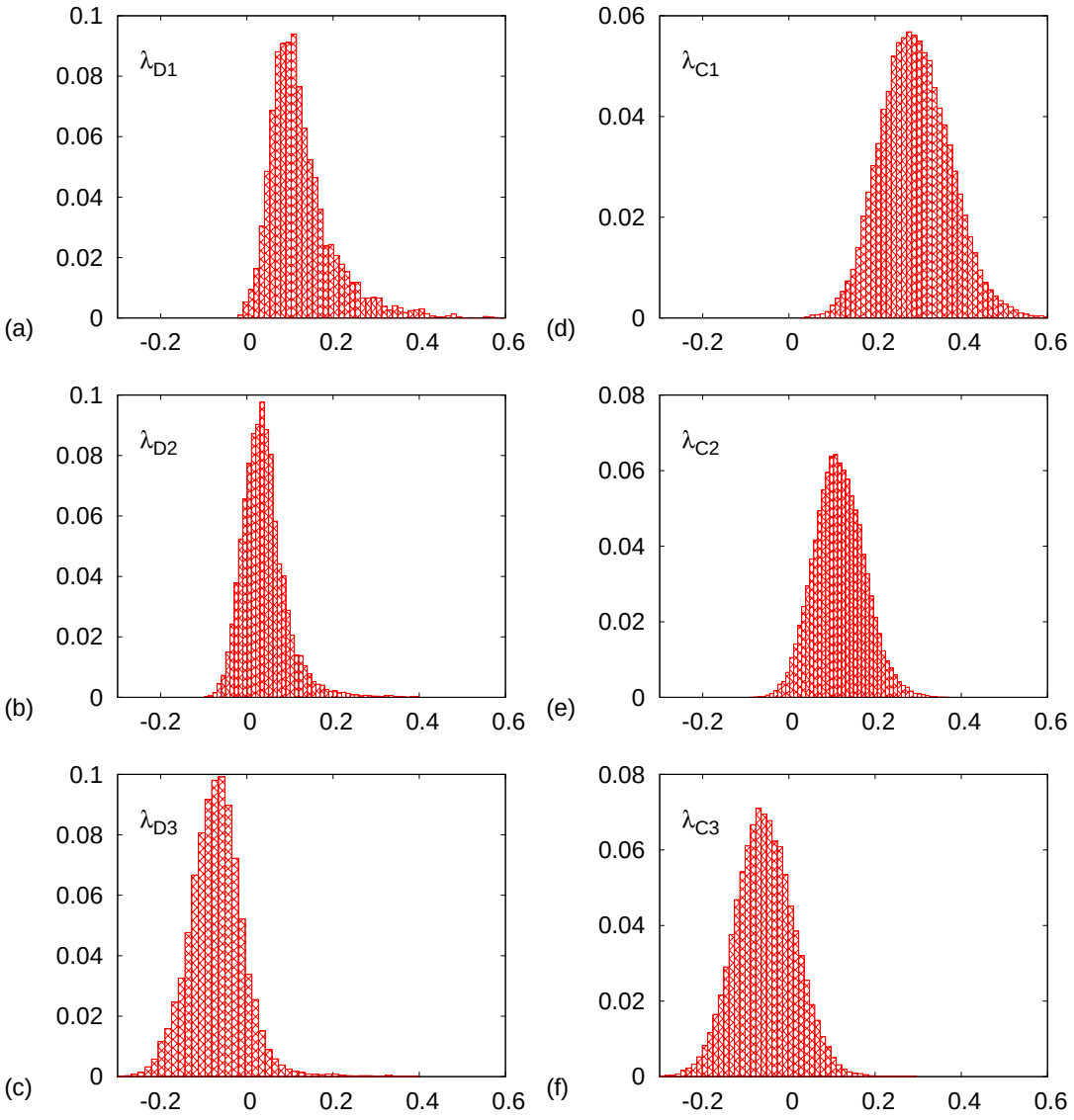

Figure 5.7: Local Lyapunov exponents obtained from the experimentally separated invariant sets of the attractor. Subfigures (a), (b) & (c) show histograms of the largest 3 Lyapunov exponents of **D** and (d), (e) & (f) of **C**.

results show that the invariant sets of which the attractor is composed have different numbers of positive STLEs and the attractor therefore suffers from UDV.

5.3.4 Measurement of Shadowing Times

As mentioned in Section 3.3.1, the presence of UDV implies a serious obstruction to shadowing, resulting in very short shadowing times. The discontinuities at nonhyperbolic points leads to the exponential divergence between true trajectories and a numerically generated ones, with shadowing times depending on the initial conditions of a given trajectory.

In the case of chaotic systems the sequence of values that the shadowing time takes can thus be considered to be a random variable. It has been shown that the statistics of shadowing times can be described by a random walk model which leads to a distribution of shadowing times $\phi(t_s)$ which is algebraic for small times and decays exponentially for large times [DL04]:

$$\phi(t_s) \approx \begin{cases} t_s^{-3/2} & \text{for small } t_s \\ \mathrm{e}^{\rho t_s} & \text{for large } t_s. \end{cases} \tag{5.1}$$

While the algebraic part of the distribution is universal, the exponent ρ in the part for long shadowing times depends on the parameters of the system.

To measure the shadowing times due to UDV, for example for $\beta_1 = 3.78$, a threshold value of the local mean distances $\mu^* = 0.488$ was defined, corresponding approximately to the minimum between the peaks in Figure 5.5(c), and then the number of time-steps between the points in the trajectory for which $\bar{\mu}$ crosses μ^* was counted.

The natural log of the distributions of shadowing times for $\beta_1 = 3.78$ are shown in Figure 5.8 (a). The results obtained show different scaling for short and long times, with exponential scaling for times over $0.1s$, in agreement with (5.1) and [DL04]. The exponents (ρ) of the probability distributions ($\phi(t_s)$) of shadowing times as a function of β_1 were determined and are presented in Figure

5.8 (b). Values that relate to times that trajectories spend in the hyperchaotic set (from **C**) and the chaotic set (from **D**) are shown separately. The exponents of shadowing time distributions for trajectories in the hyperchaotic set are found to remain approximately constant, with a decay exponent of $\rho = -4.9 \pm 0.3$ over the range of β. However, the gradients of $\ln(\phi(t_s))$ for trajectories in the chaotic set experience approximately quadratic decay as **D** is re-absorbed into **C**.

Therefore, as β is increased further into the regimes where the hyperchaotic set dominates, trajectories visit the low-dimensional chaotic set for progressively shorter times.

5.4 Summary

In this chapter hyperchaotic dynamics have been studied in the system of two oscillators coupled in a ring, as introduced in Section 4.3.2. Unstable dimension variability (UDV), a phenomenon which can exist only in hyperchaotic cases, has been measured over a range of parameter values. This form of non-hyperbolicity is detrimental to the reliability of numerical models of chaotic systems and therefore it is important to be able to ascertain over what parameter values it appears. The measurement of UDV was carried out using the newly developed technique introduced in Chapter 3, on time-series data from a physical system of coupled electronic oscillators.

In addition, the attractors at parameter values where UDV was found to be present were separated into their invariant sets using an extension of the same method. Estimates have been made of the local Lyapunov exponents using data from these separated sets. Also the shadowing times, a measure of the length of time for which numerical trajectories can be relied upon, have been calculated over a range of parameter values. It was found that, although the distribution of the lengths of time which trajectories stay in the hyperchaotic part of the attractor remains approximately constant over the studied range, they spend progressively

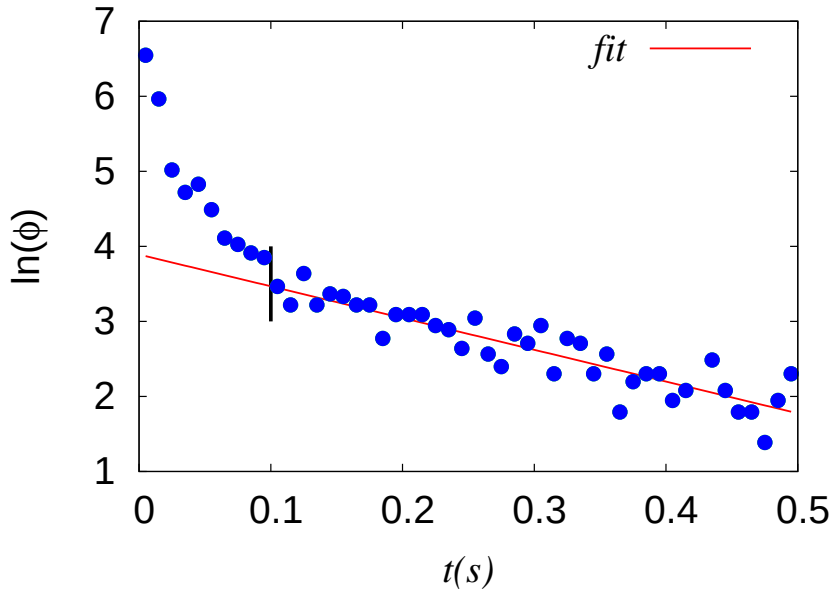

(a)

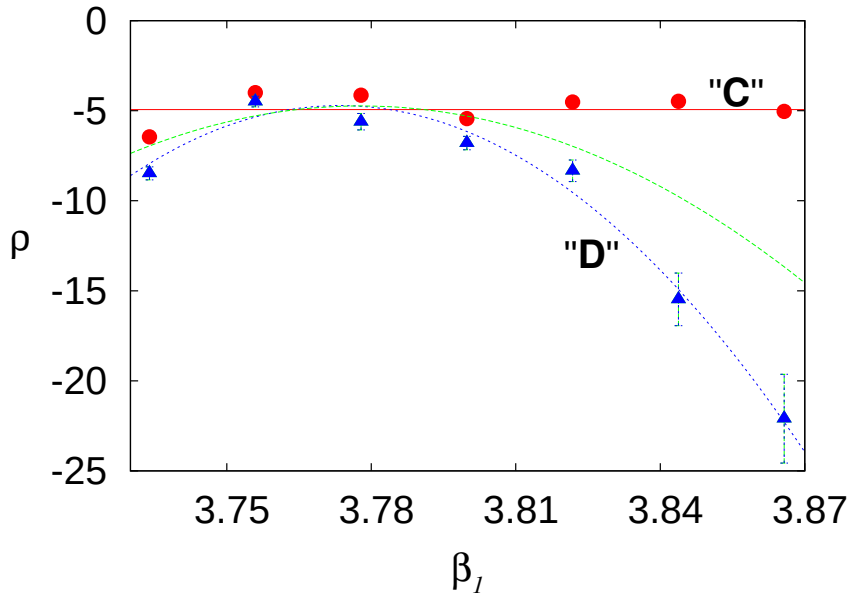

(b)

Figure 5.8: Shadowing times. (a): Values of the frequency of occurrence, ϕ, against times the trajectory spends in each of the invariant regions with two and one expanding directions are shown on a log scale. (b): Values of ρ, the gradient of the linear part of the shadowing time distributions, over a range of β_1.

shorter times in the smaller 1D unstable chaotic set, until it is hardly visited at all. After this point attractors of the system can again be assumed to have two unstable directions to the flow and be almost purely hyperchaotic.

Chapter 6

The Origins of Hyperchaos in the System of Coupled Oscillators

6.1 Introduction

As described in Chapter 5, hyperchaos has been uncovered in the system of two oscillators coupled in a ring. It is important to understand the origin of hyperchaos in systems capable of obtaining more than one positive Lyapunov exponent. This will help in understanding the structure of hyperchaotic attractors, which is currently not very well known. In the current system, hyperchaos first develops from bifurcations on the continuous branch of the original pitchfork bifurcation, as seen in Figure 5.1 on page 101. The various stable configurations which can exist have been described in Section 4.7.2 and shown schematically in Figure 4.10 on page 96.

In Chapter 5, it also was shown how unstable dimension variability (UDV) is encountered when this hyperchaotic saddle suffers a boundary crisis with chaotic attractors on the discontinuous branch. In the parameter regimes studied there, trajectories were found that visited parts of the attractor that were locally both low-dimensionally chaotic and (2D unstable) hyperchaotic, leading to fluctuations in the number of positive Lyapunov exponents (i.e. UDV). In this chapter

the emergence of hyperchaos in the present system is investigated. The dynamics found in different regions of parameter space are described along with the corresponding Lyapunov exponents of the system. The synchronisation relationship between the two subsystems is also investigated, as this gives rise to the existence of different invariant sets. It will prove important to understand how these sets lose stability to become nonattracting and then merge to form a single stable attractor.

It has previously been shown how stable attractors can be formed from the amalgamation of individually unstable nonattracting sets [Daw96]. In these cases the nonattracting invariant sets combine to form a globally stable manifold. A representation of this phenomenon is shown in Figure 6.1, with an unstable fixed-point and a chaotic saddle interacting to form a single stable attractor. It is therefore believed that attractors in high dimensional systems can be composed of nonattracting subsets, analogous to the way that chaotic attractors contain a set of unstable periodic orbits. The results in this chapter show that a hyperchaotic attractor is formed here in a similar manner, as two nonattracting, individually hyperchaotic sets merge. These sets are shown to each develop their own second positive Lyapunov exponent and become unstable at the same time as they individually become hyperchaotic. The transition to hyperchaos is shown to be due to bifurcations of the unstable periodic orbits contained within each attractor in the direction transverse to a direction of stability. A study of the attractor dimension using the methods of previous chapters is also carried out to confirm the route to hyperchaos in the system.

6.2 Region of Interest

Hyperchaos is first observed in attractors originating on the continuous "**C**" branch of the pitchfork bifurcation. This occurs on **C** before the discontinuous "**D**" branch appears (Fig. 5.1, page 101). Therefore, the system is now studied

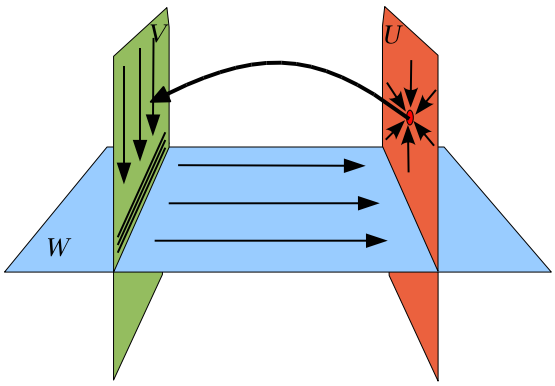

Figure 6.1: The combination of nonattracting sets to form a globally stable manifold. A saddle point on a manifold, U, with two locally contracting directions has an expanding direction from which trajectories are ejected. These intersect with a manifold containing a chaotic saddle, V, which contains a dense set of UPOs. Trajectories can escape from this via a 2D unstable UPO and traverse its local expanding manifold, W, to return to V. Thus the ensemble contains a stable attractor.

in this **C** region, at parameter values leading up to the emergence of a second positive Lyapunov exponent, to determine the origin of stable hyperchaos in the system.

For the following investigation, the parameters of the individual oscillators were kept as close as possible so that $\beta_1 = \beta_2 \equiv \beta$ in order to study the origin of hyperchaos more effectively. In previous studies of the coupled system ([KD99], [MM06] & Ch. 5) only a single parameter, β_1, was varied on one of the oscillators. While this is simpler experimentally, it complicates the analysis and understanding in terms of synchronisation. The effect of varying only one of the oscillators is to not only move through parameter space but also to detune the coupled oscillators, separating their natural frequencies ω_1 and ω_2 This separation of frequencies breaks the synchronisation far more quickly than just moving the two oscillators through the parameter space together, since synchronisation depends on the natural frequencies being similar. Therefore, here the individual "cells" of the system are kept almost identical.

The one parameter bifurcation diagram for the region of interest in **C** is shown in Figure 6.2, obtained by varying the combined parameter β and recording the

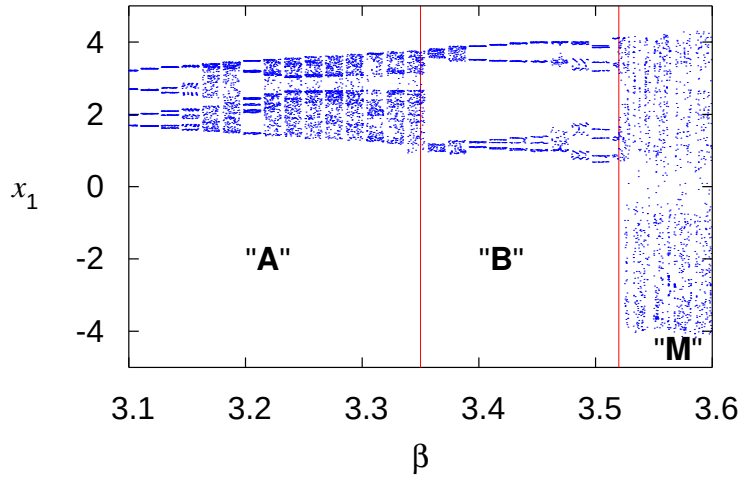

Figure 6.2: Bifurcation diagram for the two-in-a-ring system. Oscillations bifurcate to chaos in region **"A"** before returning to periodic states in region **"B"**. These then bifurcate to chaos again before a third state is encountered in **"M"**.

variable x_1. The dynamics here can be divided into three segments: **A**, **B** and **M**. The system first bifurcates from periodic behaviour to chaos in **A** before returning to periodic motion in **B** at $\beta \approx 3.35$. Another sequence of bifurcations is then encountered, resulting in the system again becoming chaotic. In **M**, starting at $\beta \approx 3.52$, trajectories are in the large "glued" attractor where two positive Lyapunov exponents were encountered in Section 5.1. It will be shown here that states **A** and **B** are different invariant sets in the combined phase space of the system and that **A** first becomes hyperchaotic and loses stability to **B**. The **B** set will also be shown subsequently to undergo a similar transition, this time resulting in the combination of **A** and **B** into one merged attracting set, **M**.

The difference between **A** and **B** lies in the relative phases of the oscillations of the two cells. Therefore, this phase relationship between these oscillations needs to be taken into consideration to understand the behaviour of the system and the transition to hyperchaos at these parameter values.

6.3 Synchronisation Sets and Phase Multistability

In a certain range of coupling strength and parameter mismatch, the oscillators are phase synchronised, whereby their frequencies become entrained and phases locked. In the considered parameter regimes the outputs of the two cells exhibit similar dynamics at any given value of β. This means that where cell 1 exhibits a limit cycle, so too does cell 2, and so on.

The averages of the variables $\bar{x_1}$ and $\bar{x_2}$ are related by a sign change such that $\bar{x_1} = -\bar{x_2}$, as outlined in Section 4.7.2. The oscillations of the individual oscillators can synchronise in two ways in this regime, resulting in two distinct states of the system. These states can be seen in Figure 6.3. In one of these *phase-states* the oscillations are in-phase and in the other they are π out-of-phase (anti-phase). Additionally, the attractors found in **B** can be followed back into the **A** region by decreasing the parameter, β. Thus both states coexist in the **A** region of parameter space, and are both stable there. However, oscillations shown in the **A** region are always obtained when resetting the system at these parameter values. In Huygens' original work on synchronisation only the anti-phase state was observed [Huy01], but this has been shown to be a feature of the specific system he used [BSRW02; Ble88]. Both in-phase and anti-phase oscillations have been observed in a range of systems [Ble88; HKB85; PVS$^+$99]. This form of phase degeneracy was shown in [PVS$^+$99] to be important in understanding the transition to hyperchaos.

At parameter values just above the Hopf bifurcation the oscillations are almost sinusoidal and symmetric under the transformation $[t \rightarrow t+T/2, (x-x_0) \rightarrow -(x-x_0)]$, where T is the period and x_0 the focus of oscillation. However, at higher parameter values the oscillations are asymmetric and contain higher harmonics and $x_n(t) \neq -x_n(t+T/2)$. In these cases there is a mirror symmetry about the time axis between the states of the two oscillators, such that $x_1(t) = -x_2(t)$ for

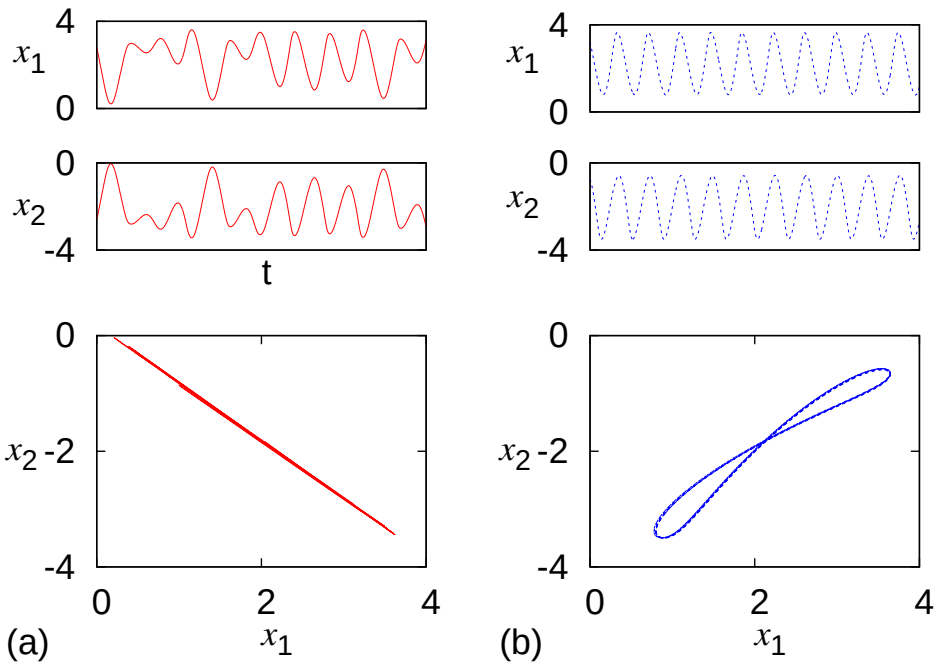

Figure 6.3: Phase multistable states. At low β the oscillators can lock in two states. In (a) oscillations are symmetrically synchronised whereas in (b) they are synchronised but do not have perfect symmetry. States found in regions "**A**" and "**B**" in Figure 6.2 are of the type shown here in (a) and (b), respectively. The oscillations of **A** exhibit perfectly synchronised chaos (of opposite sign) at the same value of β where **B** are limit-cycle.

one state and $x_1(t) = -x_2(t+T/2)$ for the other. These properties can be seen in the time-series in Figure 6.3 (a) and (b), respectively. For the phase relationship shown in (a), $x_1(t) = -x_2(t)$; so it is convenient to consider this case as *in-phase* (or *symmetric*). Conversely, states having the phase relationship shown in (b), where $x_1(t) = -x_2(t+T/2)$, are hereby considered *out-of-phase* (or *asymmetric*). The symmetric, in-phase oscillations are those found in **A** and the out-of-phase, less symmetric in **B**, following the scheme introduced in Figure 6.2.

As noted above, in the **A** region of parameter space, both of the states **A** and **B** coexist. This gives a multiplicity of states within this range of β, either of which can be selected by careful manipulation of the coupled system. The attractors of **A** are found to bifurcate to chaos at lower β than those of **B**, as seen in Figure 6.2. Notably, **B** states are limit cycle until after **A** has bifurcated to chaos. Oscillations in **A** and **B** are shown in Figure 6.3 (a) and (b) at the same value of β. The qualitative dynamics and quantities such as the Lyapunov exponents and stability to perturbations or detuning are therefore different for each of the two states.

6.3.1 Symmetry and Stability in the Phase Degenerate States.

Two uncoupled, almost identical oscillators experience their respective bifurcations at the same parameter value as each other. This is the equivalent of the limit where the coupling strength $\sigma \to 0$. As σ is increased, the two systems interact more strongly, with the various bifurcations shifting in parameter space. Furthermore, it is found that bifurcations for states synchronised in-phase (**A**) and out-of-phase (**B**) are shifted by different amounts. This separates the dynamics of the two phase-states in parameter space, with **A** bifurcating to chaos at lower values of β than **B**.

Bifurcations of **A** and **B** were studied experimentally to determine how they separate as the coupling strength is increased and the results are shown in

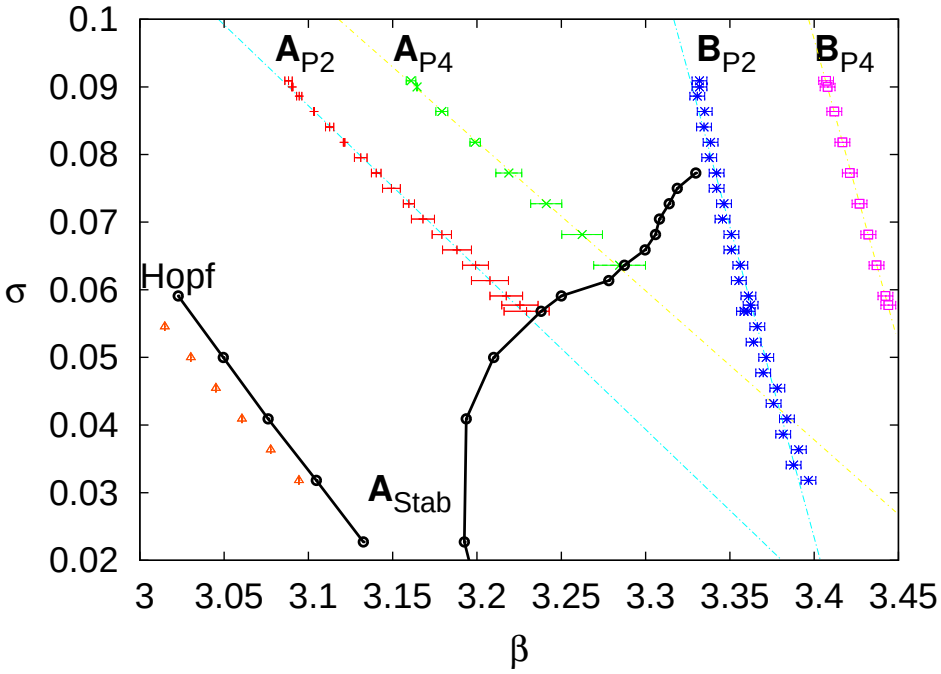

Figure 6.4: Shift of bifurcations in β with increasing coupling σ for both **A** and **B** states. The limits of stability of the less stable **A** state ($\mathbf{A}_{\mathrm{Stab}}$) and the loci of Hopf bifurcations are also shown. Subscripts P2 and P4 refer to the transition to period-2 and period-4 oscillations respectively.

Figure 6.4. Here, the loci of Hopf and the first two period doubling bifurcations of both **A** and **B** are shown in β–σ parameter space. The limits of stability of the less stable **A** state are also shown.

Both **A** and **B** originate from a common Hopf bifurcation, which is offset to lower values of β as σ is increased. This is due to the coupling dislocating the primary pitchfork bifurcation, resulting in a parameter offset in all subsequent bifurcations to lower values (Sec. 4.7.2 on page 94 & Fig. 4.10 on page 96). As the coupling strength is increased, the period doubling bifurcations of **A** approximately follow the Hopf bifurcation in their relative displacement. However, in the case of **B**, the parameter difference between the Hopf and the first period doubling ($\beta_{\mathrm{P2}} - \beta_{\mathrm{Hopf}}$) increases on increasing σ. This behaviour can be understood using symmetry arguments in the combined system, as follows.

Recalling that the equations of motion have the form:

$$\dot{x}_{1/2} = g(x_{1/2}, y_{1/2}) + h(x_{1/2} - \sigma x_{2/1}), \tag{6.1}$$

where g and h are functions obtained from Equation (4.2), the phase difference between the solutions of the two oscillators can now be taken into consideration. Considering only the symmetry in the form of the oscillations and taking the two solutions $x_1(t) = -x_2(t)$ (for **A**) and $x_1(t) = -x_2(t + T/2)$ (for **B**),

$$\dot{x}_{1/2}(t) = g(x_{1/2}(t), y_{1/2}(t)) + h((1 + \sigma)x_{1/2}(t)) \tag{6.2}$$

and

$$\dot{x}_{1/2}(t) = g(x_{1/2}(t), y_{1/2}(t)) + h(x_{1/2}(t) + \sigma x_{1/2}(t + T/2)) \tag{6.3}$$

are obtained for **A** and **B** respectively. Now, since $x_1(t)$ and $x_2(t)$ are asymmetric under $[t \to t+T/2, x \to -x]$, it can be seen that the two phase-states lead to two unique systems which diverge more as both σ is increased and as the asymmetry of the individual oscillations increases on increasing β beyond the Hopf bifurcation. It is clear from (6.2) that, as long as the oscillators are in perfect anti-phase synchrony, the coupled system is simply a parameter-shifted version of the single oscillator.

To see the increased symmetry of **B** with respect to **A**, the ansatz $x = \cos(t) + \kappa\cos(2t)$[1] is taken as the simplest solution of the equations which is not symmetric under $[t \to t+T/2, x \to -x]$. Thus the equations of motion for **A** and **B** become:

$$\dot{x}_{1/2}(t) \;=\; g(x_{1/2}(t), y_{1/2}(t)) + h((1 + \sigma)\{\cos(t) + \kappa\cos(2t)\}) \tag{6.4}$$

[1]The amplitude and frequency have been normalised here for simplicity.

and

$$\begin{aligned} \dot{x}_{1/2}(t) &= g(x_{1/2}(t), y_{1/2}(t)) \\ &\quad + h(\cos(t) + \kappa\cos(2t) + \sigma\{\cos(t + T/2) + \kappa\cos(2t)\}) \end{aligned} \tag{6.5}$$

respectively. For β values just above the Hopf bifurcation, where $\kappa = 0$ and oscillations are harmonic, increasing the coupling strength σ from $0 \rightarrow 1$ results in $h(V)$ in Equation (6.5) going towards zero. However, at higher β where the oscillations become more anharmonic and κ increases, the second part of Equation (6.5) tends to $h(2\kappa\cos(2t))$ as σ tends to unity, giving extra symmetry to the oscillations of the system.

The theory of Swift describes the effect of symmetry on period doubling bifurcations [SW84]. It was proved there that, for a large class of systems, period doubling bifurcations are suppressed if symmetry exists in the solutions under the transform $[t \rightarrow t + T/2, x \rightarrow -x]$, until symmetry-breaking occurs. Therefore, a possible mechanism can be seen for the extra stability of the limit cycle in **B** to bifurcation and chaos.

6.3.2 Transition Between Phase States

The symmetric and asymmetric states (here, **A** and **B**) are stable within a different range of detuning of the individual oscillators, similar to previous work on phase multistability. The work of Postnov *et al.* describes the coexistence of both in-phase and anti-phase synchronised attractors in a system, dubbed *phase multistability* [PVS$^+$99]. There, phase multistability was found numerically in a coupled Rössler system, with one state losing stability to the other, before they both merged into a single hyperchaotic attractor. The work described in [Daw96] shows how such a stable hyperchaotic set can be formed from invariant nonattracting subsets.

In the physical system under investigation here, a second Lyapunov exponent

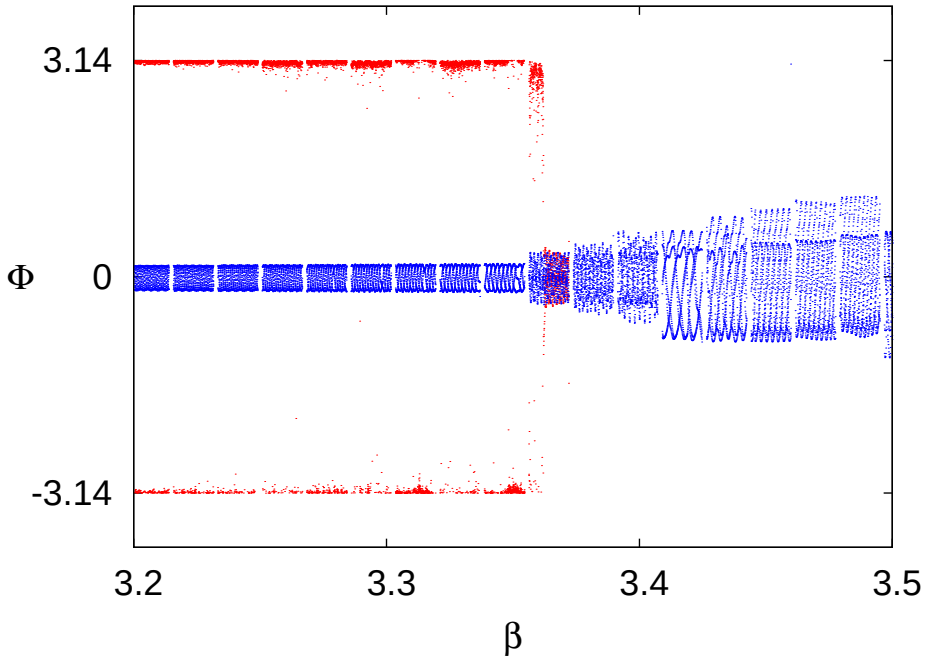

Figure 6.5: One parameter bifurcation diagram based on the relative phases of the oscillators. The difference in the phases $\Phi = \phi_1 - \phi_2$ is shown at various β in the bifurcation diagram. The **A** state (red) loses stability to the **B** state (blue) as β is increased.

is also found to exist after the two phase-states have merged into a single attractor (**M**), similar to previous numerical studies. Additionally here, **A** bifurcates to chaos at lower β than **B** and then loses stability to it as β is increased. The bifurcations with respect to the phase relationship between the oscillations of the two cells have been investigated, in order to better understand this behaviour. The relative phases of the oscillations were obtained from experimental data using the analytic signal method by performing a Hilbert transform on the time-series (Sec. 2.2.4, page 63). The bifurcation diagram showing these phases as a function of β is shown in Figure 6.5.

Just after the point where **B** loses stability to **M**, the system jumps intermittently between the two phase states **A** and **B**. This type of behaviour was also noted in the numerical work on previous phase-multistable systems. Shortly after **B** and **A** have merged into **M**, trajectories are found to visit all the sets

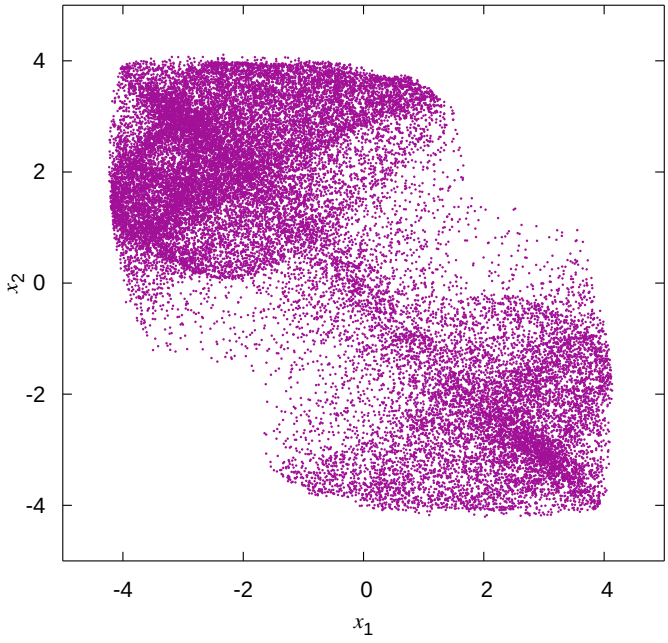

Figure 6.6: Projection of the attractor of the combined **A** and **B** sets. The hyperchaotic attractor resembles a double-ended mushroom, with the "glued" **A** set ("stem") connecting the two **B** sets ("heads").

that exist at these parameter values. In these cases the two **A** sets ($\bar{x} > 0$ and $\bar{x} < 0$, respectively) have been connected by a gluing bifurcation. This serves to also connect the positive with the negative x_n sets of **B**, as can be seen in Figure 6.6.

At lower β trajectories fluctuate intermittently between **A** and **B** but at higher parameter values it is impossible to tell that the attractor is composed of invariant subsets and only one large hyperchaotic attractor is observed. The schematic representation of the various transitions given in Figure 6.7 illustrates clearly how **A** and **B** interact in the different parameter regimes to form the stable attractor, **M**.

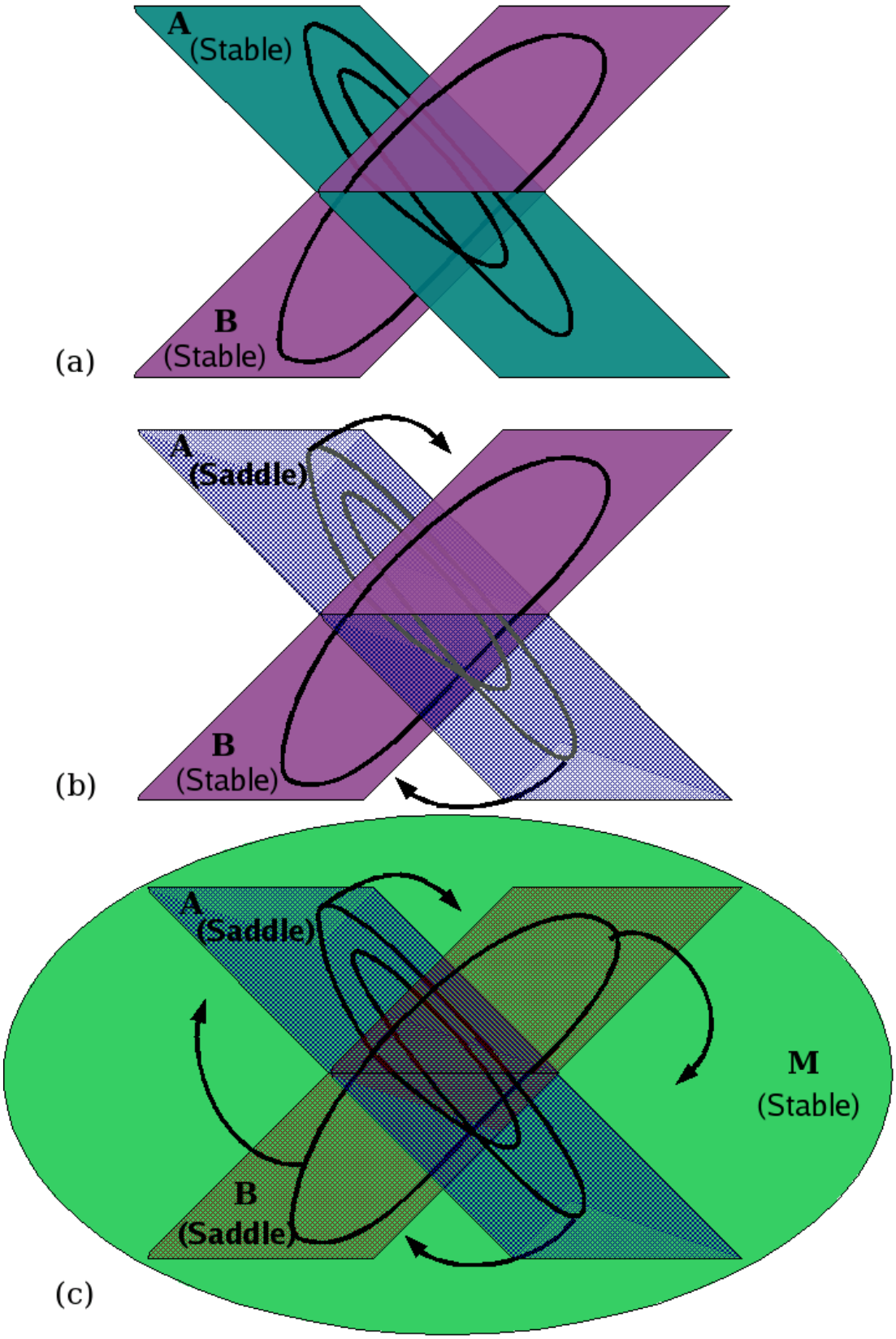

Figure 6.7: Interaction of invariant sets in the system. At lower parameter values, (a), both **A** and **B** are stable, but **A** is "preferred" by the system. At intermediate β, (b), **A** becomes a saddle and states all end up on **B**. When **B** becomes a saddle, (c), both nonattracting sets combine to form a globally stable set, **M**.

6.4 Lyapunov Exponents of the States

To investigate the origin of hyperchaos in this combined attractor, the Lyapunov exponents of the system were obtained from experimental data using the method of Wolf described in Section 2.2.2. These are shown along with the related bifurcation diagram in Figure 6.8. The first physical observation of two positive Lyapunov exponents is at the point where **A** and **B** combine in **M**. This is in agreement with the numerical study of Postnov *et al.* on the coupled Rössler system, where hyperchaos came about as a result of the merger of two phase-states.

It is important to understand whether the second positive Lyapunov exponent in **M** comes from either of the individual sets or purely from the combination of the two. To achieve this, the Lyapunov exponents of **A** and **B** were calculated individually using numerical methods. In cases where the set under investigation was an unstable saddle, the sets were separated using the PIM-simplex method outlined in Section 2.1.3 and in all cases the Lyapunov exponents were determined using the method of Benettin described in Section 2.1.2. The results of the application of these methods to **A** are shown in Figure 6.9. Here it can be seen that the loss of stability of **A** coincides with one of the negative Lyapunov exponents crossing zero. Therefore, at this point **A** becomes a nonattracting set of the system with two expanding (unstable) directions to the flow.

The loss of stability of **B** and resulting coalescence with **A** on further increasing β was studied using the same numerical methods as above. Results are shown in Figure 6.10, where it can be seen that a second positive Lyapunov exponent also emerges in **B**. Similar to the case of **A** states, **B** also becomes a hyperchaotic nonattracting set at this point. However, in this case **B** combines with **A** to form **M**, a globally stable hyperchaotic attractor composed of individually nonattracting subsets.

This provides evidence that the Lyapunov exponents in **M** just after the merger come from a combination of those from the individual sub-sets, due to the fluctuation of trajectories between **A** and **B**. Hyperchaos is experimentally

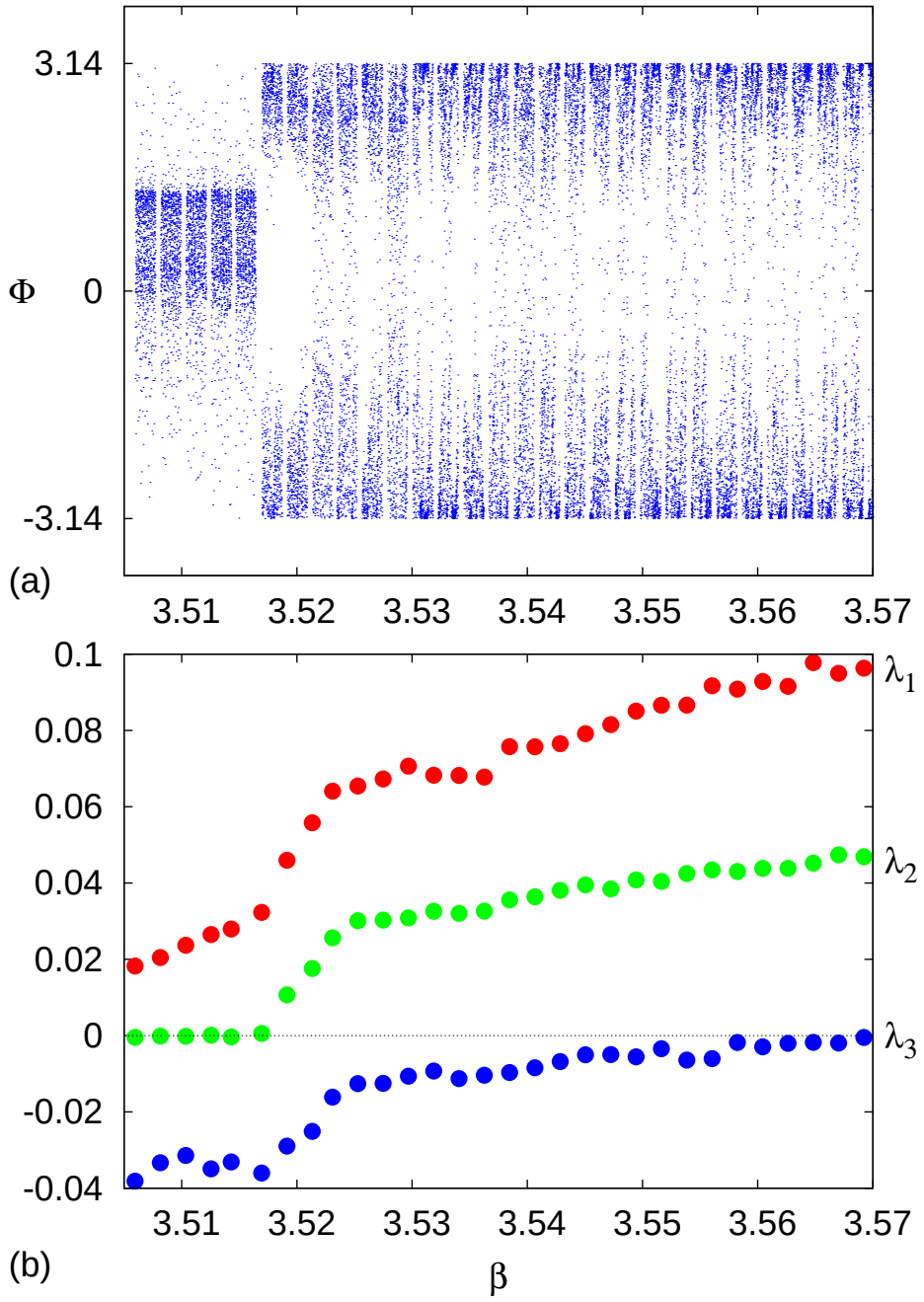

Figure 6.8: Experimental results showing the transition from chaos to hyperchaos as phase states **A** and **B** merge.

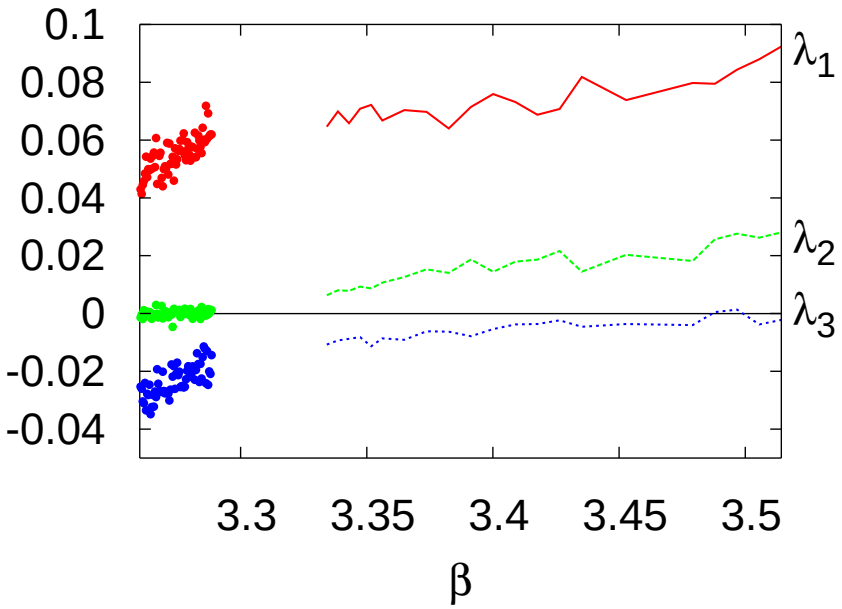

Figure 6.9: The development of a second positive Lyapunov exponent in **A**. Lines show where **A** is unstable and the set was isolated using the PIM-simplex routines.

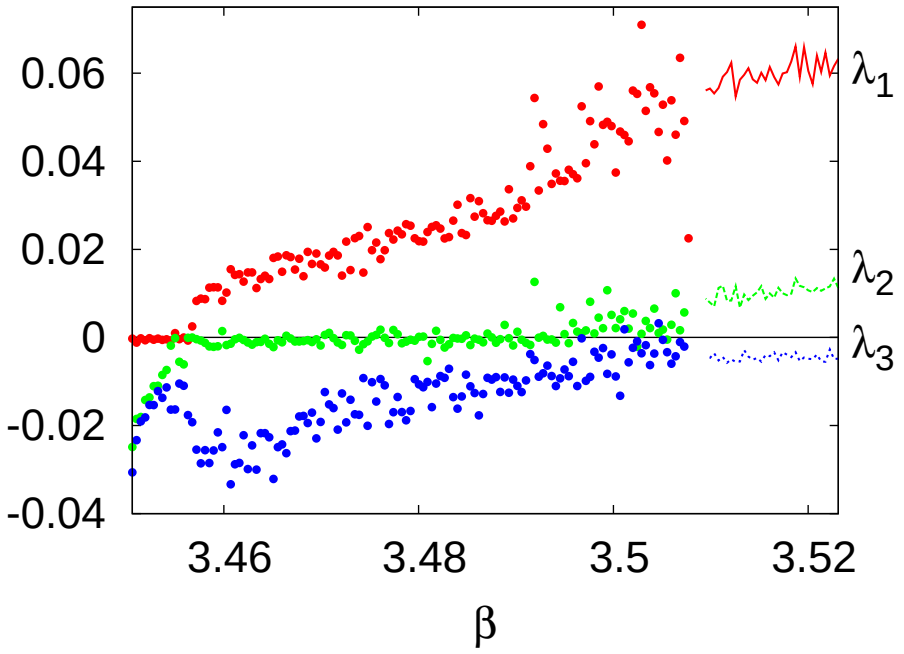

Figure 6.10: The Lyapunov exponents of **B** as it approaches instability and merges with **A**. Lines follow **B** states into the unstable region.

observable in the system only after the two sets have merged, due to the loss of stability of each set at its respective transition to two positive Lyapunov exponents. The above results also demonstrate that the development of two expanding directions in the system is smooth in both **A** and **B**; i.e. there is no discontinuous transition of the Lyapunov exponents of either of the invariant sets.

6.5 Loss of Synchronisation and Increase in Unstable Dimension

The appearance of a second Lyapunov exponent in coupled systems and the induced increase in the dimension of the local manifold in phase space is associated with a reduction in the synchronisation between oscillations of the subsystems (cells). The degree of synchronisation between the subsystems was studied in order to understand the origin of the second positive Lyapunov exponent in each

of the interacting sets of the system, the results of which are presented in Section 6.5.1.

In **A** the oscillators are initially completely synchronised, as can be seen in the phase plot in Figure 6.3 (a). This perfect synchronisation persists until the oscillations are well into chaotic regimes, but weakens as the system moves towards hyperchaos. Generalised synchronisation (GS) is expected in these regimes, where there is only a single positive Lyapunov exponent. A smooth transition to two positive Lyapunov exponents would suggest a riddling bifurcation, whereby UPOs in the attractor start to bifurcate and lose stability in the direction transverse to the synchronisation manifold [KMP00]. This can be detected by looking for a reduction in GS between the two oscillators, investigations on which follow.

Additionally, the topological dimension is investigated using the method introduced in Chapter 3 and used in Chapter 5 for detecting UDV, in order to search for direct evidence of trajectories leaving the lower dimensional manifold along the bifurcated orbits. The results of this investigation are presented in Section 6.5.2. Finally, the statistics of the phase synchronisation for orbits in the combined attractor **M** are investigated in Section 6.5.3, in order to determine how the invariant subsets **A** and **B** finally interact within **M**.

6.5.1 Generalised Synchronisation

Investigations were conducted to determine whether the appearance of a second positive Lyapunov exponent is accompanied by an associated reduction in generalised synchronisation (GS), as predicted by theory. The level of GS was measured using the ε–δ test outlined in Section 2.2.4. Results of this investigation on experimental data are presented in Figures 6.11–6.14. A set of points $(x_1(t_{k1}), x_1(t_{k2}), \dots)$ around a trajectory point $x_1(t_{k0})$ was found within a maximum radius δ_{max}, from embedded time-series measurements on the first system (O1). The equivalent points $(x_2(t_{k1}), x_2(t_{k2}), \dots)$ in the second system (O2) were located at corresponding times, and the maximum distance ε_{max} from $x_2(t_{k0})$

recorded. The radius δ was progressively reduced and the procedure repeated to produce a curve showing the dependence of ε on δ. Histograms produced from many measurements of $\log_{10}\varepsilon$–$\log_{10}\delta$ with different $x_1(t_{k0})$, over long trajectories are shown in subfigures (c) and (d). In these representations, the density of data at each value of $\log_{10}\varepsilon$ and $\log_{10}\delta$ is shown by variation of the plotted colours.

The degree of GS was found to be variable in time. Looking at this time-dependence, GS was found to be stronger when trajectories were in the less curved cycling regions of the attractor. Small discontinuities, with a partial weakening of GS, were observed around folding and re-injection points, where the attractor is less hyperbolic. However, as a time-average the systems can be seen to have a strong degree of GS at these parameter values. Also, the sets of points S(δ) and S(ε) on attractors from O1 and O2 are shown each in two different projections in (a1), (b1), (a2) and (b2), respectively in Figures 6.11–6.14. The colour gradient indicates variation in the distance of points in S(δ) from the centre of the set, in order to show the degree of correlation between S(δ) and S(ε) directly.

A representative selection of results at four different parameter values are given in Figures 6.11–6.14, at $\beta = 3.18$, 3.34, 3.378 and 3.51, respectively. At parameter values in regions of **A** where oscillations are perfectly synchronised, GS is also perfect, as expected. When one of the negative Lyapunov exponents approaches zero in **A**, strong GS is detected. However, on short timescales fluctuations were seen, indicating local deviations from the synchronisation manifold. In **B**, complete synchronisation is not found, due to symmetry reasons outlined in Section 6.3.1. Here, GS is weaker than previously, but still strongly detectable; indicating the existence of a largely 1D unstable manifold on average. As a second expanding direction to the flow starts to develop and **B** approaches the point of instability, GS becomes almost undetectable. This can be seen in the sets S(ε) compared to S(δ), as well as by a lack of a distinct correlation in the ε–δ tests. However, in this domain a degree of phase synchronisation can still be observed by the bounding of the angular distribution of S(ϵ) compared to the overall extent

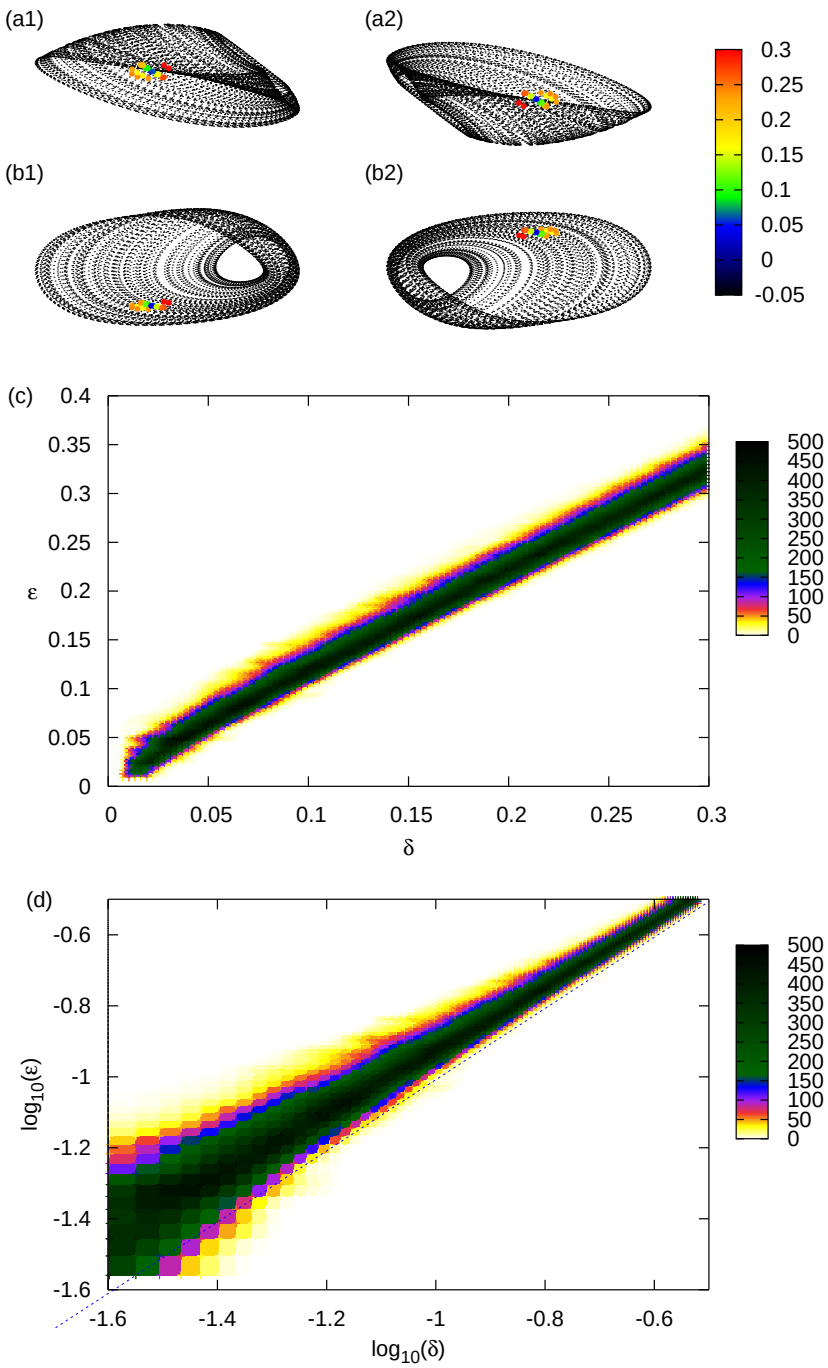

Figure 6.11: In regimes where complete synchronisation is found, the ε–δ test shows an almost perfect straight line both in plots of $\log_{10}\varepsilon$ against $\log_{10}\delta$ and in plots of ε against δ on a linear scale. Here $\beta = 3.18$, in the perfectly synchronised chaotic region of **A**. Subfigures (a1) and (b1) show two projections of the first subsystem O1 and (b1) and (b2) of O2.

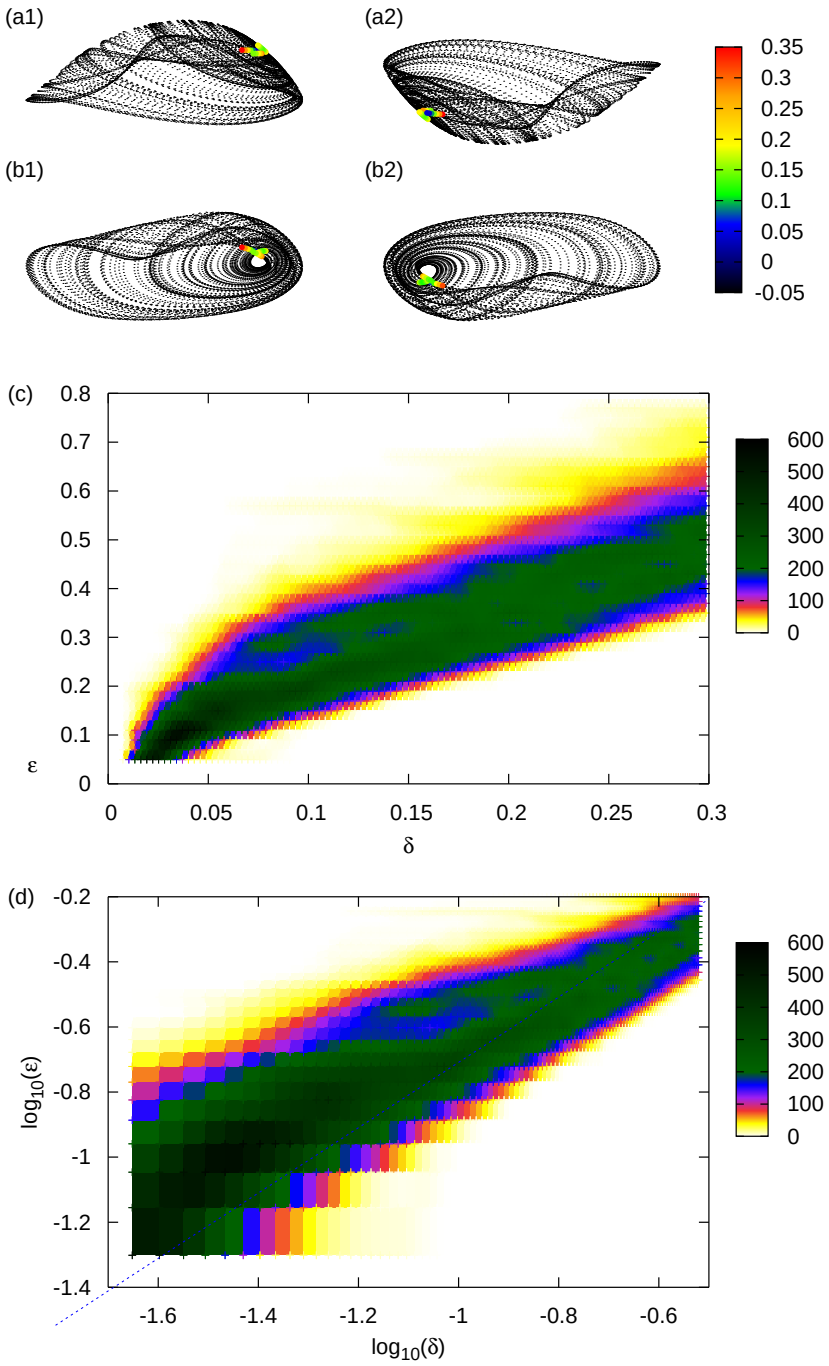

Figure 6.12: As **A** approaches having a second positive Lyapunov exponent (here at $\beta = 3.34$) and the limit of its stability, strong GS is found as a time-average, but fluctuations are found on short timescales.

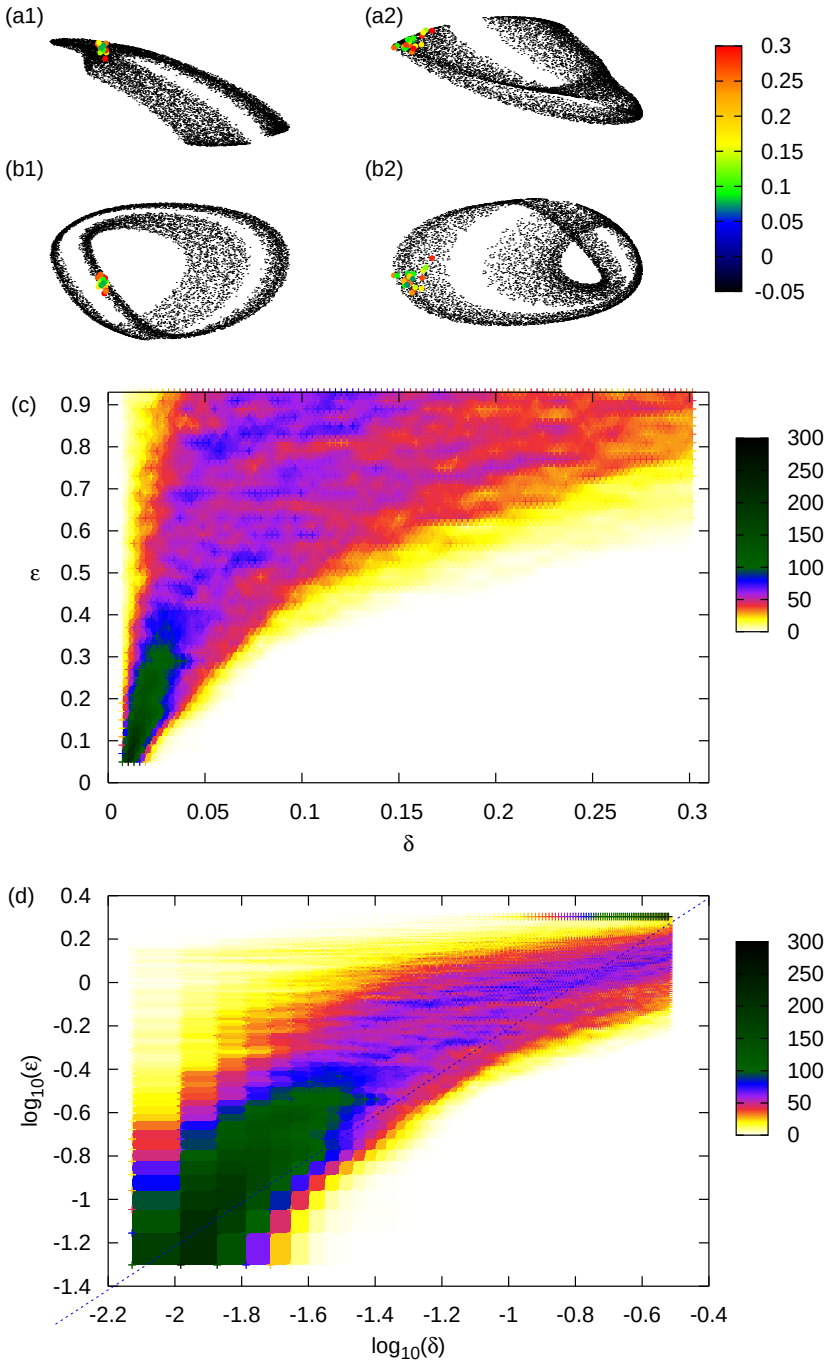

Figure 6.13: In **B**, GS is much weaker, but still detectable; indicating the existence of a largely 1D unstable manifold on average. These results were obtained at $\beta = 3.378$.

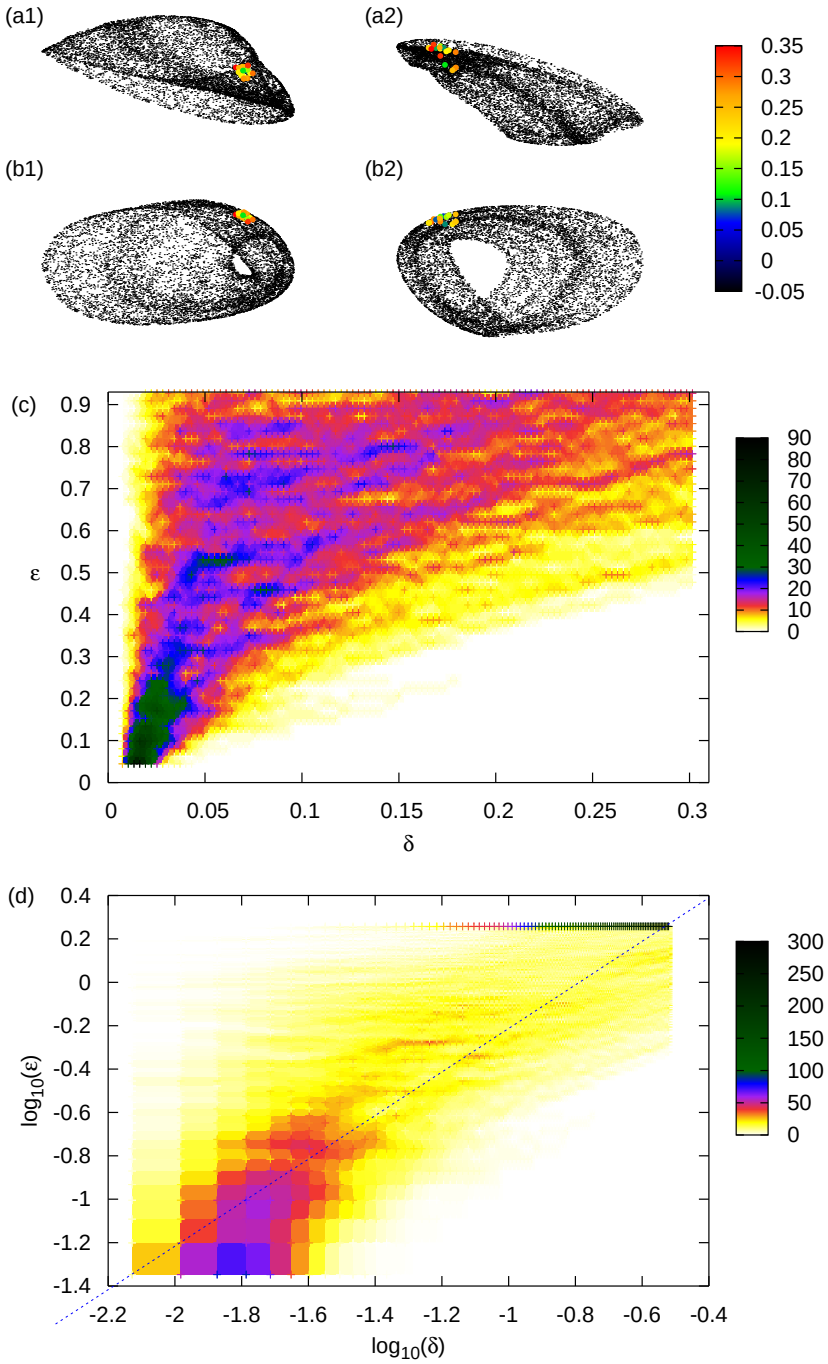

Figure 6.14: As **B** approaches instability, close to the emergence of a second expanding direction to the flow on average, GS becomes almost undetectable. This indicates that at parameter values such as these (here $\beta = 3.51$) more of the UPOs within the attractors have bifurcated.

of the attractor.

Generalised synchronisation was found to be completely undetectable using the ε–δ test in the mixed **M** regime. At these parameter values, investigations on the time evolution of the of points in S(δ) and S(ε) revealed that S(ε) became shuffled at regular intervals; particularly around re-injection points. As outlined in Section 1.2.11, the loss of GS is related to the emergence of a second positive Lyapunov exponent in systems as they become hyperchaotic. In Section 2.2.4 it was explained how this can occur when unstable periodic orbits (UPOs) lose stability transverse to the synchronisation manifold in a riddling bifurcation leading up to a blowout bifurcation. This leads to a phenomenon known as *bubbling* of the attractor, where trajectories intermittently deviate from the synchronisation manifold when hitting one of these bifurcated UPOs. The results here show a steady loss of general synchronisation at parameter values leading up to the emergence of a second positive Lyapunov exponent. This is in accordance with theoretical work described previously, and strongly suggests that the mechanism responsible for the transition to hyperchaos is via riddling of the attractor by the bifurcation of embedded UPOs.

6.5.2 Topological Dimension Measures

The results so far have suggested that the transition to hyperchaos with the emergence of a second Lyapunov exponent in the system is due to transverse loss of stability of UPOs in the attractor – a bubbling bifurcation. This provides a mechanism for a smooth transition to hyperchaos in coupled systems [KMP00]. In order to further measure the transition from one to two expanding directions in the system and confirm the above results, the local topological dimension was investigated. If attractors are indeed experiencing bubbling as orbits deviate from the synchronisation manifold when they encounter a transversely bifurcated UPO, this should be detectable by the local dimension of the set of embedded points steadily increasing as this behaviour becomes more prominent on increasing β.

The method for detecting variations in the local dimension introduced in Chapter 3 was applied over the range of β shown in Figure 6.8. A selection of histograms of averaged mean interpoint distances $\bar{\mu}$ in the reconstructed attractors are given in Figure 6.15.

The peaks in the probability distributions are seen to make a smooth transition from the value associated with a locally two dimensional manifold (i.e. containing mainly 1D unstable orbits) towards one with two expanding directions to the flow. This indicates that steadily more of the UPOs contained in the attractor are bifurcating and becoming transversely unstable, thereby displacing trajectories evermore away from the synchronisation manifold. A second peak is seen to emerge in the histograms as the **A** state is reabsorbed into the attractor. The peaks for **A** are at greater $\bar{\mu}$ than **B** at the same parameter values because **A** has bifurcated to hyperchaos at lower β than **B** and contains more 2D unstable UPOs. This leads to embedded points in the vicinity of **A** being more spread into the direction transverse to the synchronisation manifold than in **B**. Therefore UDV appears strongest whilst there is mixing between **A** and **B**, demonstrating the existence of different numbers of bifurcated and un-bifurcated UPOs in the combined manifold of the system.

The histograms are presented in a more compact representation in the three dimensional histogram of Figure 6.16. Each vertical slice of this graph consists of a histogram the same as those used in the previous figure, with the colours indicating the relative occurrences at each value. A smooth transition in the dimension can be seen, as would be expected if progressively more UPOs become unstable along previously contracting directions, forcing trajectories away from the synchronisation manifold. The re-absorption of **A** into **B** can also clearly be seen in this figure. Finally, as **A** again dominates, the dimension is seen to tend towards that of a hyperchaotic attractor containing two directions along which trajectories from different initial conditions will diverge.

The riddling of attractors provides a mechanism for a smooth loss of stability

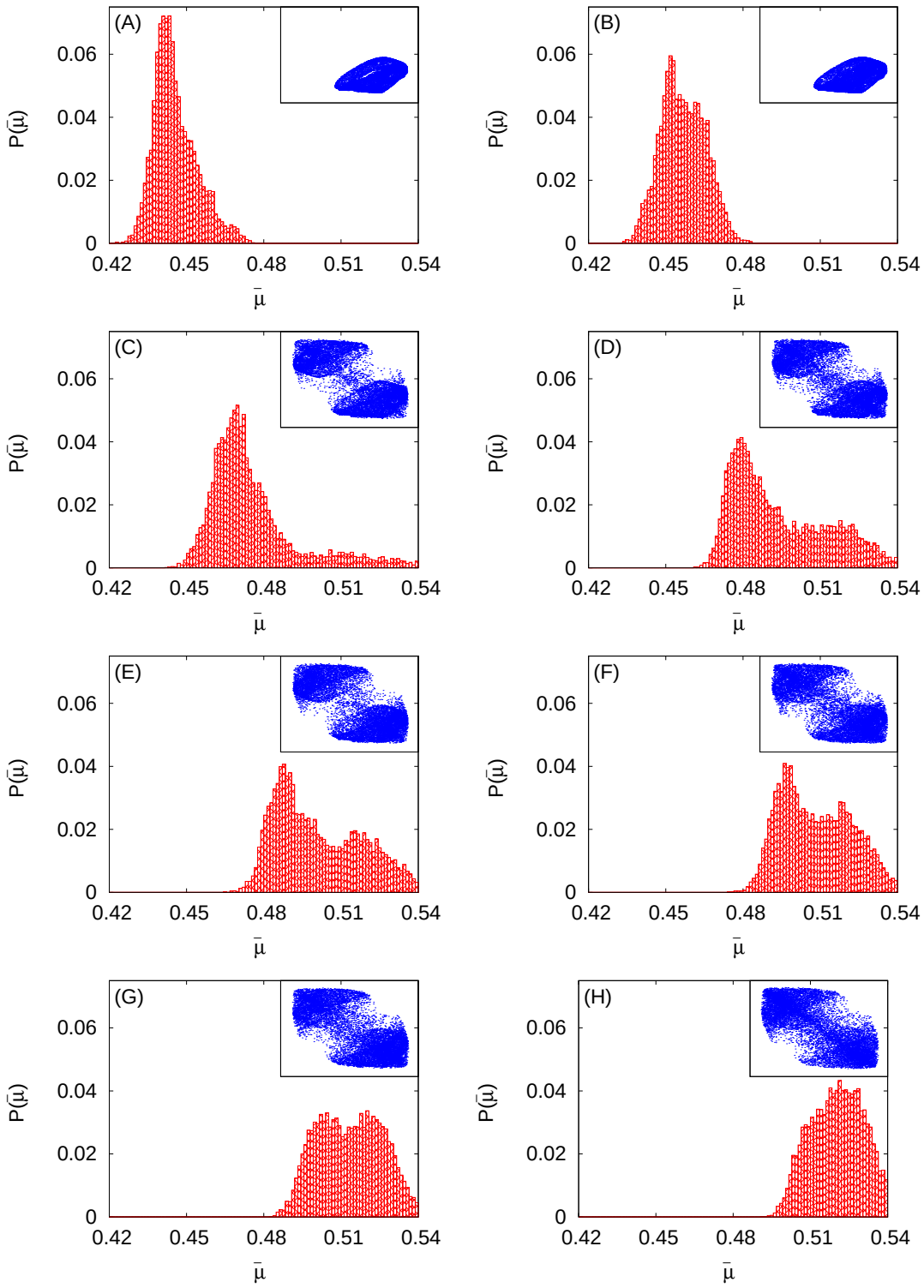

Figure 6.15: Distributions of $\bar{\mu}$ at various parameter values. A steady transition to higher dimensional dynamics is observed. The corresponding attractors projected onto the x_1–x_2 plane are shown inset. Values of β are A: 3.506, B: 3.510, C: 3.519, D: 3.523, E: 3.527, F: 3.541, G: 3.522 and H: 3.580.

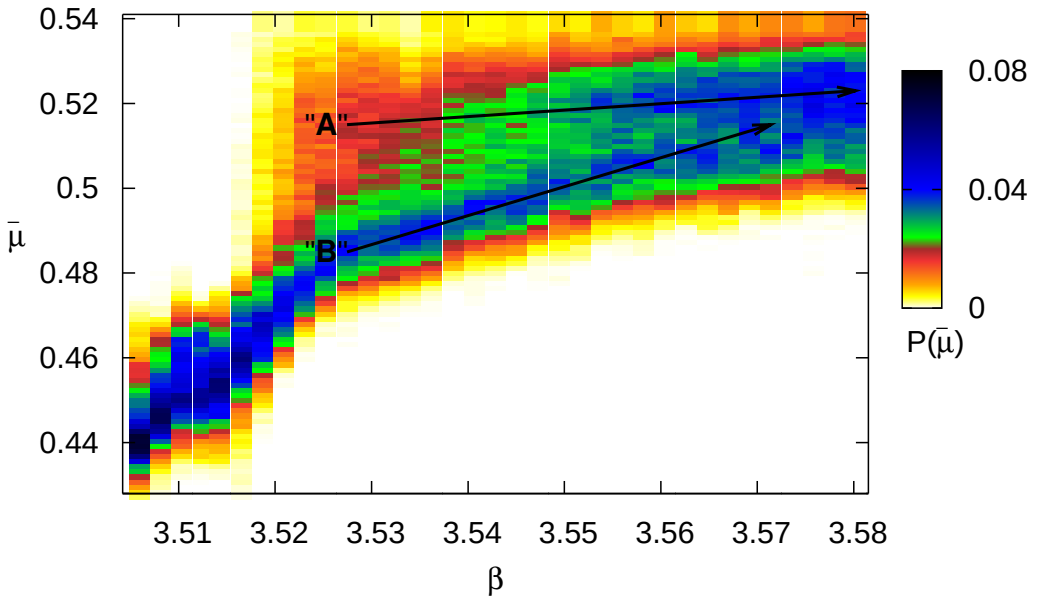

Figure 6.16: Combination of histograms for the range of β where **A** and **B** combine into the mixed state **M** and a second Lyapunov exponent emerges in the system

of a previously contracting direction and a route to hyperchaos in synchronised systems. The above results show clear evidence of such a smooth transition, demonstrating that this is the origin of high dimensional dynamics in the system. States in both **A** and **B** are therefore believed to develop a second Lyapunov exponent via this route, whereby they become nonattracting sets. These eventually combine to form a single merged hyperchaotic attractor **M**, containing within it the remnants of both **A** and **B**.

6.5.3 Interaction of the Phase Synchronised States

In order to fully understand how the two phase-states **A** and **B** interact and combine to form the merged hyperchaotic attractor **M**, the phase synchronisation at various parameter values was studied. The phase difference $\Phi = \phi_2 - \phi_1$ between the subsystems 2 and 1 was obtained using the analytic signal method given in Section 2.2.4. Time-series of Φ are shown in part (i) of Figures 6.17 (a), (b) and (c), with histograms showing the distributions of the density of points as a function of Φ in (ii). In the **A** set the phases of O1 and O2 were found to be completely locked, with the phase difference fixed at $\Phi = \pm\pi$. However, in **B** the phase difference oscillates in a narrow range of $\Phi \approx 0$ due to the asymmetry of the waveforms, as can be seen in Figure 6.17 (a). In both **A** and **B** no phase-slips are observed and phase synchronisation holds. This is in agreement with there being only a single Lyapunov exponent at zero, indicative of the network acting as a single system. The dynamics of the subsystems suffer phase-slips at the merger of **A** and **B**, separating their dynamics, before they again become progressively more unified at higher parameter values. These intermittencies found on the transition between different synchronisation regimes can be seen in (b). At such parameter values it was difficult to experimentally measure a Lyapunov exponent at zero, so it is believed that the intermittent loss of phase synchronisation in these regimes results in the dynamics of the subsystems temporarily separating from each other. However, as β is further increased trajectories are found to

spend less time in **B** and the system again approaches phase synchronisation, as can be seen in (i) of Figure 6.17 (c).

Only a single zero Lyapunov exponent was detected numerically as well as experimentally at these higher parameter values, indicating that the system can again be treated as a single entity. This occurs as phase synchronisation is re-established in the system and trajectories spend progressively more time in **A**. This demonstrates that, although each of **A** and **B** develop hyperchaos independently, the final attractor **M** is mainly composed of the hyperchaotic remnant of **A**, with a small contribution from **B**.

6.6 Summary

In this chapter the origin of hyperchaos in the system has been investigated. The transition from low dimensional to high dimensional dynamics in the system has been studied along with the synchronisation states responsible. To this end a detailed investigation has been carried out to determine the origin and characteristics of the attractors which exist when the dynamics are low dimensional. The transition to hyperchaos has been shown to be most likely due to the bifurcation of UPOs in the chaotic attractors of the system. The analysis has also covered how these sets become nonattracting before they combine and interact at higher values of the parameter β. In these regimes the system is purely hyperchaotic, before the appearance of the disconnected **D** branch and the onset of strong UDV measured in Chapter 5.

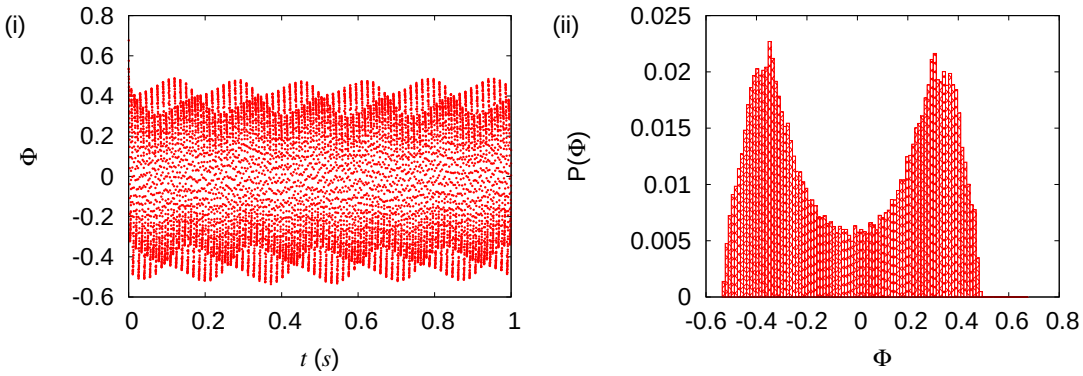

(a) $\beta = 3.356$

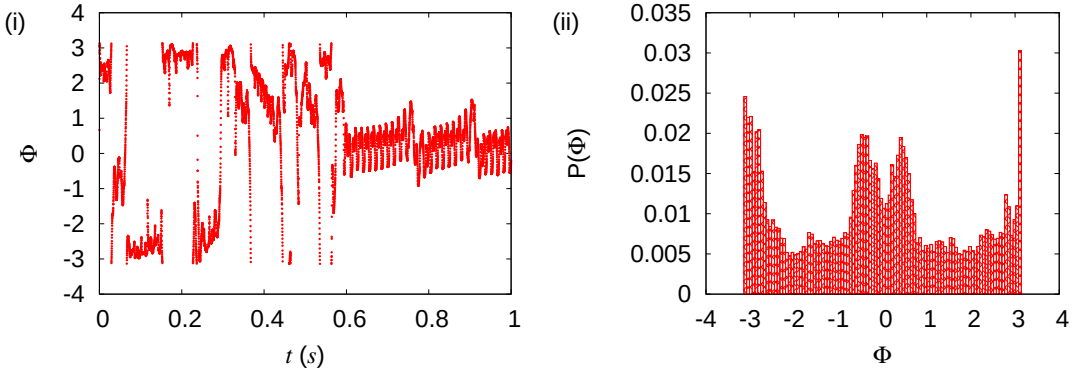

(b) $\beta = 3.332$

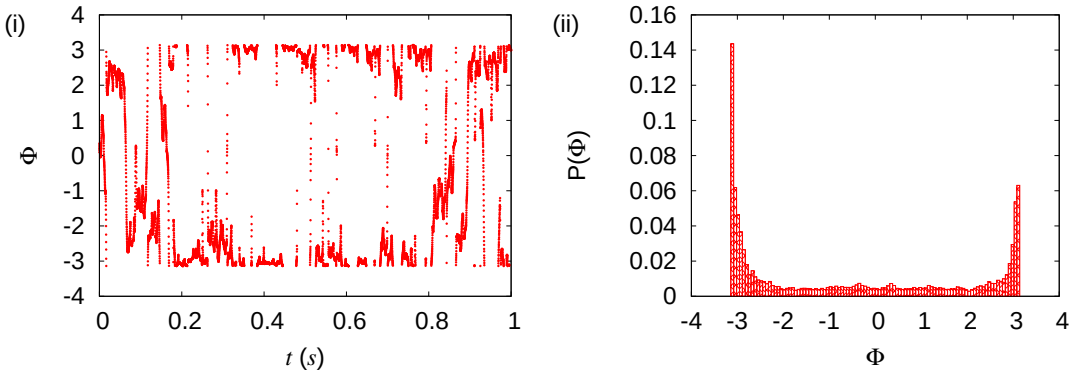

(c) $\beta = 3.602$

Figure 6.17: Phase differences Φ, used for detecting phase synchronisation states. At values of β such as shown in (a), where states are in "**B**", Φ oscillates close to zero. At values similar to those used for (b) intermittencies are found between "**B**" and "**A**", where $\Phi \approx \pm\pi$. At higher β phases are mainly restricted to $\pm\pi$ and trajectories spend most of their time in "**A**", as shown in (c).

Chapter 7

Conclusions

Much of the world around us exhibits complex behaviour in some form or another and understanding this complexity is one of the key challenges for contemporary science. It is becoming increasingly apparent that a large proportion of the dynamics we observe stems from the coupling between individually low-dimensional elements. This creates combined systems with large numbers of degrees of freedom, which can exhibit high dimensional dynamics. Conversely, through synchronisation, the dimensionality of a system can be reduced and in such cases there is hope of at least partially understanding the mechanisms responsible for some of the observed behaviour.

Theories in nonlinear dynamics help us to understand low-dimensional chaotic systems, despite the limitations imposed by sensitive dependence on initial conditions. Dynamical systems theory has therefore provided a framework for the understanding of chaos and other nonlinear phenomena. Understanding of the internal structure of chaotic attractors is important in low-dimensional systems, with theories about the unstable periodic orbits, which form the backbone of chaotic attractors, providing insight into the dynamics on such attractors. Therefore it is also important to extend these ideas to hyperchaotic attractors, so that we can develop our understanding of the dynamics in these cases.

In higher dimensional systems, attractors can be composed of invariant sets,

each with different internal dynamics. Theories have shown how these can combine to form a globally stable manifold upon which hyperchaotic attractors can exist. It is therefore useful to be able to identify such sets and understand how they contribute to the overall behaviour.

For this thesis, hyperchaos has been studied in a demonstration experimental system, in order to provide evidence for the mechanisms responsible for complex behaviour in coupled networks. Modified van der Pol electronic oscillators were used for these investigations, proving ideal due to the large amounts of data that can be obtained from them. Van der Pol type oscillators are used as models throughout biology, for example to represent neurons in the brain. This type of electronic oscillator is also very useful as the parameters can be carefully controlled and the level of noise kept to a minimum. Various coupling configurations have been used on these units (or *cells*) to study simple networks including three-cell systems close to Hopf bifurcations. As a demonstration of their practical utility, a novel system for sensitive signal detection was constructed and investigated.

For the main body of this thesis, a detailed experimental and numerical study has been carried out on a system of oscillators coupled unidirectionally in a ring, investigating the transition to high dimensional dynamics therein. The origin of hyperchaos in the constituent sets of the system was investigated using time-series analysis techniques. Throughout this work, new data analysis methods have been developed, tested and used on measurements from the experiment. To compliment these experimental approaches, computational algorithms have also been employed to solve the equations of motion of the system and extract numerical estimates of measures such as the Lyapunov exponents, in order to verify and complete the results.

Embedding techniques have been used as a basis for many techniques to analyse the degree of complexity of the systems under investigation. A newly developed method for determining the local attractor dimension was introduced

which is very easy to implement, as well as being robust enough to yield useful information solely from experimental time-series data. This was used for detecting unstable dimension variability (UDV); a feature believed to be common in high-dimensional systems. The effect of UDV is detrimental to numerical models of systems suffering from it, reducing the time for which such models can be relied. The method used here provides an alternative to techniques that are usually employed in numerical investigations. Instead of measuring the short-time Lyapunov exponents directly, this new technique determines the degree of expansion of trajectories along different directions by measuring the spread of local sets of embedded points throughout the attractor. The method was also used to identify invariant sets and extract them from the overall attractor. This allowed the evaluation of shadowing times, which is a measure of the length of time for which numerical results can be relied. These were shown to have different scaling for short and long times, in agreement with theoretical predictions. The separated invariant sets were additionally used to make measurements of the local Lyapunov exponents, which is not usually possible from experimental data. The method also proved useful in later investigations into the origins of hyperchaos in the system.

The results of an investigation into the development of high dimensional dynamics in the system have been described. A study of the phenomena found in the system of coupled oscillators was presented. Techniques have been used to identify synchronisation between oscillations of the individual cells. The transitions between the different types of synchronisation were described, along with the resulting transition to hyperchaos. Hyperchaos was found to appear in the above system after the combination of two distinct sets, related by a phase difference in the oscillations of the individual cells; an example of phase-multistability. Numerical studies revealed that each of these sets independently develops a second positive Lyapunov exponent as they lose stability to become nonattracting sets. The transition to two positive Lyapunov exponents and hyperchaos was

found both experimentally and numerically to be smooth in both of the phase multistable synchronisation states. To uncover the origin of this transition experimentally, generalised synchronisation was investigated over a range of parameter values. Additionally, the transition was studied in terms of the topological dimension, using the method developed for detecting UDV. The progressive loss of generalised synchronisation, along with the smooth transition in the Lyapunov exponents and steady change in the measured local dimension all indicate that attractor bubbling due to a riddling bifurcation was responsible for the appearance of a second expanding direction to the flow. This provides a mechanism for a steady transition to two positive Lyapunov exponents via the unstable periodic orbits which form the stable manifold of the attractor becoming sequentially unstable along the transverse direction. The emergence of stable hyperchaos was physically observable in the system after the combination of the two phase-states in a single mixed attractor.

In summary, nonlinear electronic circuits have been used to demonstrate the emergence of hyperchaos as well as important behaviour such as UDV found in such regimes. Numerical and time-series analysis techniques have been used extensively to investigate and explain these phenomena at the transition to high dimensional dynamics in systems of coupled oscillators.

Bibliography

[ABST93] H. D. I. Abarbanel, R. Brown, J. J. Sidorowich, and L. Sh. Tsimring. The analysis of observed chaotic data in physical systems. *Rev. Mod. Phys.*, 65(4):1331–1391, 1993.

[Ans67] A. D Ansov. *Proc. Steklov Inst. Math.*, 90:1, 1967.

[Bal99] Philip Ball. *The Self-Made Tapestry (pattern formation in nature).* Oxford, 1999.

[Ben69] R. S. Bennett. The intrinsic dimensionality of signal collections. *IEEE Trans. Inf. Theo.*, IT-15(5):517–525, 1969.

[BGGS80] G. Benettin, L. Galgani, A. Giorgilli, and J-M. Strelcyn. Lyapunov characteristic exponents for smooth dynamical systems and for Hamiltonian systems; a method for computing all of them. Part 2: Numerical application. *Meccanica*, 15:9–20, 1980.

[BJK87] D. S. Broomhead, R. Jones, and G. P. King. Topological dimension and local coordinates from time series data. *J. Phys. A: Math. Gen.*, 20:L563–L569, 1987.

[BJM+03] E. Barreto, K. Josić, C. J. Morales, E. Sander, and P. So. The geometry of chaos synchronization. *Chaos*, 13 (1):151–164, 2003.

[BK86] D. S. Broomhead and G. P. King. Extracting qualitative dynamics from experimental data. *Physica D*, 20:217–236, 1986.

[BKO+02] S. Boccaletti, J. Kurths, G. Osipov, D. L. Valladares, and C. S. Zhou. The synchronization of chaotic systems. *Physics Reports*, 366:1–101, 2002.

[Ble88] I. I. Blekhman. *Synchronization in Science and Technology*. New York: ASME, 1988.

[Bow75] R. Bowen. co-limit sets for Axiom A diffeomorphisms. *J. Diff. Eqations*, 18:333–339, 1975.

[BS00] E. Barreto and P. So. Mechanisms for the Development of Unstable Dimension Variability and the Breakdown of Shadowing in Coupled Chaotic Systems. *Phys. Rev. Lett.*, 85 (12):2490–2493, 2000.

[BSRW02] M. Bennet, MF Schatz, H. Rockwood, and K. Wiesenfeld. Huygens's clocks. *Proceedings of the Royal Society of London A*, 458:563–579, 2002.

[CP91] S. N. Chow and K. J. Palmer. On the numerical computation of orbits of dynamical systems: The one-dimensional case. *J. Dyn. Diff. Equ.*, 3 (3):361–379, 1991.

[CVV94] S.-N. Chow and E. S. Van Vleck. A shadowing lemma approach to

global error analysis for initial value ODEs. *SIAM J. SCI. COMPUT*, 15(4):959–976, 1994.

[Daw96] Silvina Ponce Dawson. Strange nonattracting chaotic sets, crises, and fluctuating lyapunov exponents. *Phys. Rev. Lett.*, 76 (23):4348–4351, 1996.

[DGSY94] S. Dawson, C. Grebogi, T. Sauer, and J. A. Yorke. Obstructions to shadowing when a Lyapunov exponent fluctuates about zero. *Phys. Rev. Lett.*, 73 (14):1927–1930, 1994.

[DL04] Y. Do and Y.-C. Lai. Statistics of shadowing time in nonhyperbolic chaotic systems with unstable dimension variability. *Phys. Rev. E*, 69:16213–1, 2004.

[Doe81] E. Doedel. AUTO, a program for the automatic bifurcation analysis of autonomous systems. *Cong. Numer.*, 30:265, 1981.

[EOC+00] V. Eguíluz, M. Ospeck, Y. Choe, A. Hudspeth, and M. Magnasco. Essential nonlinearities in hearing. *Phys. Rev. Lett.*, 84(22):5232–5235, 2000.

[ER92] JP Eckman and D. Ruelle. Fundamental limitations for estimating dimensions and Lyapunov exponents in dynamical systems. *Physica D*, 56:185–187, 1992.

[FCF+81] H. Froehling, J. P. Crutchfield, D. Farmer, N. H. Packard, and R. Shaw. On determining the dimension of chaotic flows. *Physica D*, 3:605, 1981.

[Fit61] R. Fitzhugh. Impulses and physiological states in models of nerve membrane. *Biophysical Journal*, 1:445–466, 1961.

[GAM01] P. Glendinning, J. Abshagen, and T. Mullin. Imperfect homoclinic bifurcations. *Phys. Rev. E*, 64:208–1–208–8, 2001.

[GH83] J. Guckenheimer and P. Holmes. *Nonlinear oscillations, dynamical systems and bifurcations of vector fields.* Springer-Verlag, 1983.

[GHYS90] C. Grebogi, S. M. Hammel, J. A. Yorke, and T. Sauer. Shadowing of physical trajectories in chaotic dynamics: Containment and refinement. *Phys. Rev. Lett.*, 65:1527–1530, 1990.

[GKOY87] C. Grebogi, E. Kostelich, E. Ott, and J. A. Yorke. Multi-dimensioned intertwined basin boundaries: basin structure of the kicked double rotor. *Physica D*, 25:347–360, 1987.

[GNS04] M. Golubitsky, M. Nicol, and I. Stewart. Some curious phenomena in coupled cell networks. *J. Nonlin. Sci.*, 14(2):207–236, 2004.

[Gol06] M. Golubitsky. Symmetry and neuroscience. *Current Events, Amer. Math. Soc.*, 2006.

[GOY83] C. Grebogi, E. Ott, and J. A. Yorke. Crises, sudden changes in chaotic attractors, and transient chaos. *Physica D*, 7:181–200, 1983.

[GP48] T. Gold and RJ Pumphrey. Hearing. I. The Cochlea as a Frequency Analyzer. *Proceedings of the Royal Society of London. Series B, Biological Sciences*, 135(881):462–491, 1948.

[GR03] M. C. Göpfert and D. Robert. Motion generation by Drosophila mechanosensory neurons. *Proc. Nat. Acad. Sci.*, 100(9):5514–5519, 2003.

[GSBJ98] M. Golubitsky, I. Stewart, P.-L. Buono, and J. J.Collins. A modular network for legged locomotion. *Physica D*, 115:56–72, 1998.

[Ham50] J. M. Hammersley. The distribution of distances in a hypersphere. *Ann. Math. Stat.*, 21(3):447–452, 1950.

[HBC+91] J. J. Healey, D. S. Broomhead, K. A. Cliffe, R. Jones, and T Mullin. The origins of chaos in a modified Van der Pol oscillator. *Physica D*, 48:332–339, 1991.

[He03] D. He. Spatio-temporal synchronization of recurrent epidemics. *Proceedings: Biological Sciences*, 270(1523):1519–1526, 2003.

[Hea91] J. J. Healey. *Qualitative Analysis of Experimental Time Series*. PhD thesis, Oxford University, 1991.

[HER05] J.M. Harte, S.J. Elliott, and H.J. Rice. A comparison of various non-linear models of cochlear compression. *The Journal of the Acoustical Society of America*, 117:3777, 2005.

[HKB85] H. Haken, J. A. S. Kelso, and H. Bunz. A theoretical model of phase transitions in human hand movements. *Biological Cybernetics*, 51 (5):347–356, 1985.

[HP68] M.W. Hirsch and C.C. Pugh. Stable manifolds and hyperbolic sets. *Global Analysis (Proc. Sympos. Pure Math.)*, XIV:133–163, 1968.

[HPF90] T. Hediger, A. Passamante, and M. E. Farrell. Characterizing attractors using local intrinsic dimensions calculated by singular-value decomposition and information-theoretic criteria. *Phys. Rev. A*, 41:5325–5332, 1990.

[Huy01] C. Huygens. (a) letter to his father. (b) Sea clocks (sympathy of clocks). Part V. *Pikovsky, A. and Rosenblum, M. and Kurths, J., Synchronization (A universal concept in nonlinear sciences): Appendix A*, 2001.

[HYG87] S. M. Hammel, J. A. Yorke, and C. Grebogi. Do numerical orbits of chaotic dynamical processes represent true orbits? *J. Complex.*, 3:136–145, 1987.

[HYG88] S. M. Hammel, J. A. Yorke, and C. Grebogi. Numerical orbits of chaotic processes represent true orbits. *Bull. Am. Math. Soc.*, 19 (2):465–469, 1988.

[JÖ1] F. Jülicher. Mechanical oscillations at the cellular scale. *C. R. Acad. Sci. Paris Sér. IV*, pages 849–860, 2001.

[JDM97] A. Juel, A. G. Darbyshire, and T. Mullin. The effect of noise on pitchfork and Hopf bifurcations. *Proc. R. Soc. Lond. A*, 453:2627–2647, 1997.

[KBA92] M. B. Kennel, R. Brown, and H. D. I. Abarbanel. Determining embedding dimension for phase-space reconstruction using a geometrical construction. *Phys. Rev. A*, 45:3403–3411, 1992.

[KD99] Paul Kerr-Delworth. *Static and Dynamic Bifurcations in Coupled Oscillators*. PhD thesis, University of Manchester, 1999.

[Kin82] Lawrence E. Kinsler. *Fundamentals of acoustics*, chapter 11. Wiley, 3 edition, 1982.

[KKG+97] E. J. Kostelich, I. Kan, C. Grebogi, E. Ott., and J. A. Yorke. Unstable dimension variability: a source of nonhyperbolicity in chaotic systems. *Physica D*, 109:81–90, 1997.

[KMP00] T. Kapitaniak, Y. Maistrenko, and S. Popovych. Chaos-hyperchaos transition. *Phys. Rev. E*, 62(2):1972–1976, 2000.

[KS03] A. Kern and R. Stoop. Essential Role of Couplings between Hearing Nonlinearities. *Physical Review Letters*, 91(12):128101, 2003.

[Kur84] Y. Kuramoto. *Chemical Oscillations, Waves, and Turbulence*. Springer, Berlin, 1984.

[Kuz05] S. P. Kuznetsov. Example of a physical system with a hyperbolic attractor of the smale-williams type. *Phys. Rev. Lett.*, 95:144101, 2005.

[LG99] Y.-C. Lai and C. Grebogi. Modeling of Coupled Chaotic Oscillators. *Phys. Rev. Lett.*, 82 (24):4803–4806, 1999.

[LGYK93] Y.-C. Lai, C. Grebogi, J. A. Yorke, and I. Kan. How often are chaotic saddles nonhyperbolic? *Nonlinearity*, 6:779–797, 1993.

[LLWG99] Y.-C. Lai, D. Lerner, K. Williams, and C. Grebogi. Unstable dimension variability in coupled chaotic systems. *Phys. Rev. E*, 60:5445–5454, 1999.

[Lor63] E. N. Lorenz. Deterministic nonperiodic flow. *J. Atmos. Sci.*, 20:130–141, 1963.

[MD97] P. Moresco and S. P. Dawson. Chaos and crises in more than two dimensions. *Phys. Rev. E*, 55:5350–5360, 1997.

[MD99] P. Moresco and S. P. Dawson. The PIM-simplex method: an extension of the PIM-triple method to saddles with an arbitrary number of expanding directions. *Physica D*, 126:38–48, 1999.

[MH99] Pascal Martin and A. J. Hudspeth. Active hair-bundle movements can amplify a hair cell's response to oscillatory mechanical stimuli. *PNAS*, 96(25):14306–14311, 1999.

[MM06] N. J. McCullen and P. Moresco. Method for measuring unstable dimension variability from time series. *Phys. Rev. E.*, 73:46203, 2006.

[Mul93] Tom Mullin, editor. *The Nature of Chaos*. Oxford, 1993.

[OEM01] M. Ospeck, VM Eguiluz, and MO Magnasco. Evidence of a Hopf Bifurcation in Frog Hair Cells. *Biophysical Journal*, 80(6):2597–2607, 2001.

[OHZ+03] G.V. Osipov, B. Hu, C. Zhou, M.V. Ivanchenko, and J. Kurths. Three Types of Transitions to Phase Synchronization in Coupled Chaotic Oscillators. *Physical Review Letters*, 91(2):24101, 2003.

[PC90] L. M. Pecora and T. L. Caroll. Synchronisation in chaotic systems. *Phys. Rev. Lett.*, 64:821–824, 1990.

[PG92] H. Poincare and D. Goroff. *New Methods of Celestial Mechanics*. New Methods of Celestial Mechanics, 1200 pp. (3 volume set not available separatly).. AIP Press. Also History of Modern Physics and Astronomy, volume 13, 1992.

[PRK99] A. Pikovsky, M. Rosenblum, and J. Kurths. Phase synchronisation in regular and chaotic systems. *Int. Journ. Bifurcation and Chaos*, 10(10):2291–2305, 1999.

[PRK01] A. Pikovsky, M. Rosenblum, and J. Kurths. *Synchronization (A universal concept in nonlinear sciences)*. Cambridge, 2001.

[PRZ+99] AS Pikovsky, MG Rosenblum, MA Zaks, J. Kurths, and HG Schuster. Phase synchronization of regular and chaotic oscillators. *Handbook of Chaos Control*, pages 305–328, 1999.

[PTVF92] William H. Press, Saul A. Teukolsky, William T. Vetterling, and Brian P. Flannery. *Numerical Recipes in C (The Art of Scientific Computing)*, chapter 16. Cambridge, second edition, 1992.

[PVS+99] D. E. Postnov, T. E. Vadivasova, O. V. Sosnovtseva, A. G. Balanov, V. S. Anishchenko, and E. Mosekilde. Role of multistability in the transition to chaotic phase synchronization. *Chaos*, 9(1):227–232, 1999.

[R$\ddot{\text{o}}$79] O. E. Rössler. An equation for hyperchaos. *Phys. Lett. A*, 71(2,3):155–157, 1979.

[RPK96] M. G. Rosenblum, A. S. Pikovsky, and J. Kurths. Phase synchronization of chaotic oscillators. *Phys. Rev. Lett.*, 76 (11):1804–1807, 1996.

[RPK+01] MG Rosenblum, A. Pikovsky, J. Kurths, C. Schäfer, and P.A. Tass. Phase synchronization: from theory to data analysis. *Handbook of Biological Physics*, 4:279–321, 2001.

[RST95] N. F. Rulkov, M. M. Sushchik, and L. S. Tsimring. Generalized synchronization of chaos in directionally coupled chaotic systems. *Phys. Rev. E*, 51 (2):980–994, 1995.

[Sau02] T. Sauer. Shadowing breakdown and large errors in dynamical simulations of physical systems. *Phys. Rev. E*, 65:36220, 2002.

[SBK+02] P. So, P. Barreto, J. Krešimir, S. Elvyn, and S. J. Schiff. Limits to the experimental detection of nonlinear synchrony. *Phys. Rev. E*, 65:46225, 2002.

[SGY97] T. Sauer, C. Grebogi, and J. A. Yorke. How long do numerical chaotic solutions remain valid. *Phys. Rev. Lett.*, 79:59–62, 1997.

[SKG+06] R. Stoop, A. Kern, M.C. Göpfert, D.A. Smirnov, T.V. Dikanev, and B.P. Bezrucko. A generalization of the van-der-Pol oscillator underlies active signal amplification in Drosophila hearing. *European Biophysics Journal*, 35(6):511–516, 2006.

[SVK04] R. Stoop, J.-J. V.D. Vyver, and A. Kern. Limit cycles, noise, and chaos in hearing. *Microscopy Res. and Tech.*, 63:400–412, 2004.

[SW84] J. W. Swift and K. Wiesenfeld. Suppression of period doubling in symmetric systems. *Phys. Rev. Lett.*, 52 (9):705–708, 1984.

[SY91] T. Sauer and J. A. Yorke. Rigorous verification of trajectories for the computer simulation of dynamical systems. *Nonlinearity*, 4 (3):961–979, 1991.

[SYM81] M. Shinriki, M. Yamamoto, and S. Mori. Multimode oscillations in a modified Van der Pol oscillator containing a positive nonlinear conductance. *Proc. I.E.E.E.*, 69:394, 1981.

[Tak81] F. Takens. *"Detecting Strange Attractors in Turbulence", Lecture Notes in Math. Vol. 898,*. Springer, New York, 1981.

[TNS05] M. Todoriki, H. Nagayoshi, and A. Suzuki. Temporal fluctuation of singular values caused by dynamical noise in chaos. *Phys. Rev. E*, 72:36207, 2005.

[Tur52] A. M. Turing. The Chemical Basis of Morphogenesis. *Royal Society of London Philosophical Transactions Series B*, 237:37–72, August 1952.

[vdP27] B. van der Pol. Forced oscillations in a circuit with nonlinear resistance (receptance with reactive triode). *London, Edinburgh and Dublin Phil. Mag.*, 3:65–80, 1927.

[Wat94] John Watkinson. *The Art of Digital Audio*, chapter 3. Focal Press, 2 edition, 1994.

[Wig90] S. Wiggins. *Introduction to Apllied Nonlinear Dynamical Systems and Chaos*. Springer-Verlag, 1990.

[WSSV85] A. Wolf, J. B. Swift, H. L. Swinney, and J. A. Vastano. Determining Lyapunov exponents from a time series. *Physica D*, 16:285–317, 1985.